DEVELOPMENT OF HIGH PERFORMANCE WATER BASE MUD AND

ESTIMATION OF DOWNHOLE SWELLING

A Dissertation

by

TAKUMA KANESHIMA

Submitted to the Office of Graduate and Professional Studies of
Texas A&M University
in partial fulfillment of the requirements for the degree of

DOCTOR OF PHILOSOPHY

Chair of Committee,	Nobuo Morita
Committee Members,	Jerome J. Schubert
	Samuel F. Noynaert
	Hiroko Kitajima
Head of Department,	Jeff Spath

August 2019

Major Subject: Petroleum Engineering

ABSTRACT

Shale swelling causes 90% of wellbore instabilities and oil-base muds (OBM) have been the best choice for many years. However, the stringent environmental concern have resulted in a keen interest in the development of highly inhibitive, high-performance water-base mud (HPWBM). Recently, polyamines have been widely studied as high performance shale inhibitors and applied around the world. However, the results indicated that the polyamines were incompatible with bentonite.

In this study, we clarified the incompatibility issue. Then, we checked the performance of lignosulfonate commonly used in the industry as a deflocculant and found it to be insufficient. For further improvements, we introduced polyvinyl alcohol (PVOH) as a new polymeric deflocculant and found that PVOH worked better than lignosulfonate.

Shale swelling has been commonly measured using linear swell meter (LSM). Since preserved shale core is rarely available, swelling tests are usually performed on "pellets" created from cuttings. Even though capillary pressure effect can be avoided by ensuring full saturation of the pellets, they would swell more than the intact shales. Besides, the LSM measurements are performed under atmospheric pressure and temperature, whereas downhole swelling obviously occurs under in situ conditions. For these two reasons, they do not represent the actual downhole swelling and thereby we are not able to predict wellbore stability. Some studies have been done on the

measurement of swelling under high pressure, however, they all require specially

designed equipment.

In this study, we measured swelling of both pellet and intact core samples under

various stress conditions using the conventional LSM in order to estimate the downhole

swelling by extrapolation. And we analytically checked the consistency of the swelling

measured under atmospheric pressure and the one estimated by extrapolation with field

observations.

As a result, we found that prediction of the wellbore stability could significantly

be improved by taking the effect of stress into account. Then, we proposed an improved

method that could analytically predict the wellbore stability from the estimated

downhole swelling even when the preserved intact core was not available.

DEDICATION

This work is dedicated first and foremost to my wife, Shiki. Without your continuous love, support and sacrifices, my work would never have been completed.

I also dedicate this work to my son, Taro. I have never seen anything but smiles and encouragement from you even though the past few years may have been difficult for you at times.

To all the friends and family who were part of this along the way, I thank you as well. It gives me great joy to finally be able to answer your "how is the PhD going?" with "It's done!".

ACKNOWLEDGEMENTS

CONTRIBUTORS AND FUNDING SOURCES

Contributors

This work was supervised by a dissertation committee consisting of Dr. Nobuo Morita [advisor], Dr. Jerome J. Schubert [committee member], Dr. Samuel F. Noynaert [committee member] of the Department of Petroleum Engineering, and Dr. Hiroko Kitajima [committee member] of the Department of Geology & Geophysics.

The data analyzed for 1.3.6.3 was provided by Kuraray co., ltd.. All other work conducted for the dissertation was completed by the student independently.

Funding Sources

NOMENCLATURE

μ_p	Plastic viscosity
τ_y	Yield point
θ_{600}	Dial reading with the viscometer operating at 600 rpm
θ_{300}	Dial reading with the viscometer operating at 300 rpm
V_f	Volume of filtrate
k	Permeability of the mudcake
Δp	Pressure drop across the mudcake
f_{sc}	Volume fraction of solids in the cake
f_{sm}	Volume fraction of solids in the mud
A	Area of the filter paper
t	Time
μ_f	Viscosity of the mud filtrate
W_a	Amount of water to be added to the ground rock
P	Consolidation pressure
σ_{H1}	Horizontal stress
σ_{H2}	Horizontal stress
σ_v	Vertical stress
P_p	Pore pressure
σ_H	Maximum horizontal stress

σ_h	Minimum horizontal stress
P_w	Wellbore pressure
σ_r	Radial stress
σ_θ	Tangential stress
σ_z	Axial stress
E	Young's modulus
ν	Poisson's ratio
r_w	Wellbore radius
α	Biot constant
η	Thermal expansion coefficient
Δp_w	Drawdown at the wellbore surface
ΔT_w	Temperature change at the wellbore surface
ΔS_w	Swelling at the wellbore surface
τ_0	Cohesion
μ	Internal friction coefficient; $\mu = \tan\phi$
ϕ	Internal friction angle
θ_{swell}	Volumetric swelling
$\varepsilon_{\text{swell}}$	Swelling strain
P_c	Confining pressure

TABLE OF CONTENTS

LIST OF FIGURES

xi

xiii

LIST OF TABLES

1. DEVELOPMENT OF HIGH PERFORMANCE WATER BASE MUD

1.1. Introduction

1.1.1. Literature Review

Shale makes up 75% of drilled formations and causes 90% of wellbore

instabilities (Tare and Mody 2002). Problems caused by water adsorption on the clay

such as borehole enlargement, disintegration of cuttings, and wellbore instability are

troublesome for drilling engineers. Oil-base muds (OBM) have been the choice of

challenging shale sections for many years (Dye et al. 2006). These mud systems can

bring advantages, including optimal shale stability, low torque and drag, good resistance

to contamination, and high drilling rates. However, the increasingly stringent

environmental concern and legislation limit their wide application. These increasing

environmental demands have resulted in a keen interest in the development of highly

inhibitive, high-performance water-base mud (HPWBM) system, which would have

similar drilling advantages to OBMs. The history of water-base mud in terms of shale

swelling inhibition is shown in Table 1 (Darley, H. C. H. 1988). Since the first well was

drilled in Texas in 1890, starting from using barite as a weighting agent, a lot of

technologies have been tested and KCl was proved to be highly effective in stabilizing

shales in 1972. As is well known, however, the potassium ion is highly flocculating and

its presence in the mud can adversely affect rheological and filtration control, thereby,

significantly influencing mud cost. Moreover, the disposal of KCl in large quantities can

be a problem affecting marine ecology and land farming (Chesser 1987, Patel and

1

Friedheim 2007). In any case, the KCl salt became the main shale inhibition agent and has been used in combination with various other salts and fluids.

Table 1 History of water-base mud

Year	Technology	Year	Technology
1890	The first well drilled in Texas	1970	Polymer
1922	Barite used as weighting agent	1972	KCl
1935	Brine	1980	KCl/PHPA
1940	Silicate	1990	Silicate/Glycol
1945	Tannin	2000	Polyamine
1955	Gypsum		

For more than the past decade, polyamines have been widely studied as high performance shale inhibitors and applied extensively around the world with success (Huadi et al. 2010, Mehtar et al. 2010, Young and Ramses 2006). Recently, oligomeric polyetheramines have been proven to be more effective and applied to Bohai Bay shale formations (Patel et al. 2001, Zhong et al. 2011, Zhong et al. 2013, Zhong et al. 2015, Patel et al. 2009). Figure 1 shows the schematic drawing describing working mechanism of the oligomeric polyetheramine shale inhibitor. Oligomeric polyetheramine, such as the one shown in the figure, perfectly fits between clay platelets tending to collapse the clay's hydrated structure and greatly reduce the clay's tendency to imbibe water from the aqueous environment.
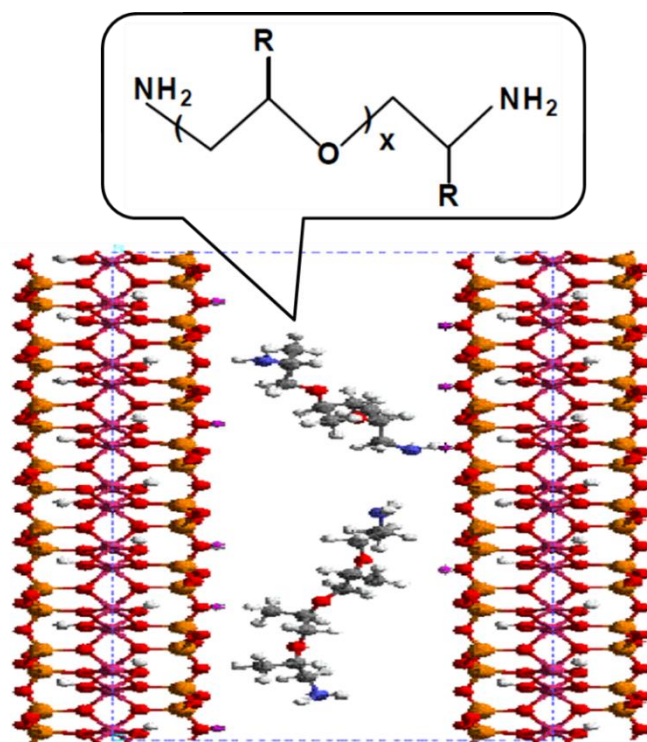
Figure 1 Molecular model of oligomeric shale inhibitor binding two shale layers (Adapted from Patel et al. 2009)

These researchers used the bentonite inhibition test to determine the ability of the oligomeric polyetheramine to prevent bentonite from swelling and maintain a low rheological profile (Figure 2, Left). The test determines the maximum amount of API bentonite that can be inhibited by a single treatment of shale inhibitor. Then they performed the bentonite swelling test (Figure 2, Right). They compacted sodium bentonite powder into pellets and immersed the pellets in the various drilling mud filtrates and measured the swelling. Because the swelling of the high performance water-base drilling fluid (HPWDF) shown in pink curve is smaller than the other water base muds, they applied it to the actual formation.
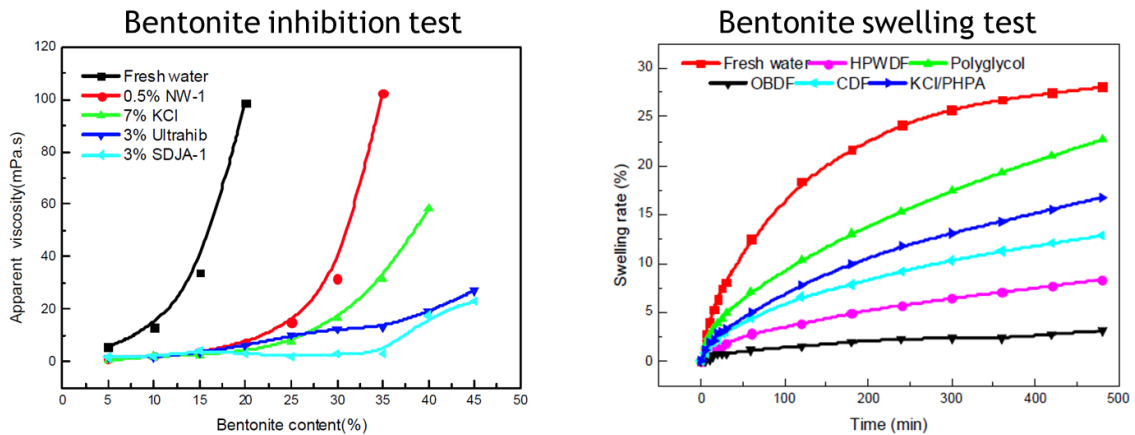
Figure 2 Left) Variation of apparent viscosity with bentonite content in various inhibitor solutions; Right) Linear swelling rate of clay pellet in different drilling fluid filtrate (Reprinted from Zhong et al. 2013)

From another perspective, however, the oligomeric polyetheramine that has been proved to be effective by those tests is suspected to be incompatible with bentonite when formulating water-base muds where bentonite is supposed to swell, disperse, and increase the viscosity.

Lignosulfonate has been commonly used as a deflocculant for KCl muds (Netwas Group). To further improve the mud properties, we introduce polyvinyl alcohol (PVOH) as a new polymeric deflocculant. The effects that PVOH exerts on clay dispersions have been extensively studied (Chang et al. 1992, Heath and Tadros 1983, Dairanieh and Lahalih 1988, Mostafa and Assaad 2007, İşçi et al. 2006). In the presence of shale inhibitors such as KCl and polyamines, however, no research has been done on the interaction between PVOH and clay or the effect that PVOH exerts on clay dispersions.

1.1.2. Objective

In this study, we clarify a compatibility issue between the oligomeric polyetheramine and bentonite in terms of rheology and fluid loss control. We check the performance of lignosulfonate as a deflocculant for KCl muds and oligomeric polyetheramine muds. To further improve mud properties, we introduce polyvinyl alcohol (PVOH) as a new polymeric deflocculant and investigate its performance and working mechanism. Furthermore, we check the compatibility of PVOH with other additives commonly used in the industry and high temperature tolerance. Lastly, we optimize the mud composition to achieve low shale swelling.

1.2. Experimental Methods

1.2.1. Materials

Wyoming bentonite, carboxymethyl cellulose, starch, lignosulfonate, and lignite were supplied by Newpark Resources Inc. by the names of NewGel, NewPacR, NDFT303, NewFlow, and NewLig, respectively. Polyvinyl alcohol was supplied by Kuraray co., ltd. by the name of Kuraray Poval. Potassium chloride and hydrochloric acid were purchased from The Lab Depot, Inc.. Poly(propylene glycol) bis(2-aminopropyl ether) ($\overline{M_n} \sim 230$), potassium hydroxide, and deionized water were purchased from MilliporeSigma Corporate. All experimental materials were used without further purification.

1.2.2. Outcrop Shale Sample

The Marcellus shale outcrop sample was provided by Dr. A Daniel Hill of Harold Vance Department of Petroleum Engineering. Table 2 is the list of outcrop shale sample.

Table 2 List of outcrop shale sample

Sample	Collection location	Bulk density (g/cc)
Marcellus	Pennsylvania	2.3800

1.2.3. Mud Preparation

Bentonite dispersion was prepared by adding bentonite powder to deionized water with rapid stirring using a Hamilton Beach HMD200 mixer such that the concentration of the resulting dispersion was 8 wt%. The dispersion was kept under ambient condition for at least 2 days to ensure pre-hydration. Polyvinyl alcohol aqueous solutions were prepared by adding PVOH powder to deionized water with rapid stirring and heating up to 200 $^{\circ}$F using a magnetic stirrer equipped with hotplate. Mud samples were prepared by adding other additives to the pre-hydrated bentonite dispersion with rapid stirring using a magnetic stirrer. pH of the muds were adjusted by adding potassium hydroxide or hydrochloric acid.

1.2.4. Rheology

Rheological characteristics of the muds were measured with a Fann Model 35 Viscometer at 3, 6, 100, 200, 300, and 600 rpm at room temperature. Results were characterized by the Bingham plastic model in terms of plastic viscosity, μ_p, and yield point, τ_y as shown in Figure 3. μ_p and τ_y were computed using

$$\mu_p = \theta_{600} - \theta_{300} \text{ (cp)}$$

$$\tau_y = \theta_{300} - \mu_p \text{ (lbf/100 ft}^2\text{)},$$

where θ_{600} is the dial reading with the viscometer operating at 600 rpm and θ_{300} is the dial reading with the viscometer operating at 300 rpm.
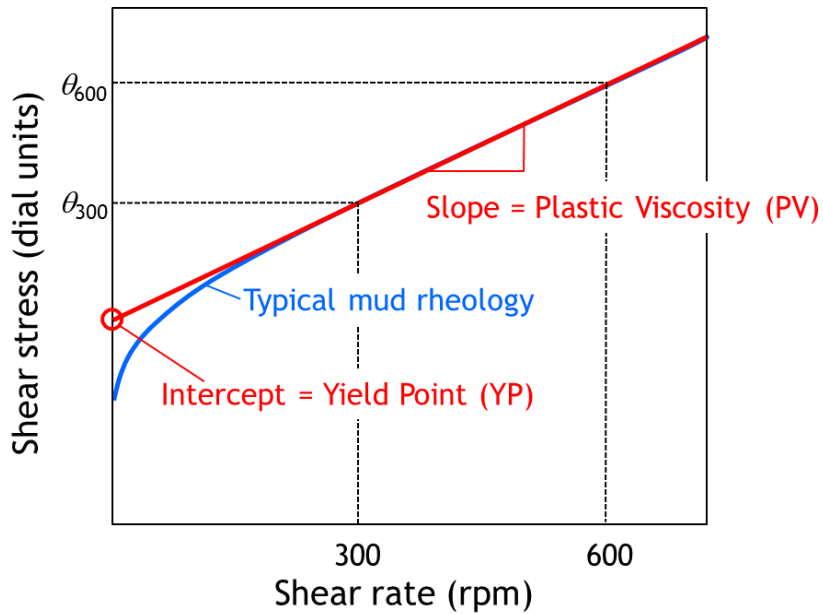
Figure 3 Variation of shear stress with shear rate and definition of plastic viscosity (PV) and yield point (YP) based on Bingham plastic model

7

1.2.5. Fluid Loss

A Fann Multiple Unit Filter Press was used to determine the filtration rate through a standard filter paper and the rate at which the mudcake thickness increases on the standard filter paper under standard test conditions. This test is indicative of the rate at which permeable formations are sealed by the deposition of a mudcake after being penetrated by the bit.

The flow of mud filtrate through a mudcake is described by Darcy's law (Bourgoyne et al. 1991). The volume of filtrate is given by

$$V_f = \sqrt{2k\Delta p \left(\frac{f_{sc}}{f_{sm}} - 1\right) A \frac{\sqrt{t}}{\sqrt{\mu_f}}}, \tag{1}$$

where

k : permeability of the mudcake (D)

Δp : pressure drop across the mudcake (atm)

f_{sc} : volume fraction of solids in the cake

f_{sm} : volume fraction of solids in the mud

A : area of the filter paper (cm^2)

t : time

μ_f : viscosity of the mud filtrate (cp)

According to the standard API practice (API 13B-1), filter paper with a diameter of 3.5 in (Fann N87000) was used and all tests were operated at a pressure of 100 psig. The filtrate volume collected in a 30 minutes time period was recorded and plotted as a

function of the square root of the time. Note that Eq. (1) indicates that the filtrate volume is proportional to the square root of the time period used.

1.2.6. Swelling

A Fann Linear Swell Meter (LSM) Model 2000 was used to measure the swelling of shale pellets.

Shale rock was ground with mortar and pestle to pass through a 200-mesh sieve. Before creating a pellet the ground shale was equilibrated to standard room humidity and temperature conditions. We refer to this as room-dry condition hereafter. Moisture content of the room-dry ground shale was determined as follows. First, we weighed approximately a 5 g portion of the ground sample then dried this sample in an oven at 220 ° F for 2 hours. Next, we weighed the sample after it cooled to room temperature, and then calculated the moisture content. Then, deionized water was added and mixed thoroughly with mortar and pestle to make up a total of 5 wt% moisture.

Figure 4 LSM sample setup

Bentonite pellets was also created. Room-dry bentonite powder was used without adjusting moisture content because room-dry bentonite contained approximately 10 wt% moisture.

To make a pellet, 20 g of the prepared shale or bentonite powder was placed in the compaction cell between two plastic discs and a standard level of 10,000 psi load was applied for 1.5 hours and then released. The pellet was placed between a clear acrylic disc and a Teflon plunger cap. The pellet and end pieces were then wrapped with a screen that fits tightly around the sample. This screen contains the sample and prevents slaking or dispersion when it is exposed to the test fluid. It also largely prevents lateral swelling, such that nearly all the swelling occurs vertically, or parallel to the sample axis. The porous screen allows complete physical and chemical contact between the sample and the test fluid.

To start a test, the screened sample was placed in the LSM apparatus and the swelling indicator, which was connected to a high-precision linear variable differential transformer, was brought down into contact with the Teflon piece that sat on top of the sample (and (3)). The test fluid was then poured into the apparatus such that it completely covered the sample. A computer automatically recorded sample vertical swelling vs. time.

1.2.7. Hot-Rolling

An OFITE 4 Roller Oven was used to determine the effect of temperature on drilling muds. 450 mL of drilling mud was placed into a 500 mL aging cell and then pressurized with nitrogen gas. The aging cell was then placed into the roller oven and rolled at 16 rpm at 250 °F for 16 hours. After the hot-rolling, the mud sample was retrieved from the cell and then analyzed.

1.2.8. Elemental Analysis

A Thermo Fisher Nicolet iS10 + Nicolet Continuμm was used to determine the composition of the substances adsorbed on bentonite. Mud samples were centrifuged, thoroughly washed with distilled water, and then dried. The dried samples were placed in the apparatus and analyzed. These analyses were performed by Kuraray co., ltd., which provided us with polyvinyl alcohol samples.

1.3. Results and Discussion

1.3.1. Clarification of Incompatibility

To clarify the incompatibility between the oligomeric polyetheramine shale inhibitor and bentonite, we formulated the simple muds shown in Table 3. Because the exact chemical structure of the oligomeric polyetheramine used in previous studies was not disclosed, we chose poly(propylene glycol) bis(2-aminopropyl ether) ($\overline{M_n} \sim 230$) (PPGBAE) as a likely example of the oligomeric polyetheramine (Figure 5). Then we measured rheological properties (Figure 6) and fluid loss properties (Figure 7). We also measured the properties of 3 wt% bentonite mud as a control experiment.

Table 3 Mud composition to clarify the incompatibility between oligomeric polyetheramine and bentonite

Additive	Function	Concentration
Wyoming bentonite	Viscosifier Filtration control	3 wt%
PPGBAE or KCl	Shale inhibitor	1 wt% or 10 wt%
HCl or KOH	pH control	pH = 10
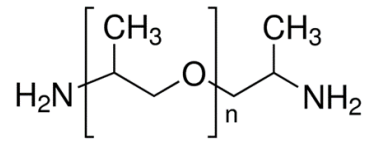
Figure 5 Chemical structure of poly(propylene glycol) bis(2-aminopropyl ether) (PPGBAE)
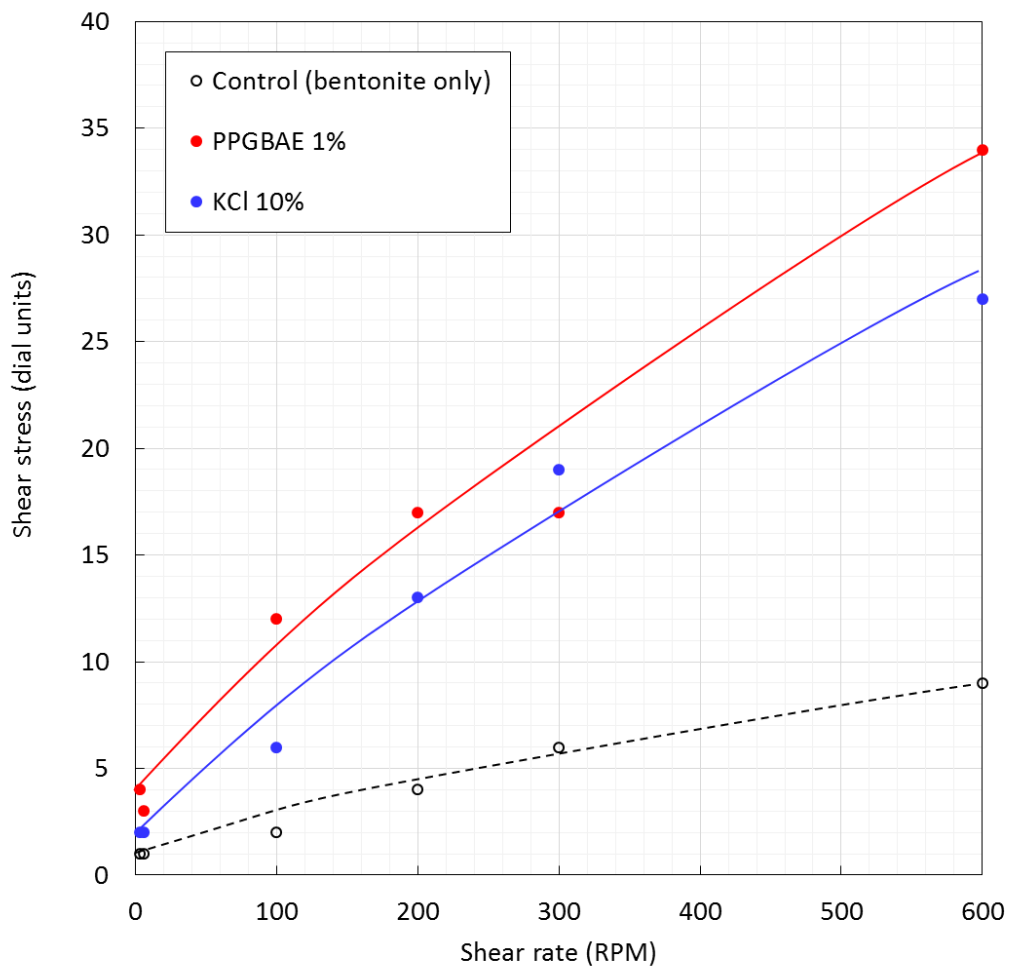
Figure 6 Variation of shear stress with shear rate in simple PPGBAE mud (red circles) and KCl mud (blue circles)
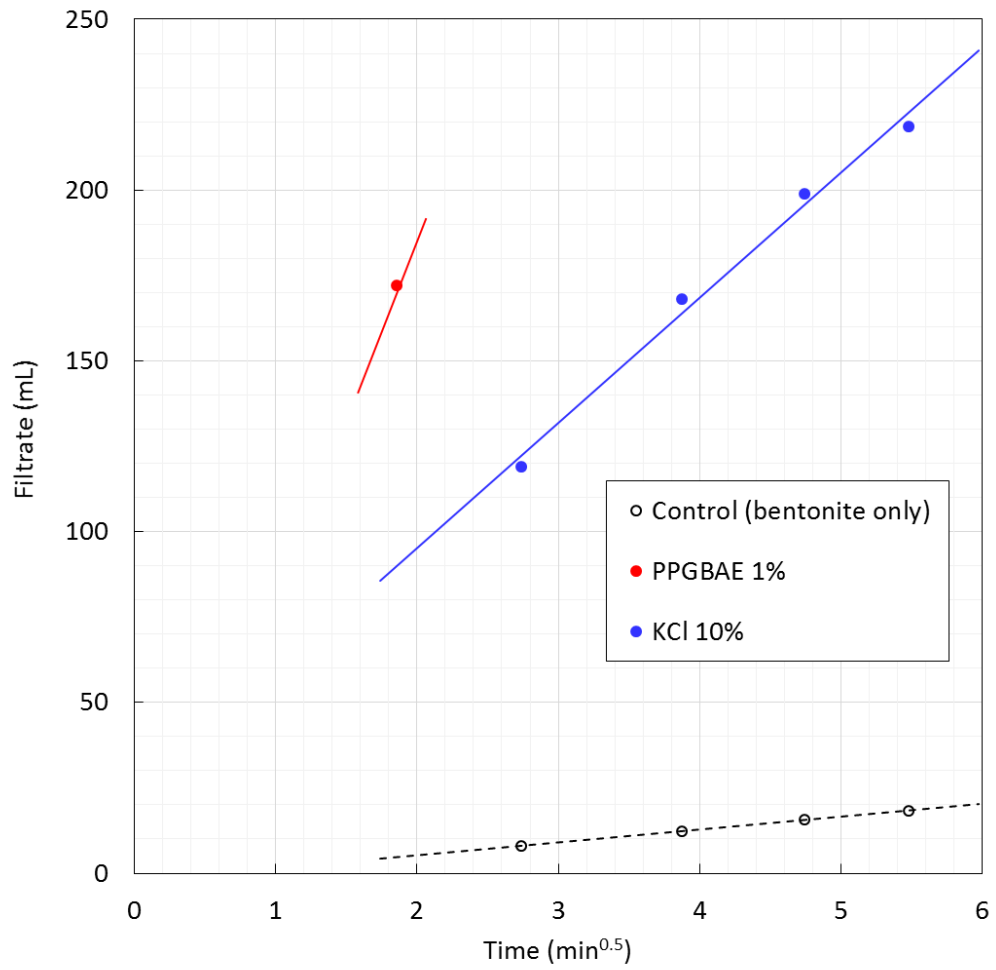
Figure 7 Fluid loss properties of simple PPGBAE (red circle) mud and KCl mud (blue circles)

As shown in Figure 6, a control experiment with no shale inhibitor showed a typical rheological profile (open black circles). With PPGBAE or KCl, on the other hand, the muds were flocculated and the shear stress raised significantly (red and blue filled circles, respectively).

As shown in Figure 7, volume of the filtrate significantly increased by adding PPGBAE (red filled circle) or KCl (blue filled circles) compared to a control experiment (open black circles).

According to the above, we hereby clarified that shale inhibitors severely impaired the mud properties, in other words, shale inhibitors were inherently incompatible with bentonite.

1.3.2. Polyvinyl Alcohol

In this section we introduce polyvinyl alcohol (PVOH) as a new polymeric deflocculant and check how PVOH affects the mud properties.

PVOH is a unique water soluble polymer with the chemical structure shown in Figure 8.

$$(CH_2 - CH)_n \qquad (CH_2 - CH)_m$$
$$O-C-CH_3 \qquad OH$$
$$O$$
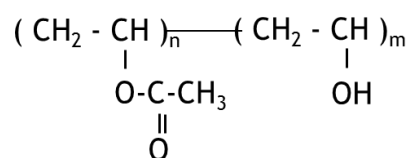
Figure 8 Chemical structure of polyvinyl alcohol

PVOH forms transparent film. And it is used in a variety of fields such as paper coating, adhesive, and so on. Adsorption of PVOH on attapulgite clay has been studied (Chang et al. 1992). They studied the effect of the adsorption of PVOH on the rheology of attapulgite suspensions. Then we came up with an idea that PVOH was possibly useful for drilling muds as a deflocculant. In other words, PVOH possibly keeps shale inhibitors from approaching bentonite by adsorbing on it.

PVOH is characterized by two parameters. One is degree of polymerization (DP) defined as the total number of repeating units ($m + n$ in Figure 8). As DP increases, solubility decreases and viscosity increases. The other one is degree of hydrolysis (DH) defined as the percentage of hydroxyl groups ($m/(m + n) \times 100$ in Figure 8, %). As DH increases, solubility significantly decreases and viscosity slightly increases because the number of the hydroxyl bonds between OH groups increases, and hence the PVOH molecules are bound more strongly. The nomenclature of PVOH is shown in Figure 9.

$$\underline{5\text{-}98}$$

DH (%)

Viscosity of 4% aqueous solution (cp)
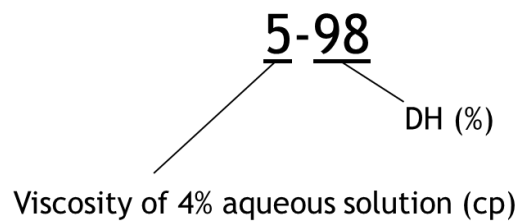
Figure 9 Nomenclature of PVOH

Taking 5-98 as an example, five means that the viscosity of 4% aqueous solution of the PVOH is 5 cp. Note that the viscosity has directly to do with molecular weight, and so does with DP. Ninety eight means the degree of hydrolysis of the PVOH is 98 %. Table 4 shows the list of PVOH samples tested in this study. All samples were supplied by Kuraray co., ltd. by the name of Kuraray Poval.

Table 4 List of tested PVOH samples

Sample name	Degree of polymerization (DP)	Degree of hydrolysis (DH) (%)
3-80	300	80
3-88	300	88
3-98	300	98
5-98	500	98
26-80	1700	80
22-88	1700	88
28-98	1700	98
29-99	1700	99
60-98	2400	98

1.3.3. Effect of PVOH

First of all, we need to confirm that PVOH is compatible with drilling muds. In order to check how PVOH affects the mud properties, we formulated the simple muds using various amount of polymers without shale inhibitor shown in Table 5. We compared PVOH to carboxymethyl cellulose (CMC), which is commonly used as a filtration control agent. And we measured rheological properties (Figure 10 and Figure 11) and fluid loss properties (Figure 12 and Figure 13).

Table 5 Mud composition to compare CMC and PVOH

Additive	Function	Concentration
Wyoming bentonite	Viscosifier Filtration control	5 wt%
Carboxymethyl cellulose	Filtration control	0 – 0.2 wt%
PVOH (5-98)	To be determined	0 – 0.2 wt%
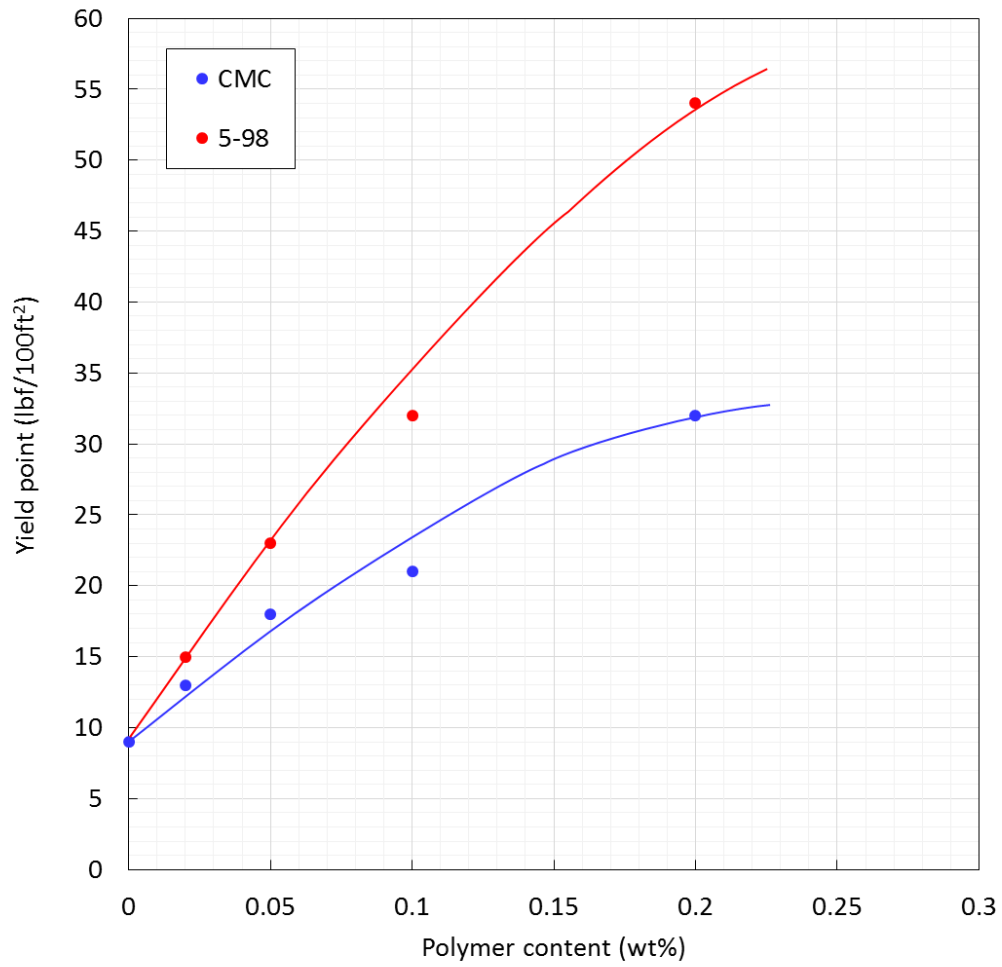
Figure 10 Variation of yield point with polymer content comparing PVOH (red circles) and CMC (blue circles)
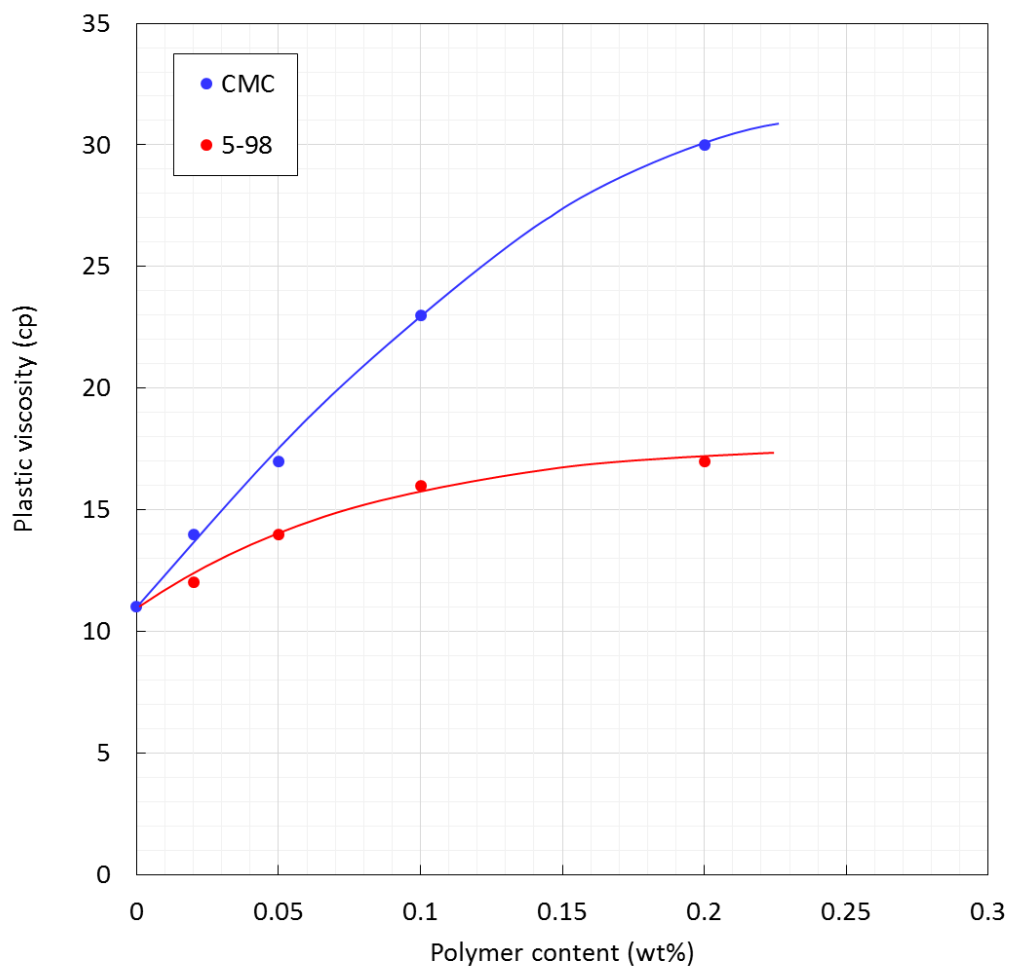
Figure 11 Variation of plastic viscosity with polymer content comparing PVOH (red circles) and CMC (blue circles)
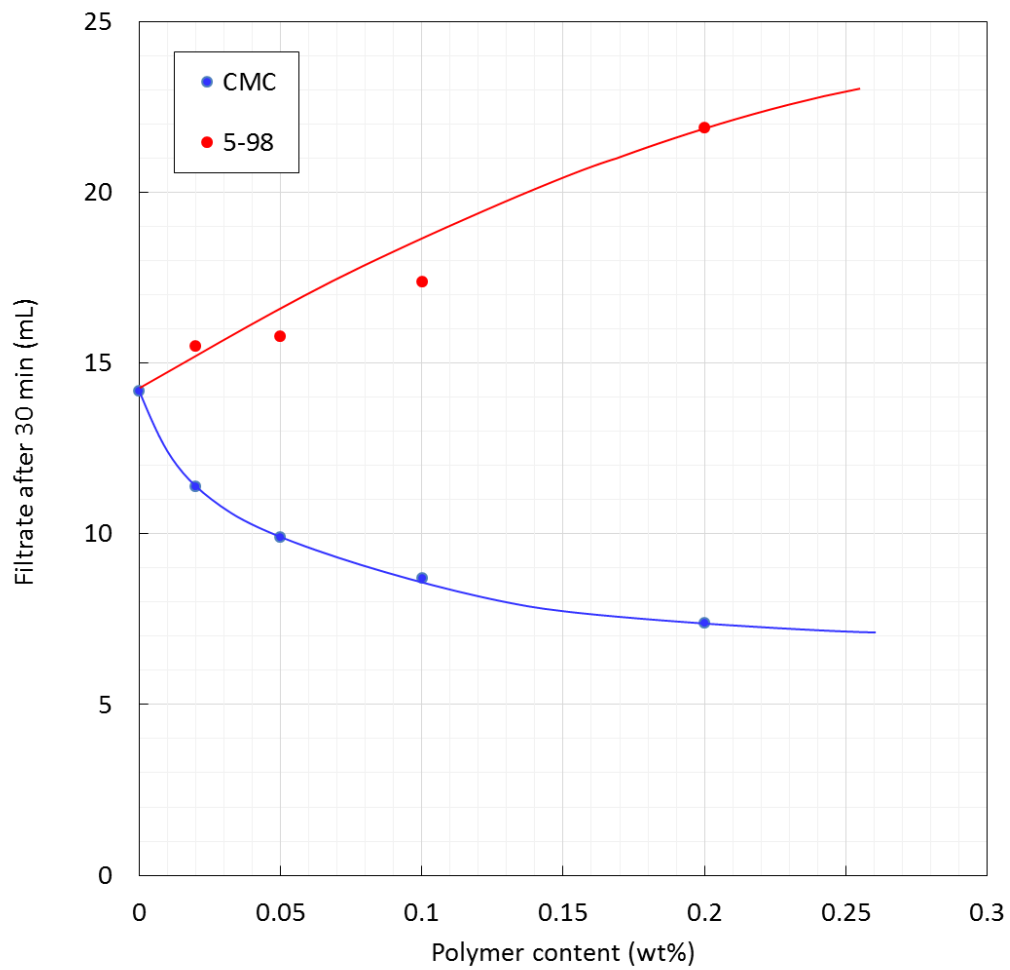
Figure 12 Comparison of fluid loss properties between PVOH (red circles) and CMC (blue circles) as a function of polymer content
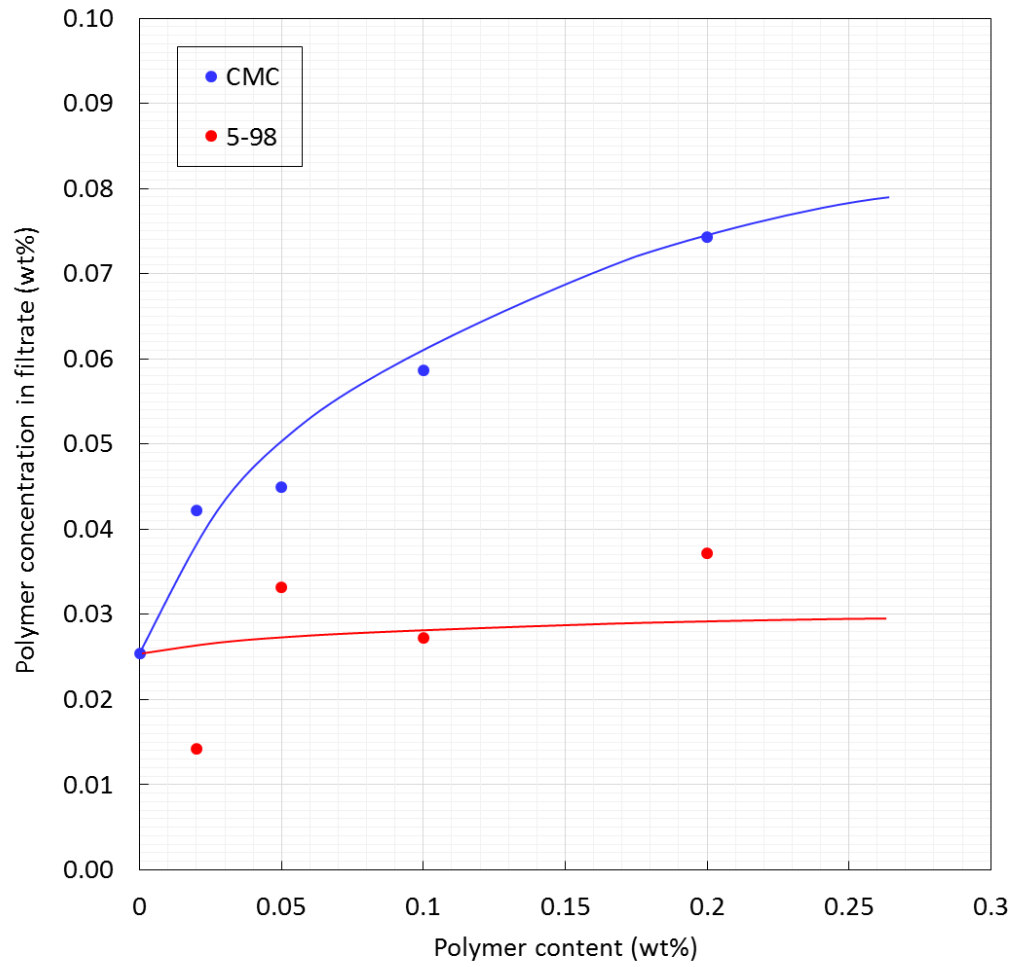
Figure 13 Variation of polymer concentration in filtrate with polymer content in the mud comparing PVOH (red circles) and CMC (blue circles)

As shown in Figure 10, the addition of PVOH increased the yield point more significantly than that of CMC did.

As shown in Figure 11, PVOH did not significantly affect the plastic viscosity, whereas CMC significantly increased it as opposed to the yield point discussed above. This implies that PVOH would work as a deflocculant without significantly affecting mud rheology.

As shown in Figure 12, the fluid loss increased as the PVOH content was increased (red circles), whereas it decreased as the CMC content increased (blue circles). Note that this is why CMC is used as a filtration control agent. Then we performed another experiment. We measured the polymer concentration in the filtrate. It means how much polymer comes out from the mud to the filtrate. Polymer concentration was calculated by

$$Polymer\ concentration = \frac{mass\ of\ dried\ filtrate - tare}{mass\ of\ filtrate - tare} \times 100\ (\%).$$

As shown in Figure 13, the more CMC was added, the more CMC came out (blue circles), whereas no matter how much PVOH was added, almost no PVOH came out (red circles). This means PVOH is much more adsorbent to bentonite than CMC is. Thus, as we discussed in 1.3.2, PVOH possibly keeps shale inhibitors from approaching bentonite by adsorbing and covering bentonite.

1.3.4. Effect of DP and DH

In this section, we formulated the simple muds shown in Table 6 in order to check the effect of degree of polymerization (DP) and degree of hydrolysis (DH) of PVOH on mud properties without shale inhibitors. The results of rheological properties and fluid loss properties are shown in Figure 14, Figure 15, Figure 16, and Figure 17, respectively.

Table 6 Mud composition to check the effect of DP and DH on mud properties

Additive	Function	Concentration
Wyoming bentonite	Viscosifier Filtration control	6.3 wt%
PVOH (5-98, 28-98, 60-98, 26-80, 22-88, 29-99)	To be determined	0.1 wt%
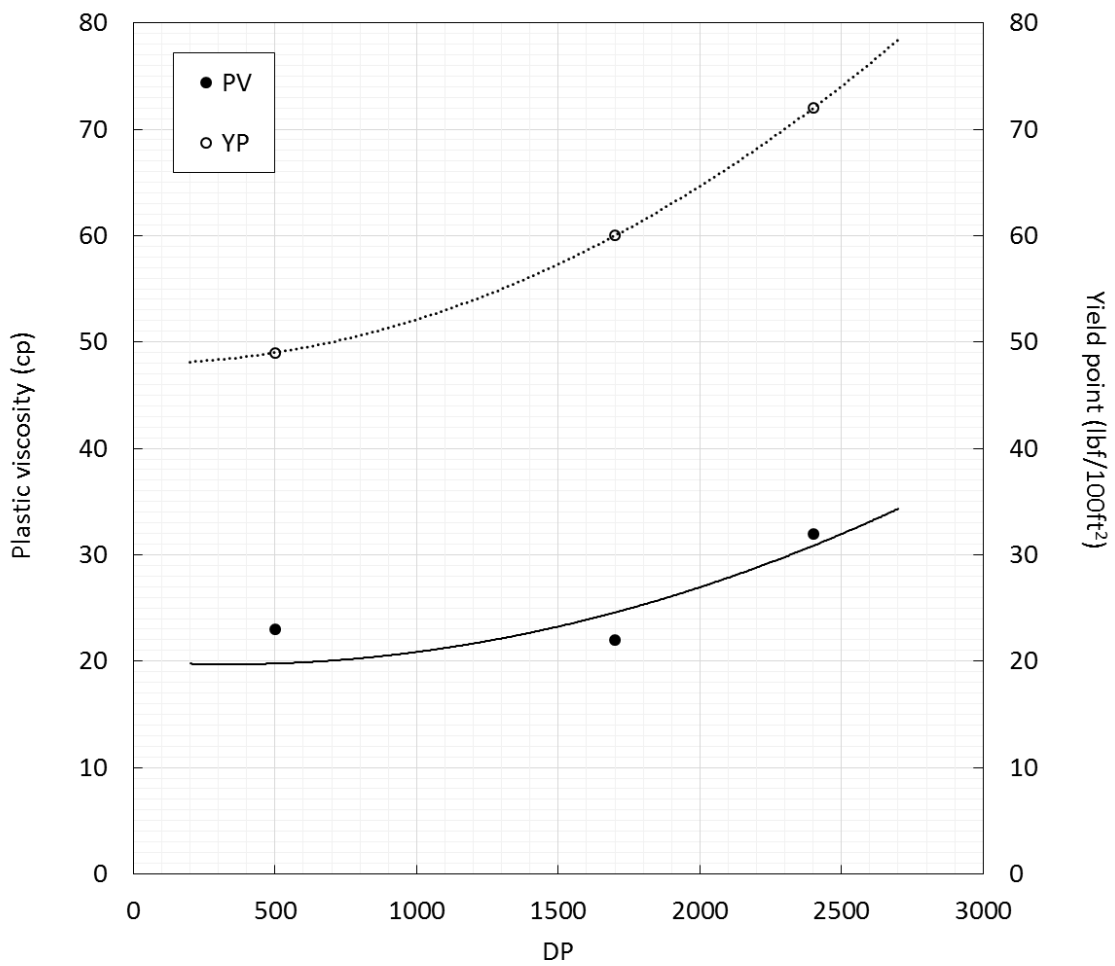
Figure 14 Variation of plastic viscosity (filled circles) and yield point (open circles) as a function of degree of polymerization. All PVOHs have the same DH of 98 %
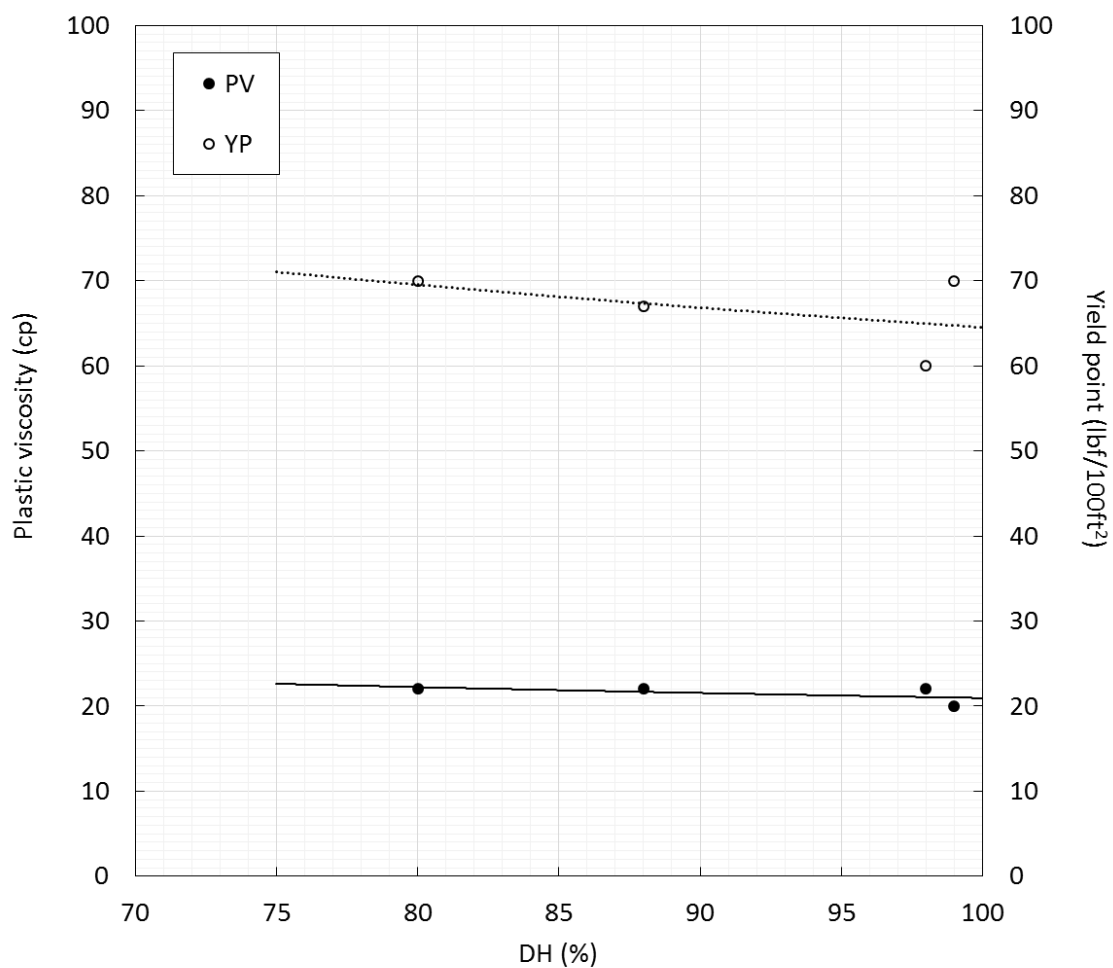
Figure 15 Variation of plastic viscosity (filled circles) and yield point (open circles) as a function of degree of hydrolysis. All PVOHs have the same DP of 1700
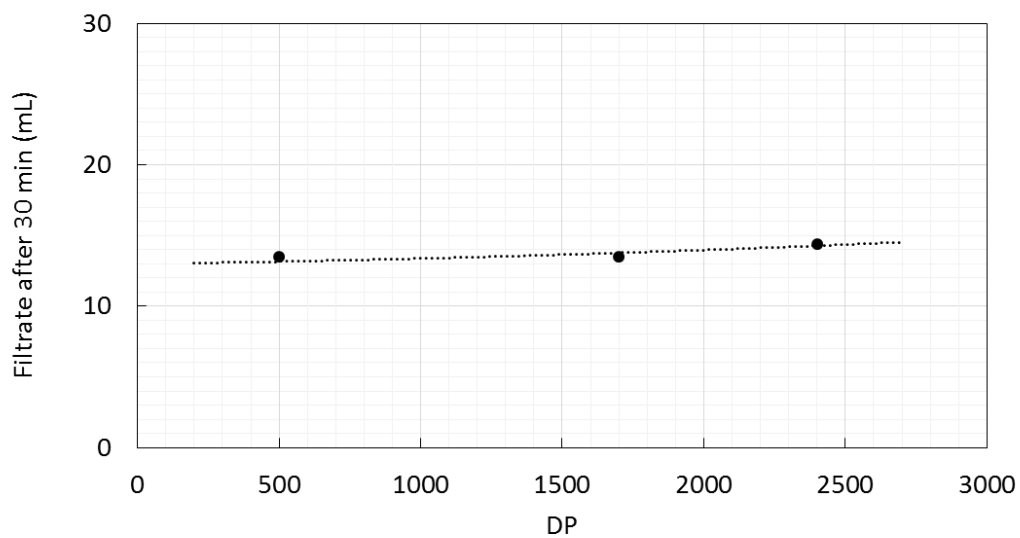
Figure 16 Variation of fluid loss as a function of degree of polymerization. All PVOHs have the same DH of 98 %
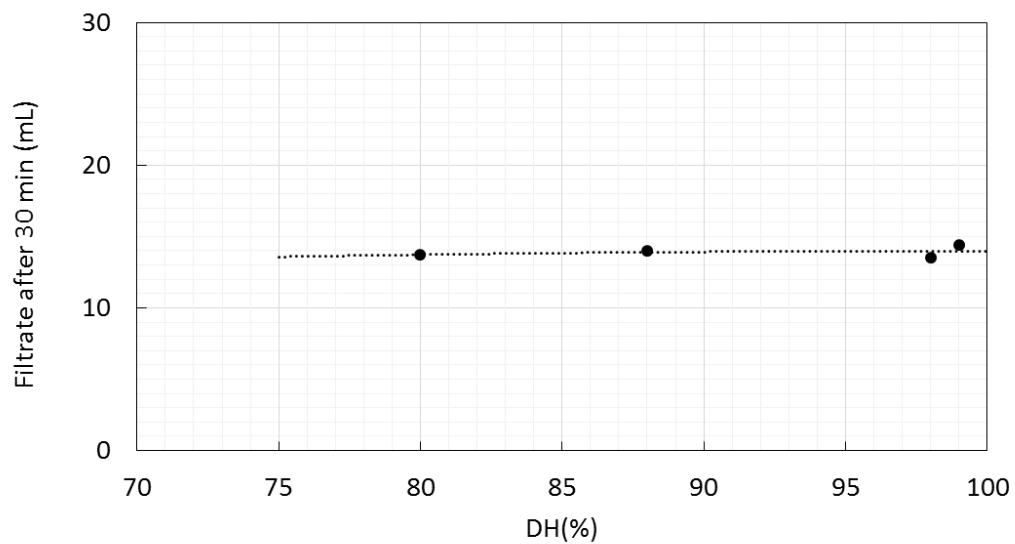
Figure 17 Variation of fluid loss as a function of degree of hydrolysis. All PVOHs have the same DP of 1700

Figure 14 shows the effect of DP on PV and YP. In this experiment, 3 PVOHs (5-98, 28-98, and 60-98) were used. They have 3 different degrees of polymerization, while they all have the same DH of 98 %. As shown in the figure, high DP led to high PV and YP because of the high viscosity of the PVOH.

Figure 15 shows the effect of DH on PV and YP. In this experiment, 4 PVOHs (26-80, 22-88, 28-98, and 29-99) were used. They have 4 different degrees of hydrolysis, while they all have the same DP of 1700. As opposed to the effect of DP, DH had minimal effect on PV (filled circles) and YP (open circles) because DH did not have significant effect on the viscosity of PVOH as we discussed in 1.3.2.

Figure 16 and Figure 17 show the effect of DP and DH on fluid loss properties, respectively. The same 3 PVOHs (5-98, 28-98, and 60-98) and 4 PVOHs (26-80, 22-88, 28-98, and 29-99) were used for the measurements shown in Figure 16 and Figure 17, respectively. Unlike the rheological properties, either DP or DH did not affect the fluid loss properties.

1.3.5. Deflocculant

1.3.5.1. Performance of PVOH as deflocculant

In this section we check the performance of PVOH as a deflocculant in the presence of shale inhibitor compared to lignosulfonate, which is commonly used as a deflocculant for KCl mud. We formulated the simple muds with KCl or PPGBAE as a shale inhibitor and lignosulfonate or PVOH as a deflocculant shown in Table 7 and measured rheological properties (Figure 18 and Figure 19) and fluid loss properties (Figure 20 and Figure 21). In this experiment, PVOH 3-98 was used because smaller DP has a less effect on the rheology as we discussed in 1.3.4. We also measured the properties of 3 wt% bentonite mud as a control experiment.

Table 7 Mud composition to check the performance of PVOH as deflocculant

Additive	Function	Concentration
Wyoming bentonite	Viscosifier Filtration control	3 wt%
PPGBAE or KCl	Shale inhibitor	1 or 10 wt%
PVOH (3-98) or Lignosulfonate	Deflocculant	0.5 wt%
HCl or KOH	pH control	pH = 10
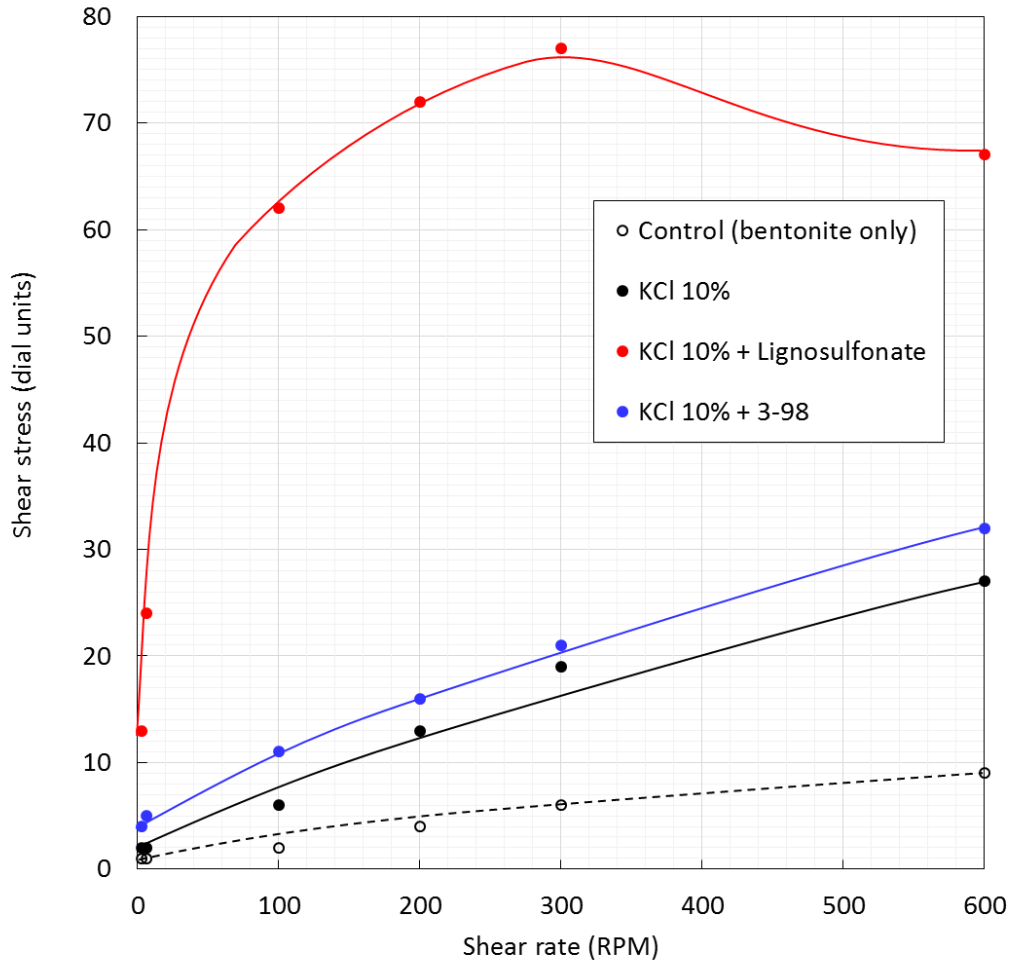
Figure 18 Variation of shear stress with shear rate in simple KCl mud (filled black circles), KCl mud with lignosulfonate (red circles), KCl mud with PVOH (blue circles)
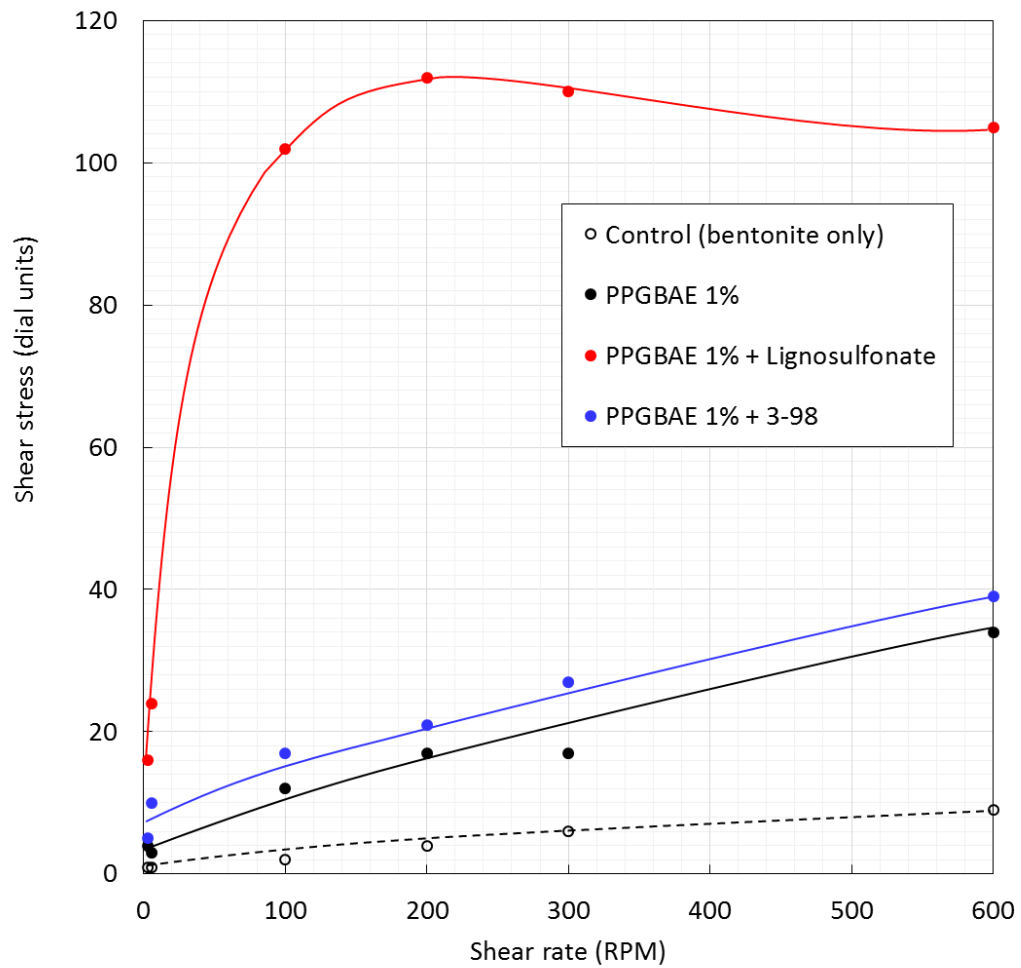
Figure 19 Variation of shear stress with shear rate in simple PPGBAE mud (filled black circles), PPGBAE mud with lignosulfonate (red circles), PPGBAE mud with PVOH (blue circles)
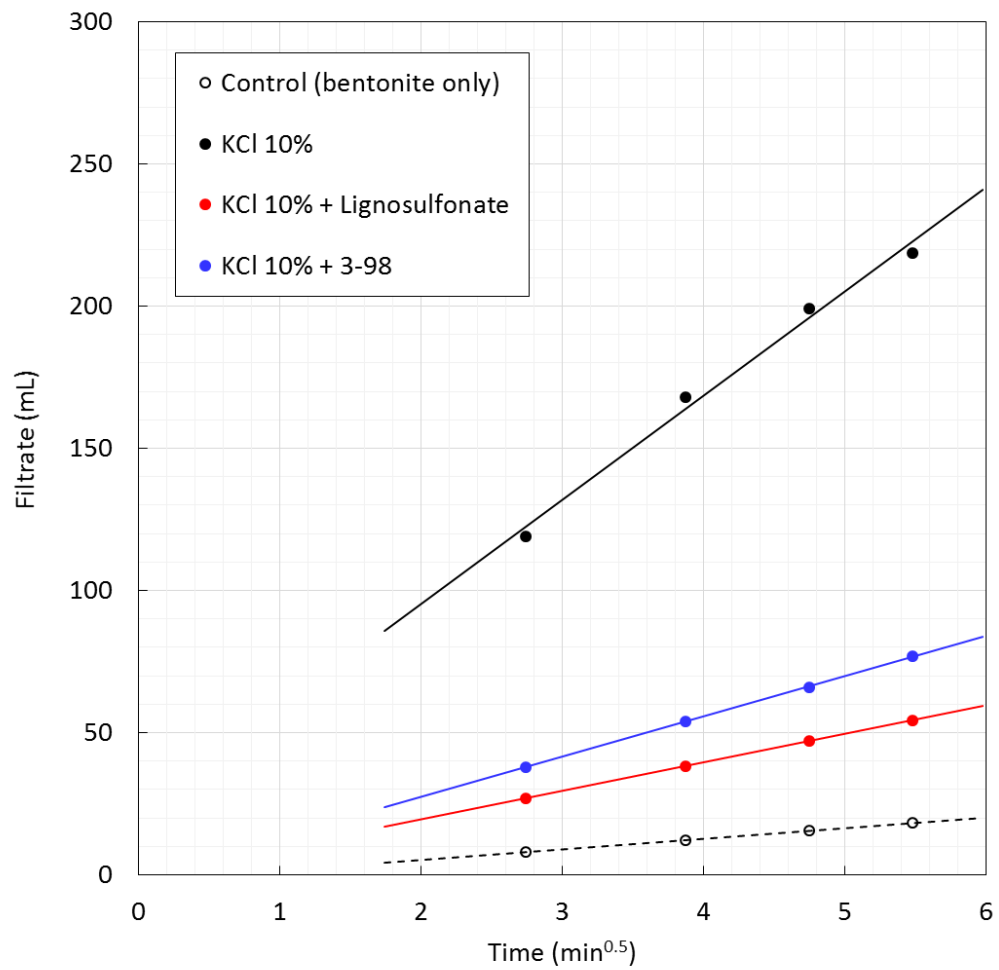
Figure 20 Fluid loss properties of simple KCl mud (filled black circles), KCl mud with lignosulfonate (red circles), and KCl mud with PVOH (blue circles)
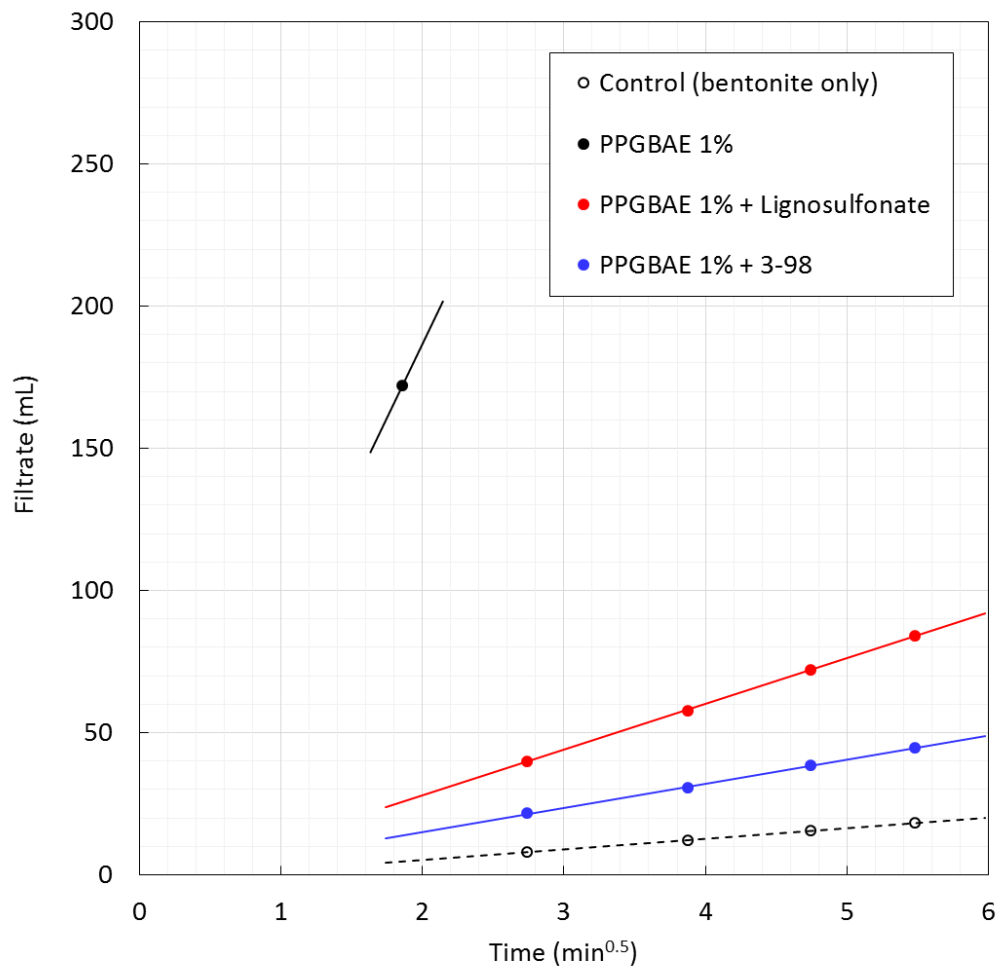
Figure 21 Fluid loss properties of simple PPGBAE mud (filled black circle), PPGBAE mud with lignosulfonate (red circles), and PPGBAE mud with PVOH (blue circles)

In Figure 18, KCl was used as a shale inhibitor. In the presence of KCl, the mud was flocculated (filled black circles). Even with lignosulfonate as a deflocculant, the mud was still flocculated and the mud showed abnormal rheology profile (red circles). With PVOH (3-98) as a deflocculant, on the other hand, even though the shear stress was increased to some extent, no floc was observed and the rheology profile was normal.

In Figure 19, PPGBAE was used as a shale inhibitor. Note that PPGBAE content is one tenth of that of KCl because PPGBAE is much more effective. Exactly the same tendency was found in this graph. PPGBAE flocculated the mud and lignosulfonate did not help, and PVOH (3-98) brought the rheology profile back to normal.

Figure 20 shows the fluid loss properties of simple KCl muds. Compared to the control experiment (open black circles), the fluid loss significantly increased by adding KCl (filled black circles). With lignosulfonate as a deflocculant, even though the mud was still flocculated as we mentioned above, lignosulfonate did help reduce the fluid loss (red circles). PVOH (3-98) also helped reduce the fluid loss (filled blue circles).

Figure 21 shows the fluid loss properties of simple PPGBAE muds. The tendency was almost the same as the KCl muds we discussed above but slightly different. The fluid loss significantly increased by adding PPGBEA (filled black circles), lignosulfonate reduced the fluid loss (red circles), and PVOH (3-98) reduced it even more (blue circles). Here we found that PVOH worked with PPGBAE better than with KCl.

1.3.5.2. Effect of DH

In this section, we formulated the simple muds with KCl or PPGBAE as a shale inhibitor and PVOH as a deflocculant shown in Table 8 in order to check the effect of degree of hydrolysis (DH) of PVOH on the performance of the PVOH in terms of fluid loss property. The results of fluid loss measurement are shown in Figure 22.

Table 8 Mud composition to check the effect of DH on the performance of PVOH as deflocculant

Additive	Function	Concentration
Wyoming bentonite	Viscosifier Filtration control	3.0 wt%
PPGBAE or KCl	Shale inhibitor	1 or 10 wt%
PVOH (3-80, 3-88, 3-98)	Deflocculant	1 wt%
HCl or KOH	pH control	pH = 10
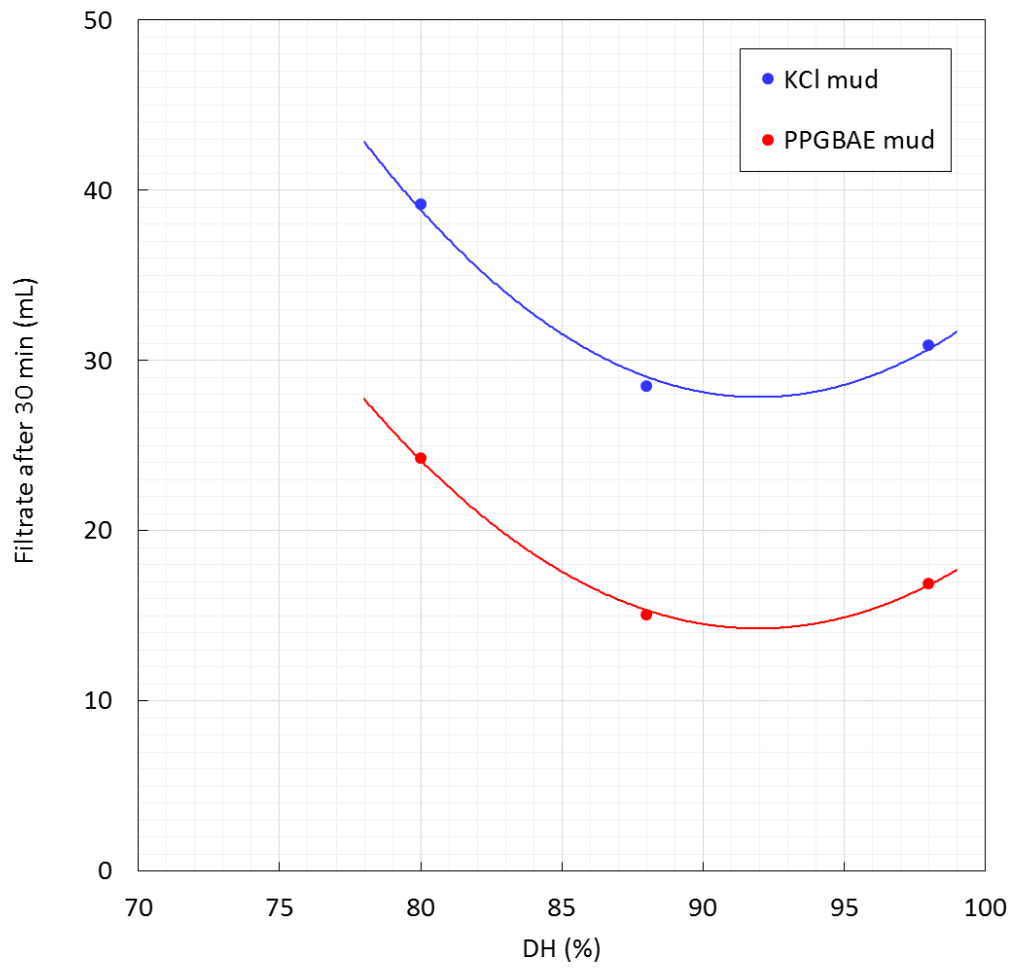
Figure 22 Effect of DH on fluid loss properties in KCl mud (blue circles) and PPGBAE mud (red circles)

In this experiment, 3 PVOHs (3-80, 3-88, and 3-98) were used. They have 3 different degrees of hydrolysis, while they all have the same DP of 300. As we discussed in 1.3.4, DH did not affect fluid loss properties without shale inhibitor. In the presence of shale inhibitor, on the other hand, as shown in Figure 22, DH 88% worked the best as a deflocculant in terms of fluid loss property regardless of whether KCl or PPGBAE was used as a shale inhibitor.

According to the above, PVOH 3-88 would be the best choice because it has the best performance as a deflocculant in terms of fluid loss properties, while it has the minimal effect on the rheological properties.

1.3.6. Working Mechanism of PVOH

In this section, we performed simple solubility tests and fluid loss tests in order to discover the working mechanism of PVOH. We also discuss the results of elemental analyses performed by Kuraray co., ltd. to understand the mechanism more clearly.

1.3.6.1. PPGBAE vs KCl

In order to discover the reason why PVOH worked with PPGBAE better than with KCl, we formulated the simple solutions shown in Table 9 and performed simple solubility tests (see caption of Figure 23) to check the compatibility between PVOH, and KCl or PPGBAE. The results are shown in Figure 23.

Table 9 Solution composition for simple solubility tests

Solution	Composition (wt%)		
	KCl	PPGBAE	PVOH (3-88)
a-1	10	-	2
a-2	20	-	2
b-1	-	1	2
b-2	-	2	2
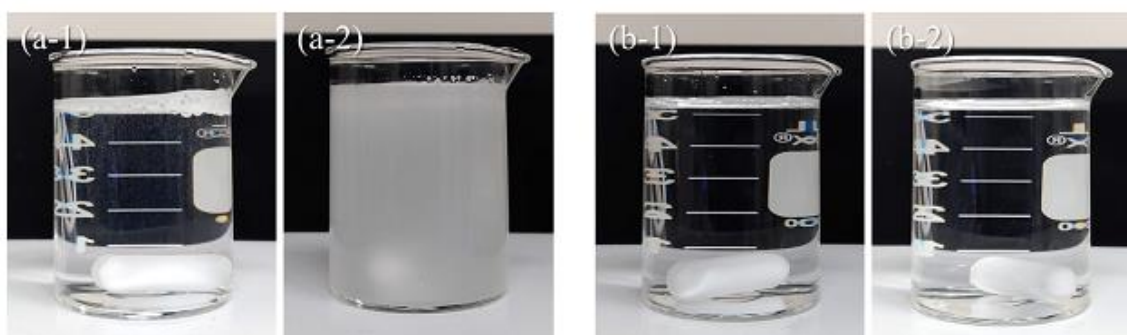
Figure 23 Solubility test. Either KCl or PPGBAE was added to PVOH (3-88) aqueous solution such that the resulting composition of each solution was those shown in Table 9

As shown in Figure 23, when 10 wt% of KCl was added into 2 wt% PVOH 3-88 aqueous solution, nothing happened and KCl just dissolved (a-1). When 20 wt% of KCl was added, the solution became turbid (a-2). The same test was performed on PPGBAE. Even with 2 wt% of PPGBAE, it just dissolved (b-1), (b-2). Here it was found that PVOH was not compatible with high concentration KCl (salting-out effect) and that was probably why PVOH worked with PPGBAE better than with KCl.

1.3.6.2. Working Mechanism

As we discussed in 1.3.2, we hypothesized that PVOH would work as a deflocculant by adsorbing on bentonite and thus keeping shale inhibitors from approaching it.

In order to confirm the hypothesis, we formulated the simple muds with various compositions shown in Table 10 and measured fluid loss properties (Figure 24). We basically formulated several muds with a given PPGBAE content along with various PVOH contents.

Table 10 Mud composition with various PPGBAE and PVOH concentration to discover the working mechanism of PVOH

Additive	Function	Concentration
Wyoming bentonite	Viscosifier Filtration control	3 wt%
PPGBAE	Shale inhibitor	1 - 2 wt%
PVOH (3-88)	Deflocculant	0.5 - 5 wt%
HCl	pH control	pH = 10
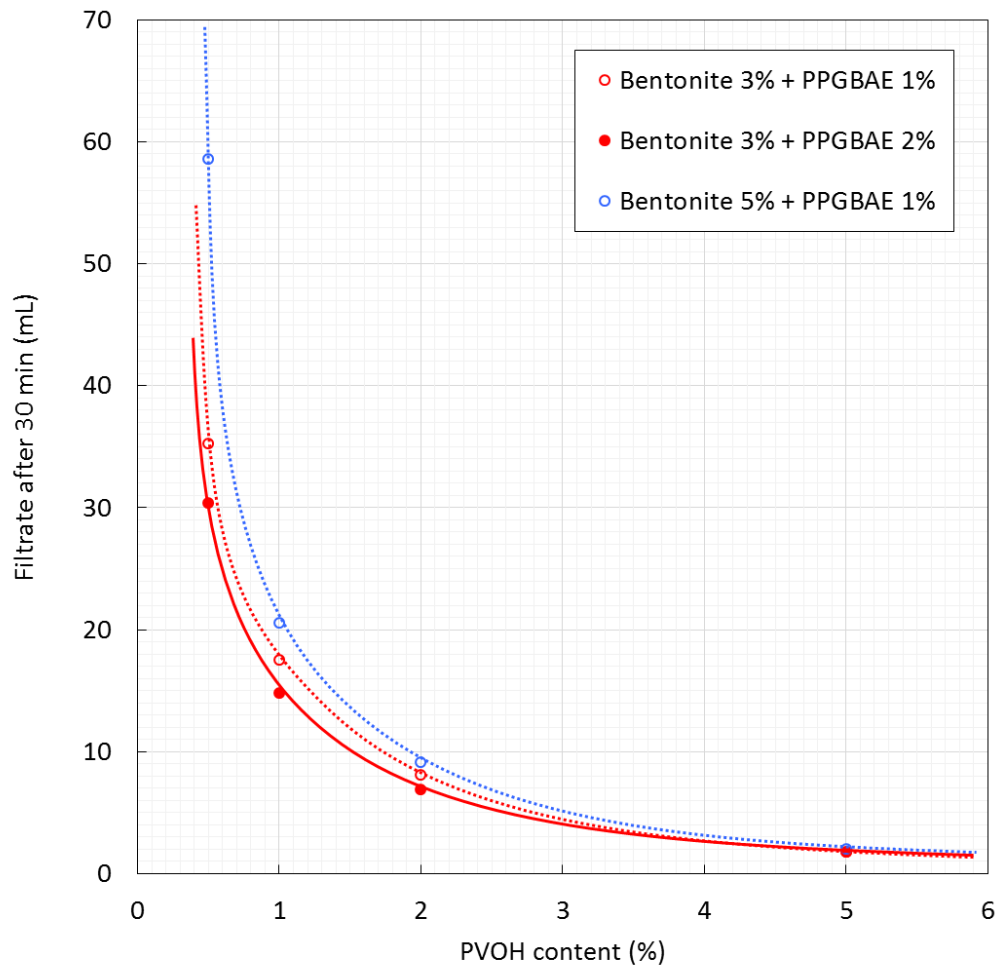
**Figure 24 Variation of the volume of filtrate with PVOH content in PPGBAE muds
with different bentonite/PPGBAE ratio**

As shown in Figure 24, when the PPGBAE content was increased from 1 wt% to 2 wt%, the volume of the filtrate did not change much (filled and open red circles). However, when the bentonite content was increased from 3 wt% to 5 wt%, filtrate significantly increased and more PVOH was required to achieve the same fluid loss level. Practically, we would recommend to use the same concentration of PVOH as bentonite.
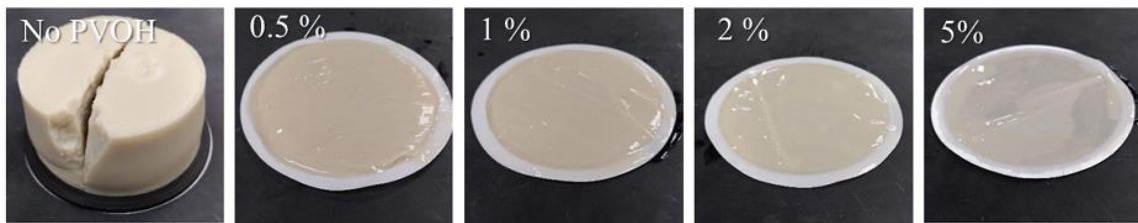
Figure 25 Appearance of filter cake. Mud composition: Bentonite 3 wt% + PPGBAE 2 wt% (solid red curve in Figure 24)

The appearance of the filter cakes are shown in Figure 25. The more PVOH was used, the thinner and the denser filter cake was obtained, and hence the less fluid loss level was achieved.
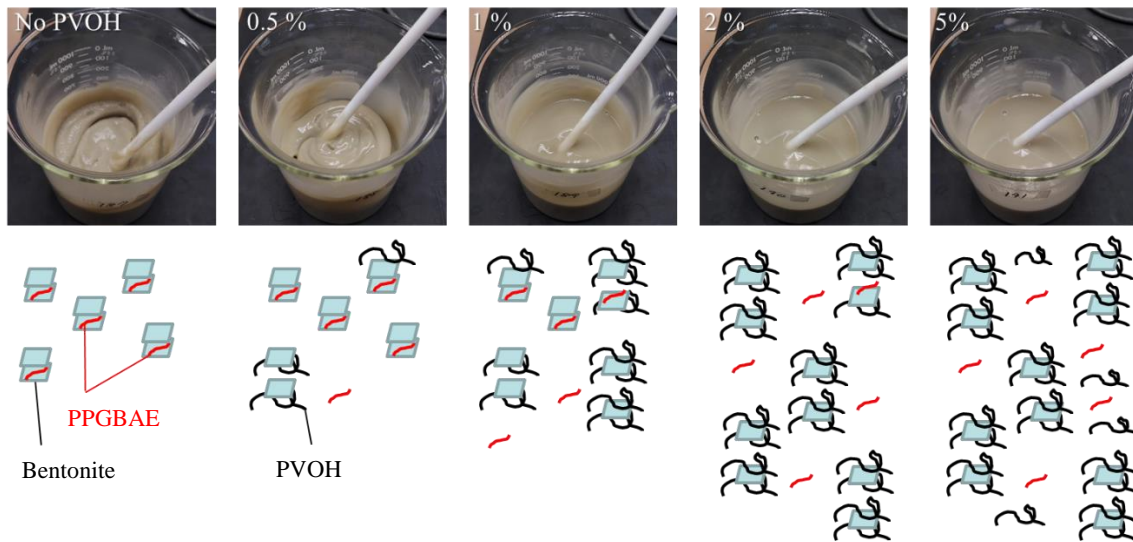
Figure 26 Appearance of mud and schematic drawing describing what each photo implies. Mud composition: Bentonite 5 wt% + PPGBAE 1 wt% (dashed blue curve in Figure 24)

Now we discuss the working mechanism of PVOH. As shown in Figure 26, with no PVOH it did not look like a mud. This is what we referred to as flocculation. With 0.5 wt% of PVOH, it started looking like a mud and it became less viscous as the PVOH content was increased. Below these photos are schematic drawings describing what each photo implies. With no PVOH, like previous research described, PPGBAE fits between bentonite platelets and keeps them from swelling. But because PVOH adsorbs on bentonite more strongly than PPGBAE does, PVOH starts kicking PPGBAE out and bentonite starts swelling. Eventually PVOH completely covers all bentonite platelets and PPGBAE can no longer approach them. This is probably why PPGBAE content does not affect fluid loss as long as there is enough PVOH in the system.

41

1.3.6.3. Elemental Analysis

In order to prove the argument in 1.3.6.2, elemental analyses were performed on the mud samples listed in Table 11. Each component was separately measured as a reference (sample 5 - 8). The results are shown in Table 12.

Table 11 Mud composition for elemental analysis

Sample	Composition (wt%)			
	Bentonite	Lignosulfonate	PVOH (3-88)	PPGBAE
1	3	0	0	0
2	3	0	0	1
3	3	1	0	1
4	3	0	1	1
5	100	0	0	0
6	0	100	0	0
7	0	0	100	0
8	0	0	0	100

Table 12 Results of elemental analysis in terms of element composition

Sample	Element composition (wt%)			
	N	C	H	S
1	0.000	0.535	0.648	0.000
2	0.688	5.804	1.460	0.000
3	0.499	6.625	0.778	0.123
4	0.167	11.780	2.299	0.000
5	0.000	0.210	1.036	0.015
6	0.000	31.347	4.175	6.821
7	0.000	52.136	8.690	0.000
8	11.310	56.182	11.549	0.000

Because PPGBAE and lignosulfonate have their characteristic element (N for PPGBAE, S for lignosulfonate), the amount of each organic substance adsorbed on bentonite can be calculated as shown in Table 13.

Table 13 Amount of the substances adsorbed on bentonite

Sample	Adsorbed amount (g/g-bentonite)		
	Lignosulfonate	PVOH (3-88)	PPGBAE
1	-	-	-
2	-	-	0.0608
3	0.0181	-	0.0441
4	-	0.2259	0.0147

As seen in Table 13, the amount of PPGBAE adsorbed on bentonite decreased by adding lignosulfonate and it decreased further by adding PVOH. And the amount of PVOH adsorbed on bentonite was much larger than that of lignosulfonate despite the fact that their amount in the mud was the same. That means PVOH adsorbs on bentonite more strongly than lignosulfonate and thus keeps PPGBAE from adsorbing on bentonite more efficiently than lignosulfonate does. This is consistent with the argument in 1.3.6.2.

From another perspective, the amount of PPGBAE that did not adsorb on bentonite increased by adding PVOH. In other words, more PPGBAE would pass through a mudcake as filtrate and contact the formation by adding PVOH. Thus, PVOH would also prevent shale swelling by increasing PPGBAE content in the filtrate, making the mud (filtrate) more inhibitive.

1.3.6.4. Effect of pH

In order to understand the working mechanism more clearly, we formulated the simple muds with various pH shown in Table 14 and measured rheological properties (Figure 27 and Figure 28) and fluid loss properties (Figure 29).

Table 14 Mud composition to check the effect of PH on mud properties

Additive	Function	Concentration
Wyoming bentonite	Viscosifier Filtration control	3 wt%
PPGBAE	Shale inhibitor	1 wt%
PVOH (3-88)	Deflocculant	1, 3 wt%
HCl	pH control	pH = 5 – 11
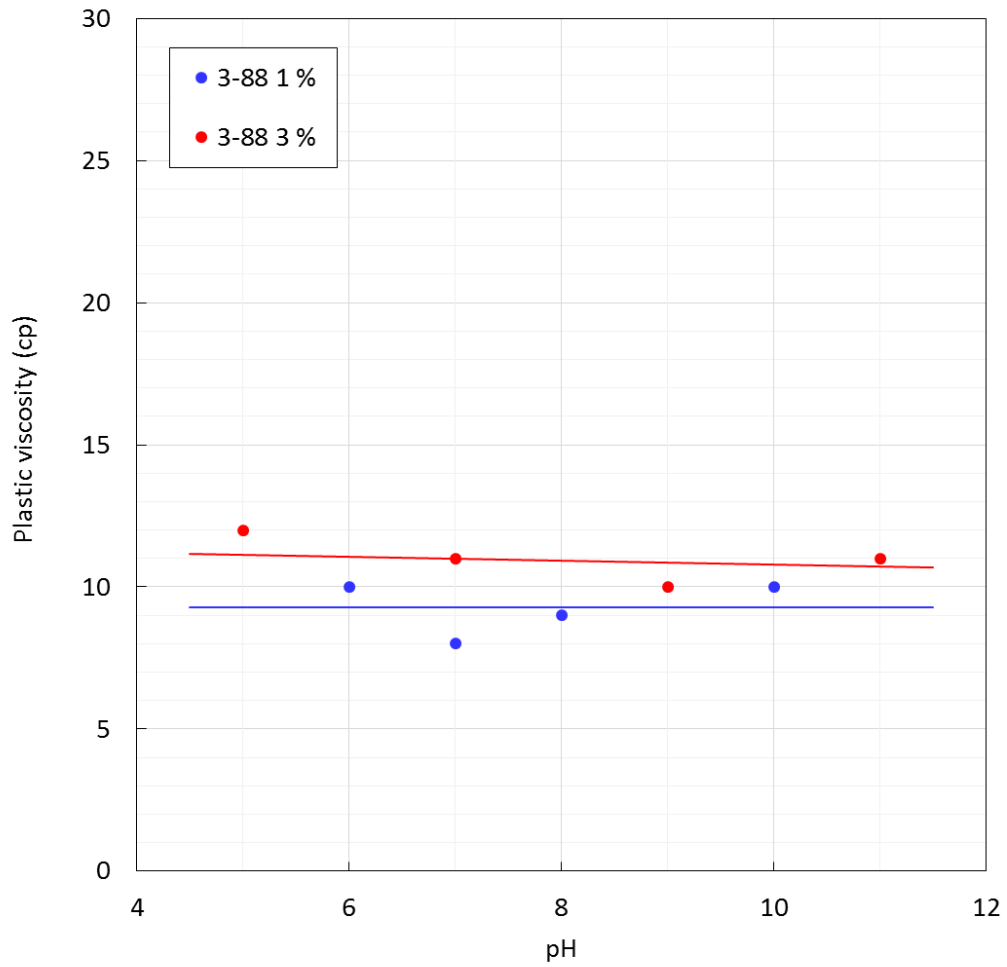
Figure 27 Variation of plastic viscosity with pH in simple PPGBAE muds with 1 wt% PVOH (blue circles) and 3 wt% PVOH (red circles)
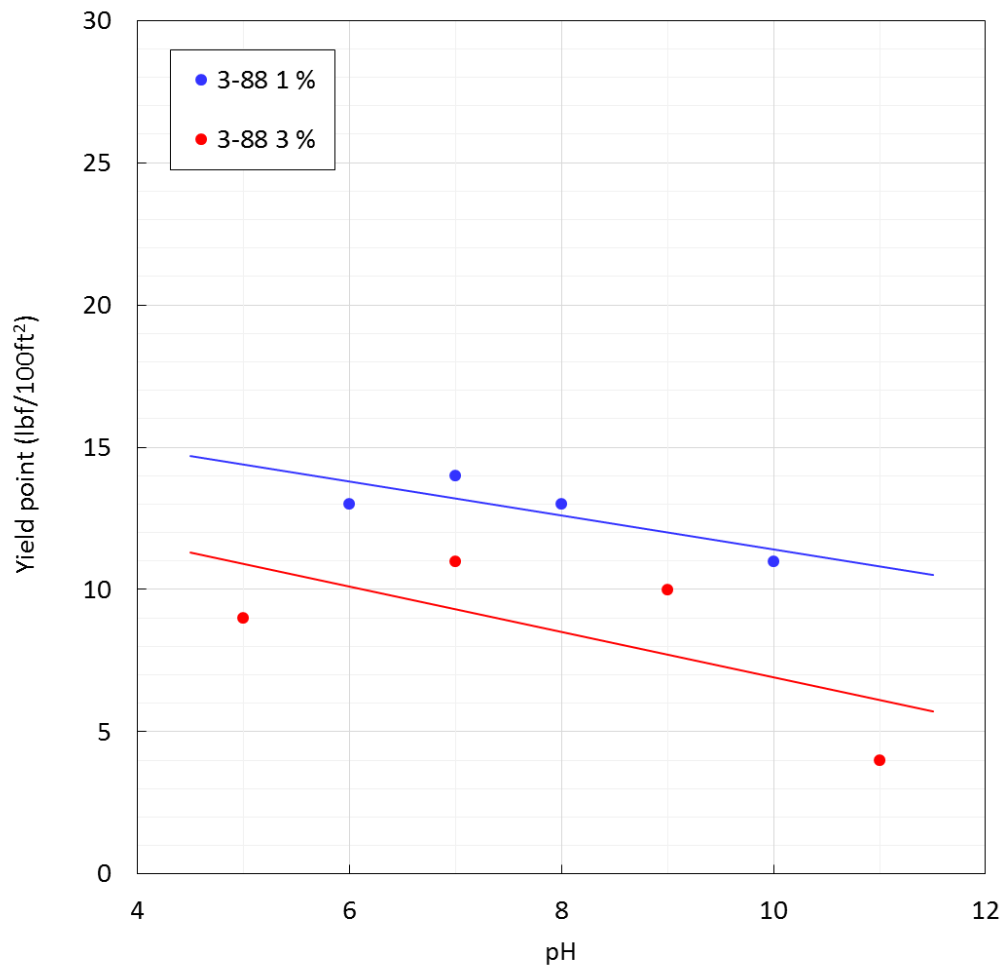
Figure 28 Variation of yield point with pH in simple PPGBAE muds with 1 wt% PVOH (blue circles) and 3 wt% PVOH (red circles)
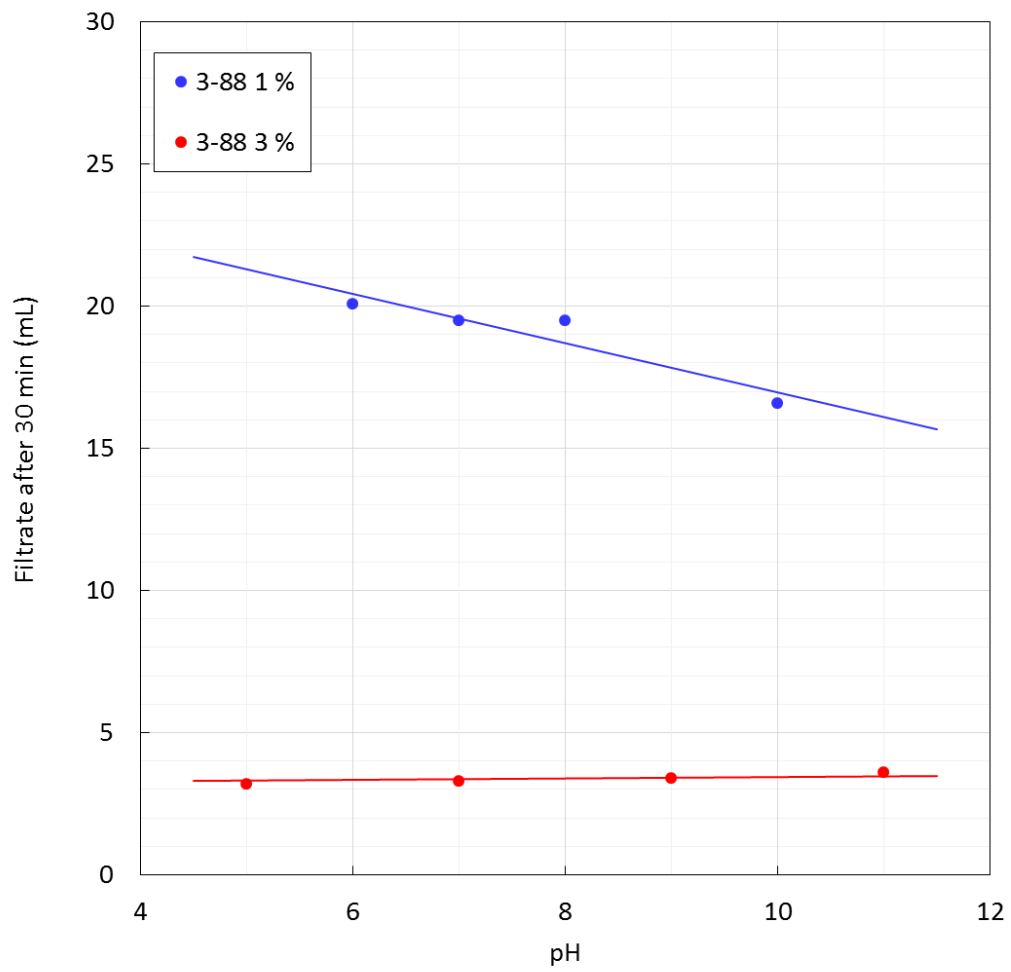
Figure 29 Fluid loss properties of simple polyamine muds at various pH

Figure 27 and Figure 28 show the variation of plastic viscosity and yield point of the simple PPGBAE muds as a function of pH. The plastic viscosity did not depend on pH and the yield point slightly decreased with pH regardless of PVOH content.

Figure 29 shows the fluid loss properties of the simple PPGBAE muds as a function of pH. With 1 wt% of PVOH, filtrate decreased with pH. With 3 wt% of PVOH, on the other hand, filtrate did not depend on pH. The less the pH, the more NH_2 groups of PPGBAE become $NH_3^+Cl^-$ groups and the more effective PPGBAE becomes. This is probably why filtrate increased as we decrease the pH when the PVOH content was low (1 wt%) and was not enough to cover all bentonite platelets. When the PVOH content was high (3 wt%), on the other hand, filtrate did not depend on pH because PVOH could completely cover all bentonite platelets. Note that this is consistent with the discussion in 1.3.6.2.

1.3.7. Compatibility with Other Additives

In this section, we checked the performance of PVOH as a deflocculant with other common additives, in other words, we checked the compatibility of PVOH with other additives in terms of rheological properties and fluid loss properties. We formulated the KCl muds and PPGBAE muds shown in Table 15.

Table 15 Mud composition to check the compatibility of PVOH with other additives commonly used

Additive	Function	Concentration
Wyoming bentonite	Viscosifier Filtration control	5 lb/bbl (1.4 wt%)
CMC	Filtration control	0.5 lb/bbl (0.14 wt%)
Starch	Filtration control	3 lb/bbl (0.86 wt%)
Lignite	HPHT filtration control	2 lb/bbl (0.57 wt%)
KCl or PPGBAE	Shale inhibitor	0 – 30 lb/bbl (0 – 8.6 wt%)
Lignosulfonate or PVOH (3-88)	Deflocculant	3 lb/bbl (0.86 wt%)
HCl or KOH	pH control	pH = 10

1.3.7.1. KCl mud
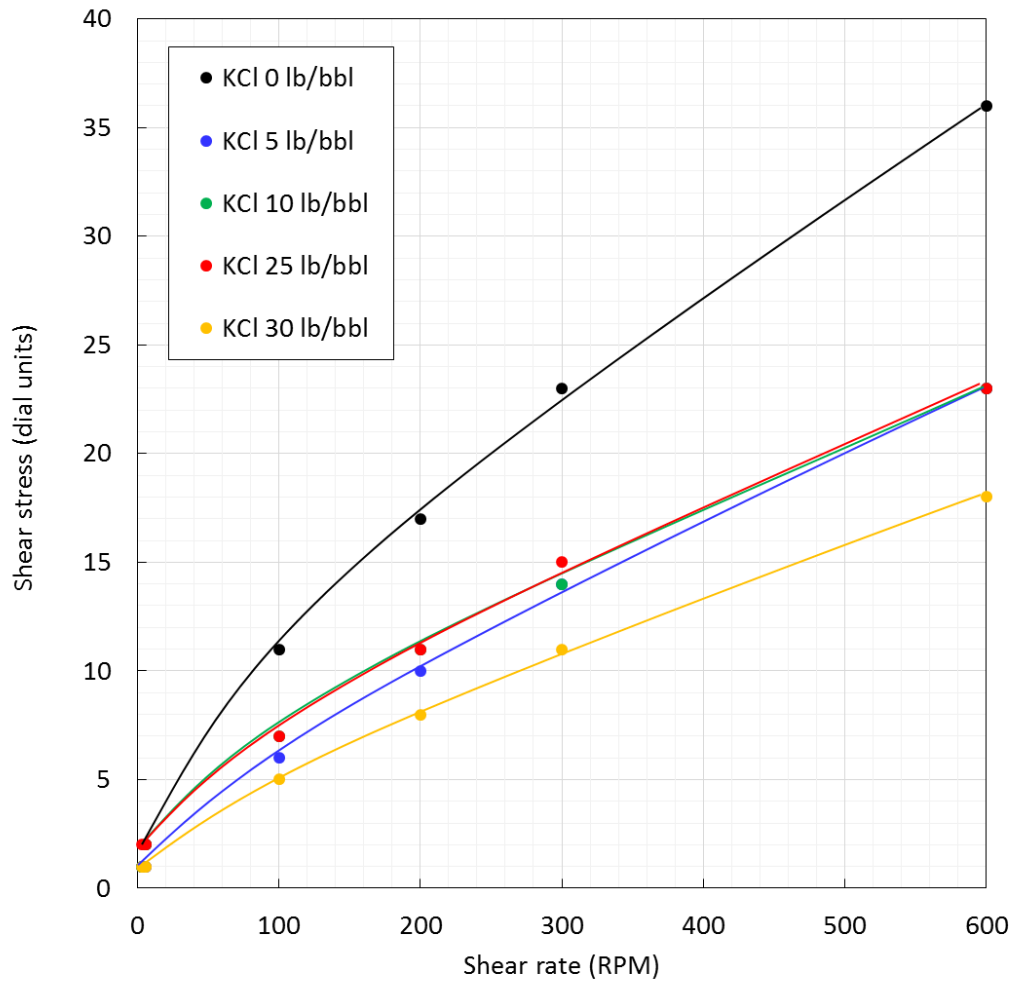
Figure 30 Variation of shear stress with shear rate in KCl muds with lignosulfonate as a defocculant
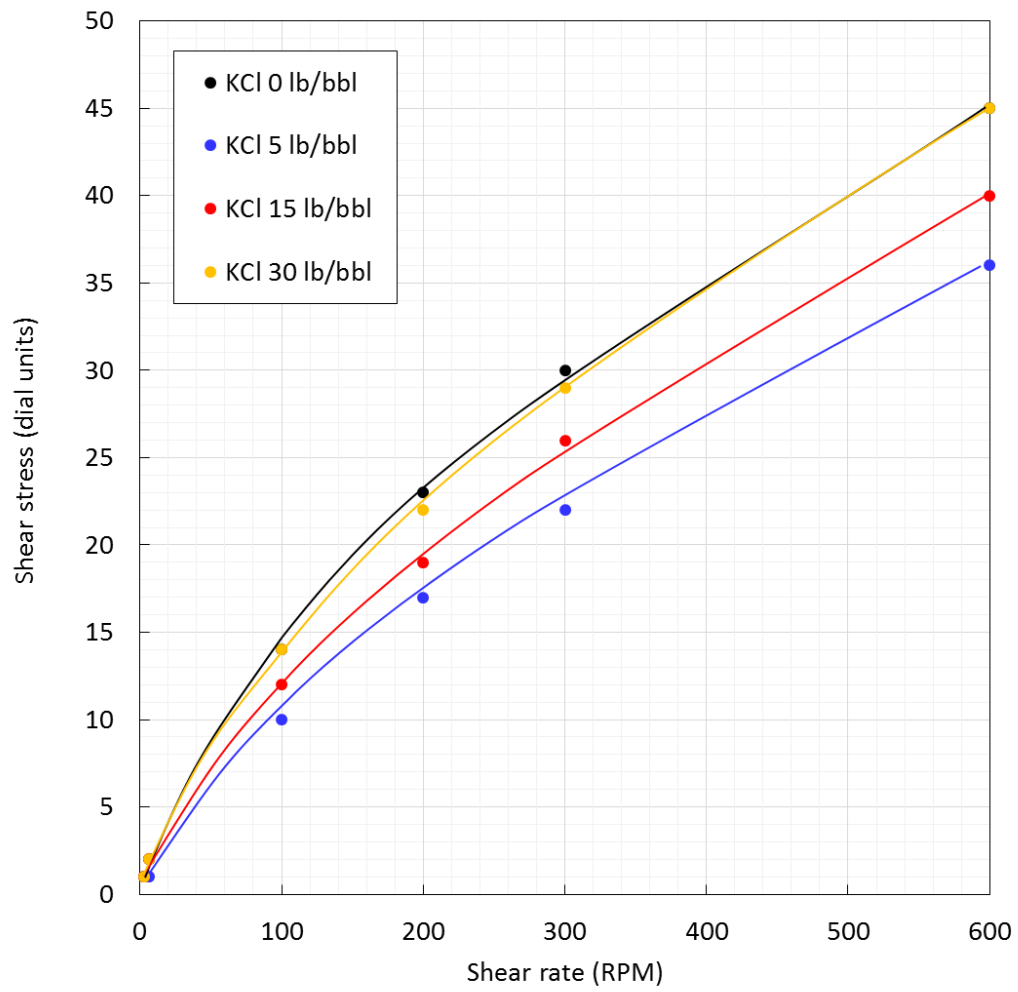
Figure 31 Variation of shear stress with shear rate in KCl muds with PVOH as a deflocculant
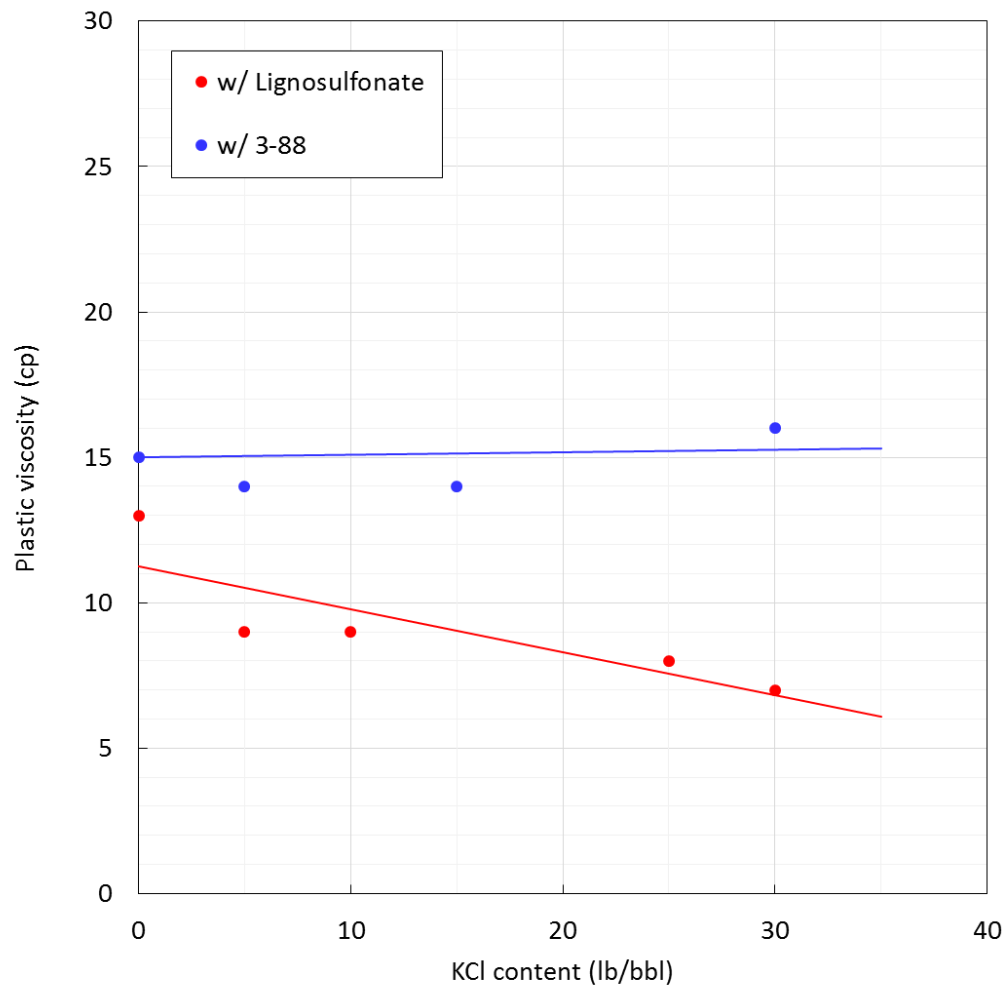
Figure 32 Variation of plastic viscosity with KCl content in KCl muds with lignosulfonate (red circles) or PVOH (blue circles) as a deflocculant
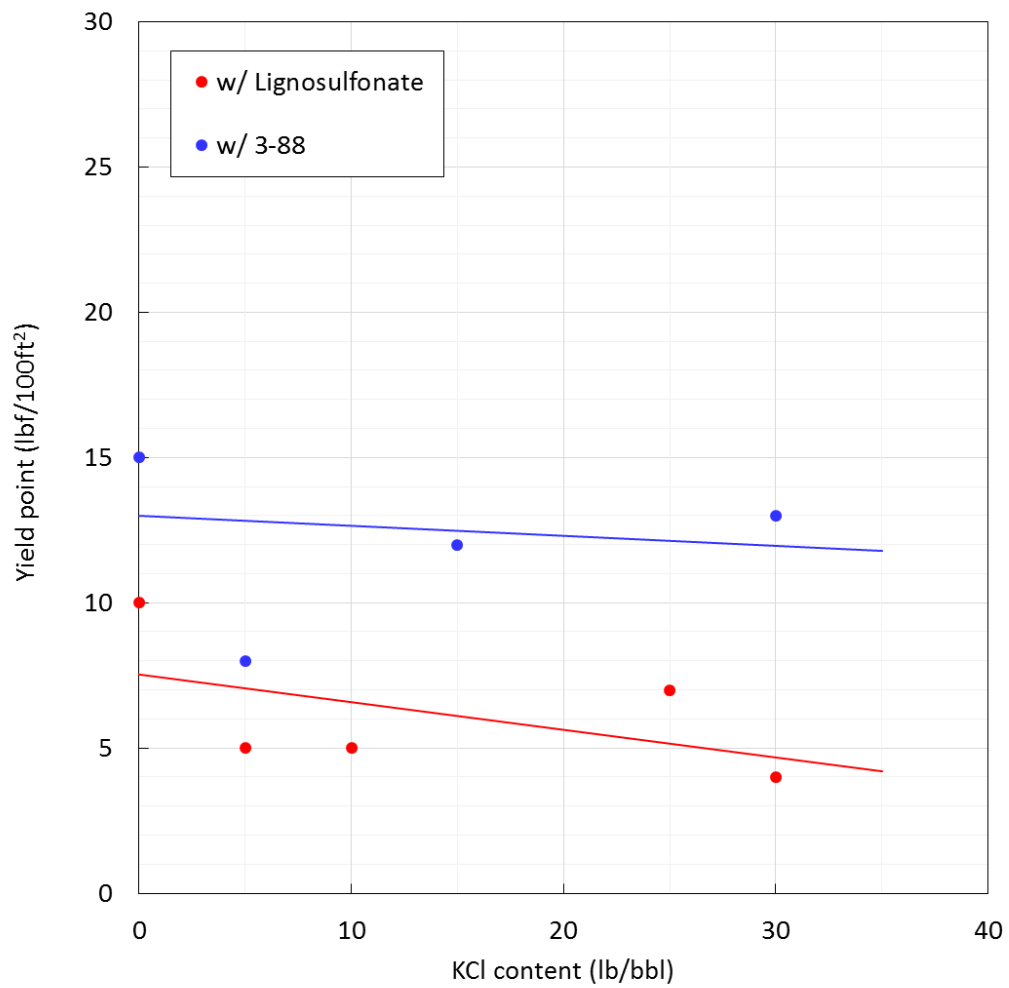
Figure 33 Variation of yield point with KCl content in KCl muds with lignosulfonate (red circles) or PVOH (blue circles) as a deflocculant
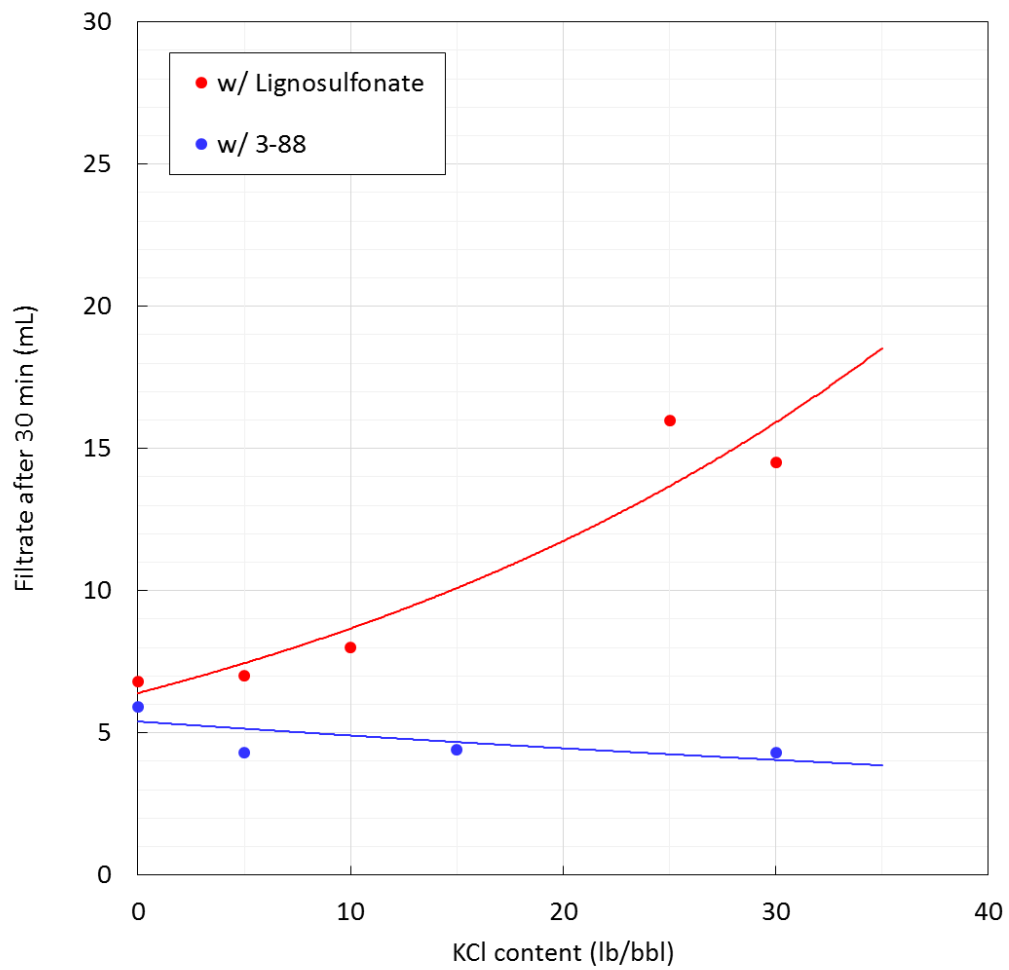
Figure 34 Variation of the volume of filtrate in KCl muds with lignosulfonate (red circles) or PVOH (blue circles) as a deflocculant

Figure 30 shows the variation of shear stress with shear rate in the KCl muds with lignosulfonate as a deflocculant. The rheological properties were normal for all the formulations and no floc was observed.

Figure 31 shows the variation of shear stress with shear rate in the KCl muds with PVOH (3-88) as a deflocculant. Same as the KCl muds with lignosulfonate as a deflocculant, the rheological properties were normal for all the formulations and no floc was observed. With PVOH as a deflocculant, however, the effect of KCl content on shear stress was smaller than the one with lignosulfonate as a deflocculant.

Figure 32 and Figure 33 show the results of plastic viscosity and yield point of the KCl muds as a function of KCl content, respectively. We can hardly say there are any correlations between KCl content and plastic viscosity or yield point because of the scattering of the data points.

Figure 34 shows the results of fluid loss properties of the KCl muds as a function of KCl content. With lignosulfonate as a deflocculant, filtrate increased with KCl content. With PVOH as a deflocculant, on the other hand, filtrate did not increase with KCl content. Thus, PVOH works as a deflocculant better than lignosulfonate even with other additives despite the fact that PVOH was not compatible with high concentration KCl as we discussed in 1.3.6.1.

1.3.7.2. PPGBAE mud
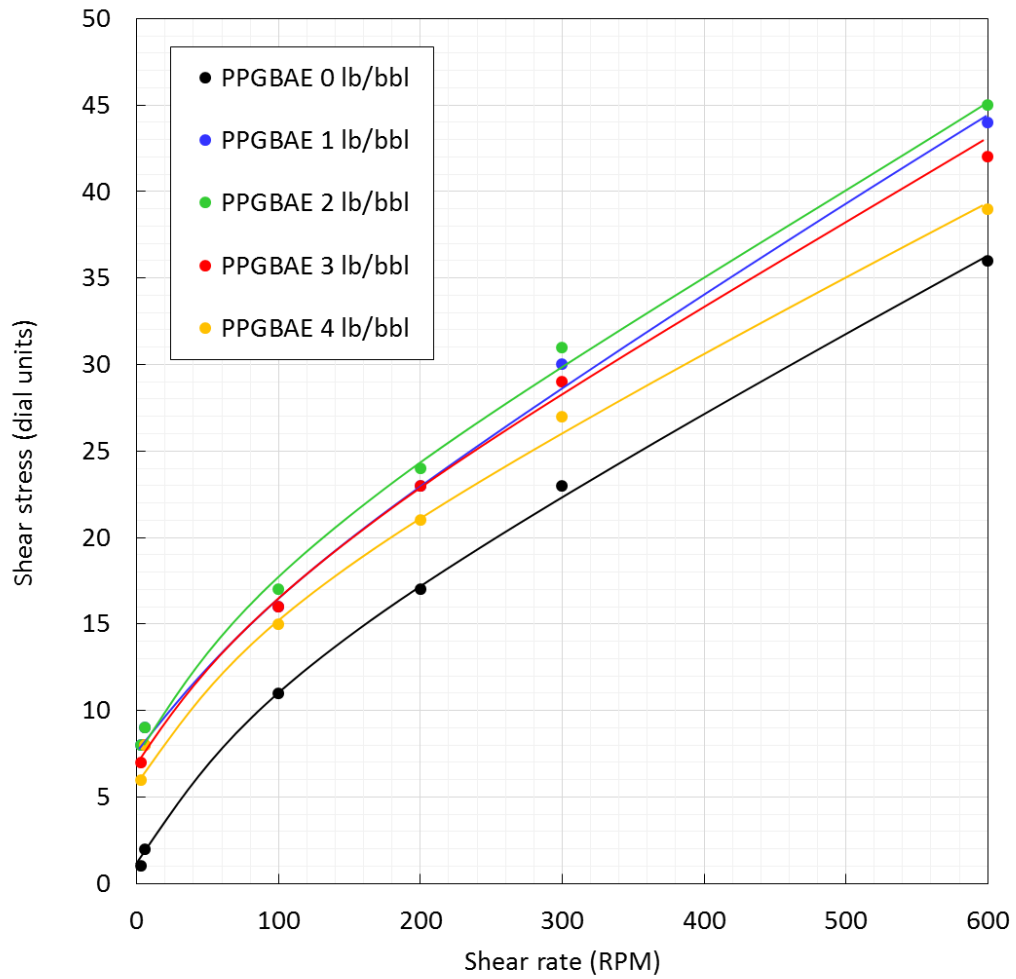
Figure 35 Variation of shear stress with shear rate in PPGBAE muds with lignosulfonate as a deflocculant
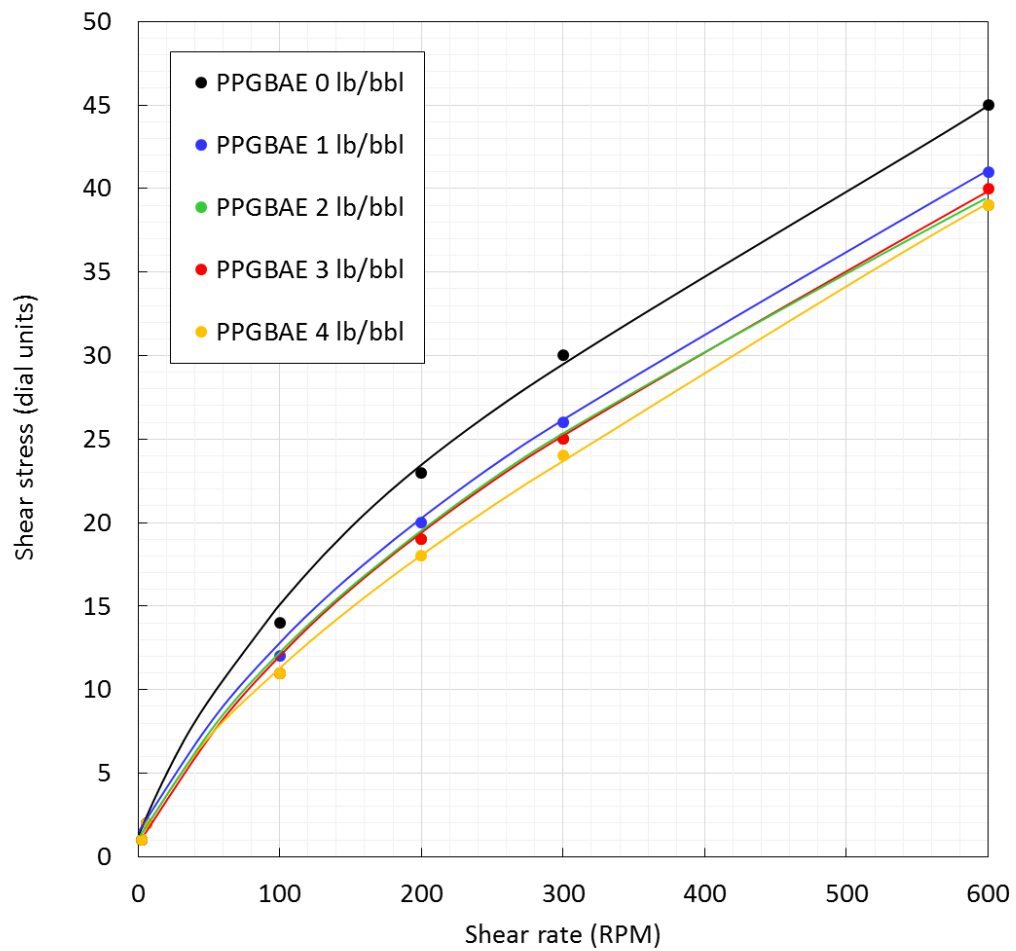
Figure 36 Variation of shear stress with shear rate in PPGBAE muds with PVOH as a deflocculant
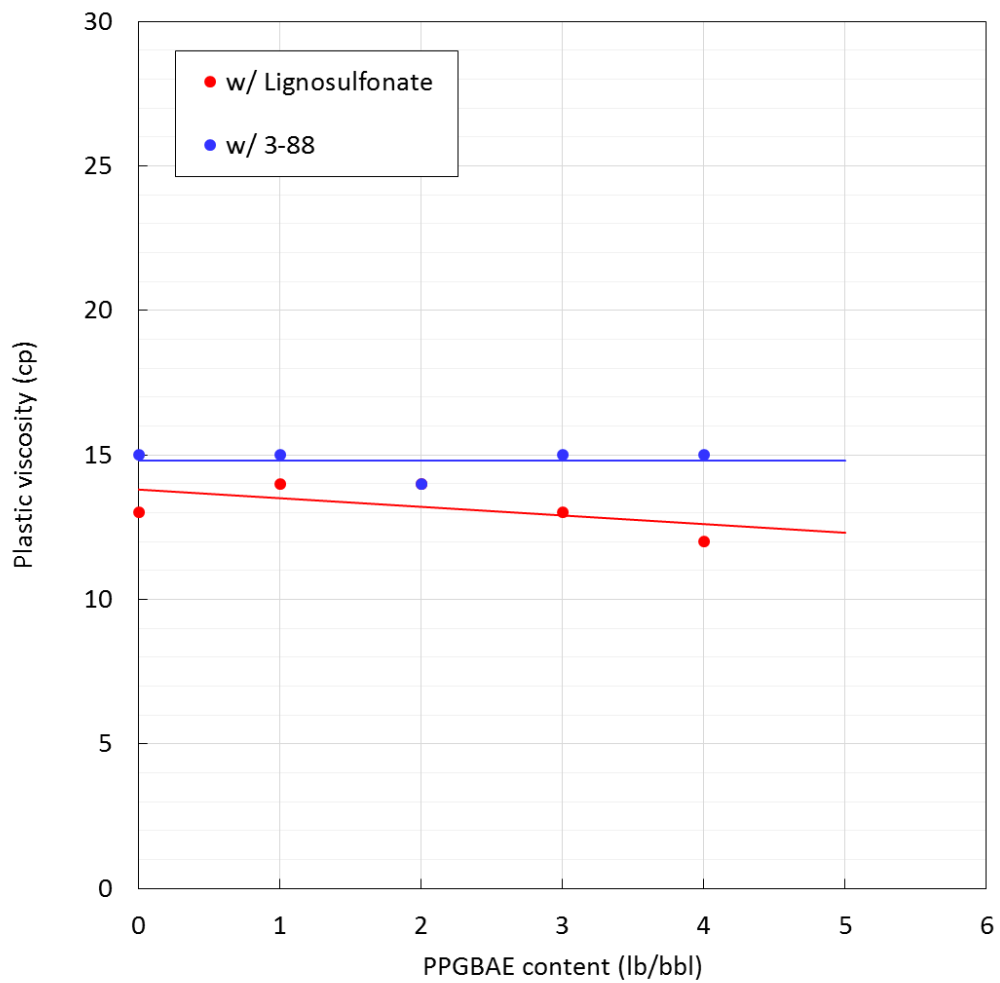
Figure 37 Variation of plastic viscosity with PPGBAE content in PPGBAE muds with lignosulfonate (red circles) or PVOH (blue circles) as a deflocculant
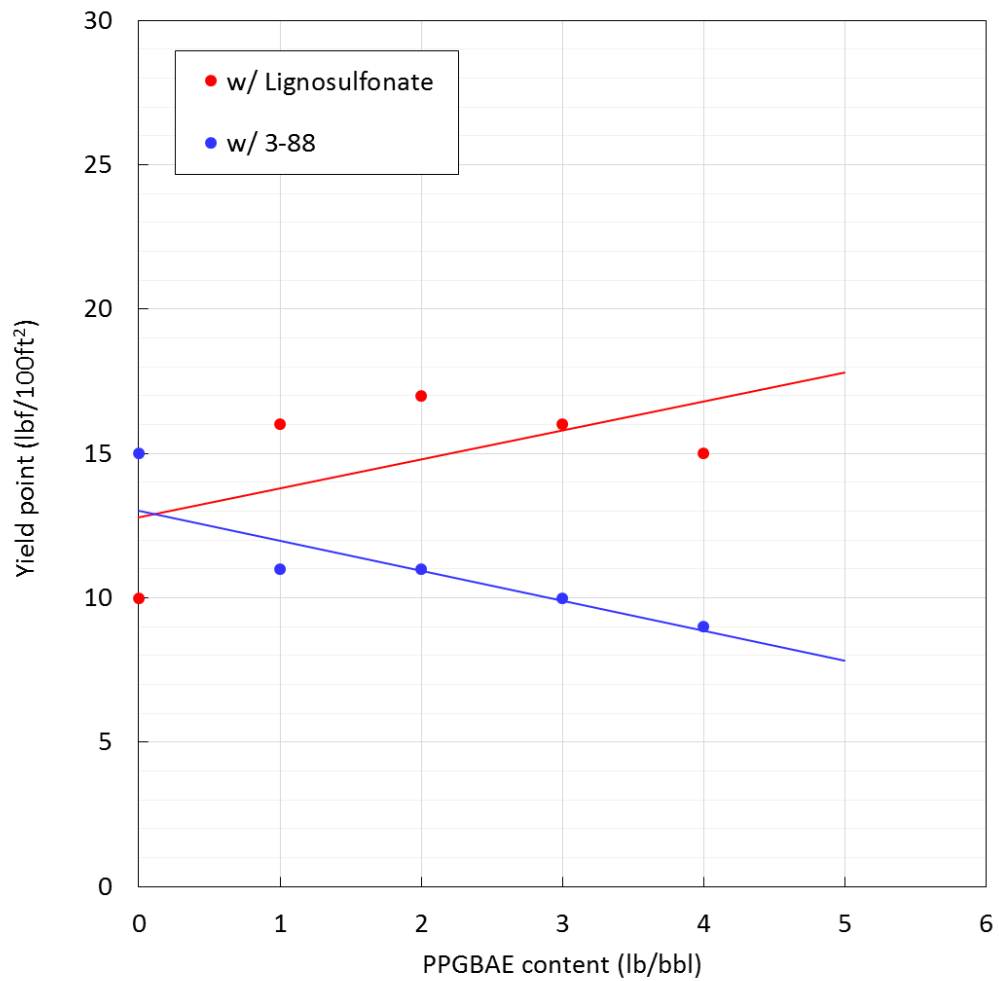
Figure 38 Variation of yield point with PPGBAE content in PPGBAE muds with lignosulfonate (red circles) or PVOH (blue circles) as a deflocculant
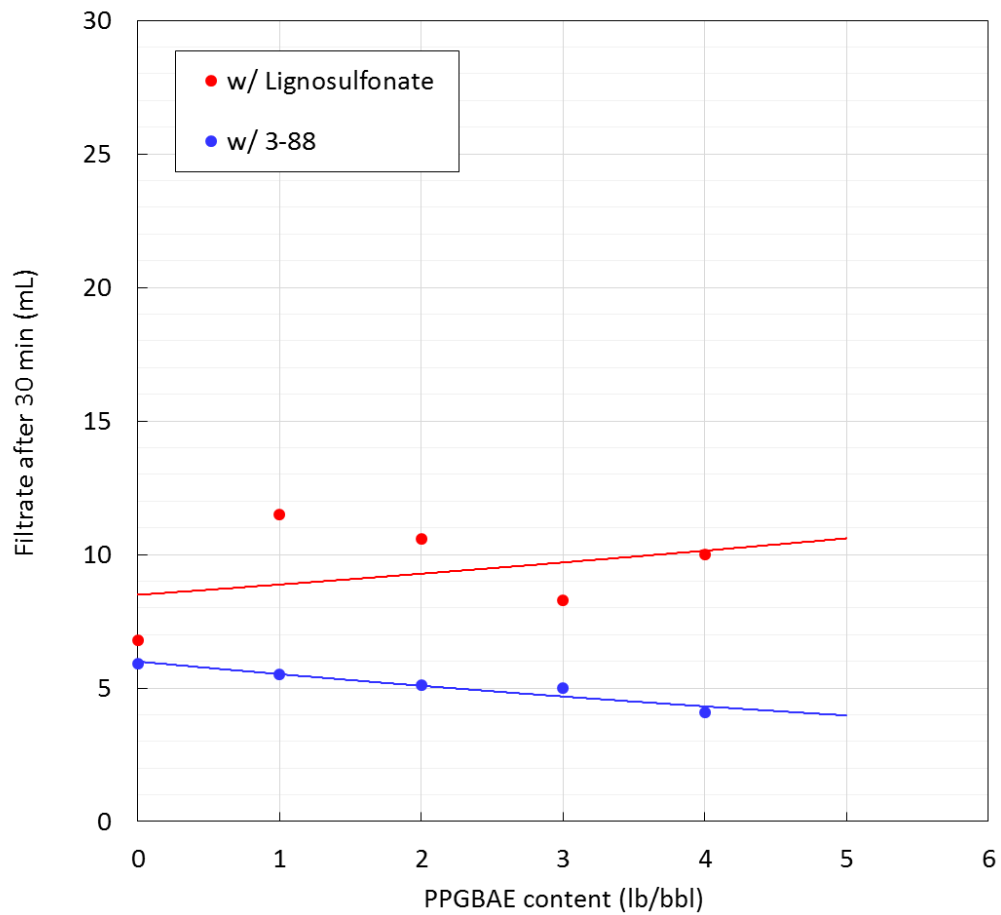
Figure 39 Variation of the volume of filtrate in PPGBAE muds with lignosulfonate (red circles) or PVOH (blue circles) as a deflocculant

Figure 35 shows the variation of shear stress with shear rate in the PPGBAE muds with lignosulfonate as a deflocculant. The rheological properties were normal for all the formulations and no floc was observed.

Figure 36 shows the variation of shear stress with shear rate in the PPGBAE muds with PVOH (3-88) as a deflocculant. Same as the PPGBAE muds with lignosulfonate as a deflocculant, the rheological properties were normal for all the formulations and no floc was observed. With PVOH as a deflocculant, similarly to the discussion in 1.3.7.1, the effect of PPGBAE content on shear stress was smaller than the one with lignosulfonate as a deflocculant.

Figure 37 and Figure 38 show the results of plastic viscosity and yield point of the PPGBAE muds as a function of PPGBAE content, respectively. We can hardly say there are any correlations between PPGBAE content and plastic viscosity or yield point because of the scattering of the data points.

Figure 39 shows the fluid loss properties of the PPGBAE muds as a function of PPGBAE content. The results are similar to those of KCl muds. With lignosulfonate as a deflocculant, filtrate increased with PPGBAE content. With PVOH as a deflocculant, on the other hand, filtrate did not increase with PPGBAE content. Similarly to the discussion in 1.3.7.1, PVOH works as a deflocculant better than lignosulfonate even with other additives. Note that this is consistent with the discussion in 1.3.6.2.

1.3.8. High Temperature Tolerance

In this section, we check the high temperature tolerance of PVOH compared to lignosulfonate. We formulated the same mud as we used in the previous section with PPGBAE as a shale inhibitor and lignosulfonate or PVOH as a deflocculant (Table 16). We measured the rheological properties and the fluid loss properties of the muds before and after hot-rolling at 16 rpm at 250 °F for 16 hours.

Table 16 Mud composition to check high temperature tolerance of PVOH compared to lignosulfonate

Additive	Function	Concentration
Wyoming bentonite	Viscosifier Filtration control	5 lb/bbl (1.4 wt%)
CMC	Filtration control	0.5 lb/bbl (0.14 wt%)
Starch	Filtration control	3 lb/bbl (0.86 wt%)
Lignite	HPHT filtration control	2 lb/bbl (0.57 wt%)
Polyamine	Shale inhibitor	4 lb/bbl (1.14 wt%)
Lignosulfonate or PVOH	Deflocculant	3 lb/bbl (0.86 wt%)
HCl	pH control	pH = 10
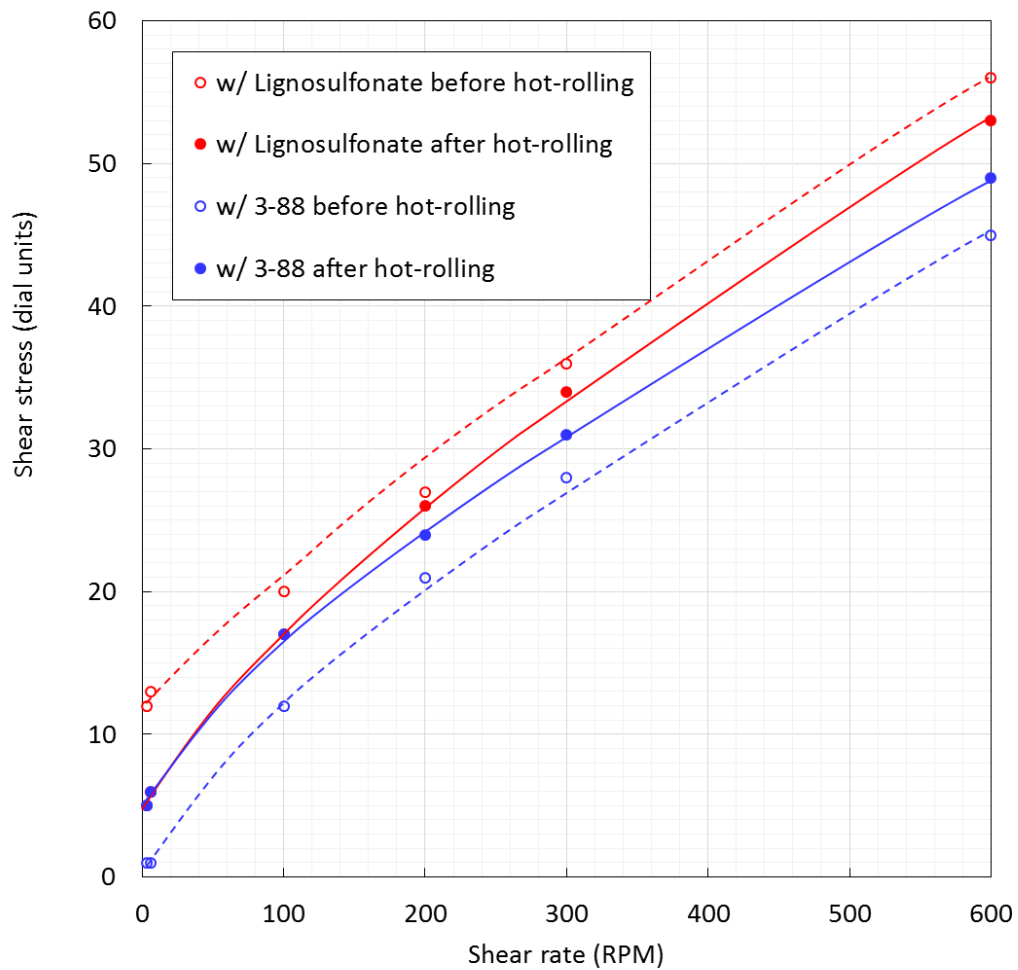
Figure 40 Variation of shear stress with shear rate in PPGBAE muds before (open circles) and after (filled circles) hot-rolling. Red symbols represent lignosulfonate as a deflocculant and blue symbols represent PVOH as a deflocculant
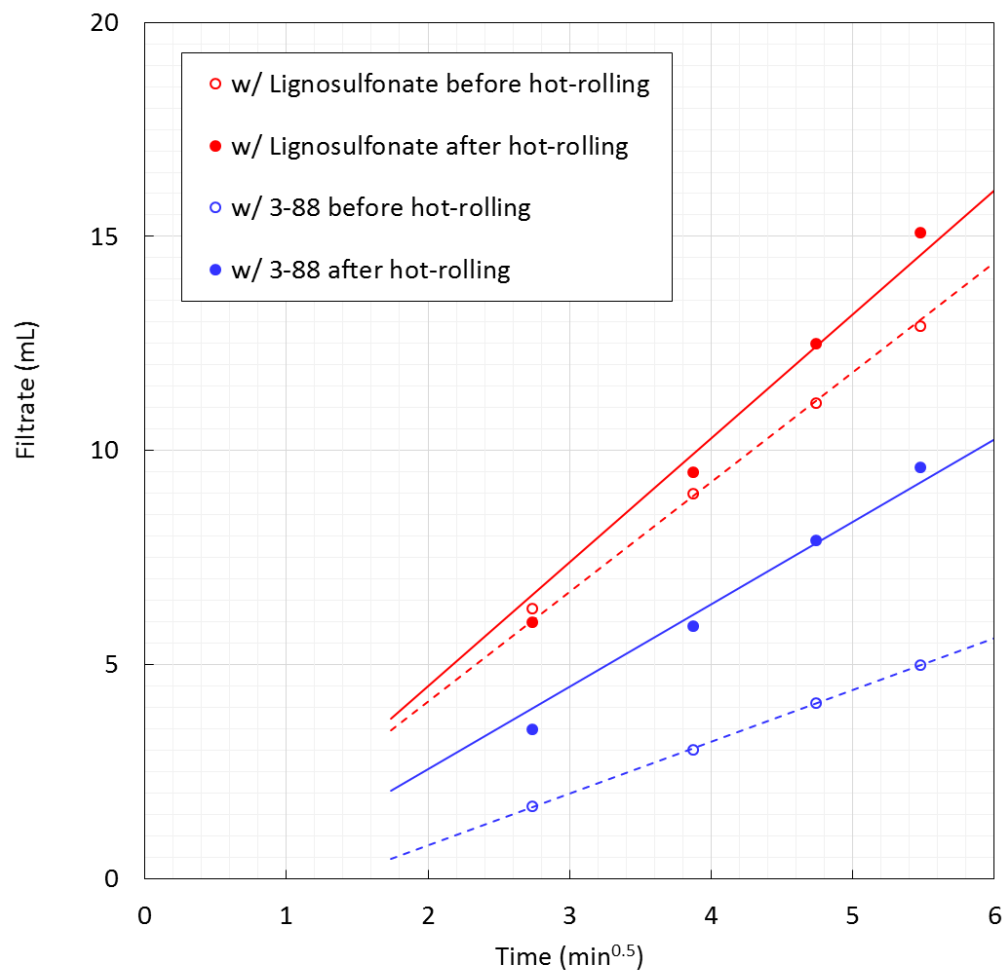
Figure 41 Fluid loss properties of PPGBAE muds before (open circles) and after (filled circles) hot-rolling. Red symbols represent lignosulfonate as a deflocculant and blue symbols represent PVOH as a deflocculant

As shown in Figure 40, the rheological properties did not change much before and after the hot-rolling regardless of whether lignosulfonate (filled and open red circles) or PVOH (filled and open blue circles) was used as a deflocculant.

As shown in Figure 41, the volume of filtrate from the mud with PVOH as a deflocculant increased by hot-rolling, whereas the one with lignosulfonate did not change much. This means PVOH is more sensitive to high temperature than lignosulfonate probably because of thermal decomposition of the PVOH. Even after hot-rolling, however, the volume of filtrate from the mud with PVOH was still less than the one with lignosulfonate before hot-rolling. In other words, the performance of PVOH after being exposed to high temperature is still better than the performance of fresh lignosulfonate.

1.3.9. Swelling

In this section, we perform swelling tests using Wyoming bentonite and Marcellus shale pellets compacted under 10,000 psi for 1.5 hours in order to optimize the mud composition to achieve low shale swelling.

The composition of tested muds is shown in Table 17. Note that all muds contained Wyoming bentonite (5 lb/bbl), CMC (0.5 lb/bbl), Starch (3 lb/bbl), and Lignite (2 lb/bbl) in common except for sample 1 that was prepared for control experiment (Wyoming bentonite 5 lb/bbl only).

Table 17 Mud composition for swelling test

Sample	Concentration (lb/bbl)				pH
	KCl	PPGBAE	Lignosulfonate	PVOH (3-88)	
0	-	-	-	-	8
1	30	-	3	-	10
2	30	-	-	3	10
3	-	4	3	-	10
4	-	4	-	3	10
5	-	0	-	3	10
6	-	1	-	3	10
7	-	2	-	3	10
8	-	3	-	3	10
9	-	2	-	3	8
10	-	2	-	3	6
11	-	2	-	1	8

1.3.9.1. Bentonite Pellet
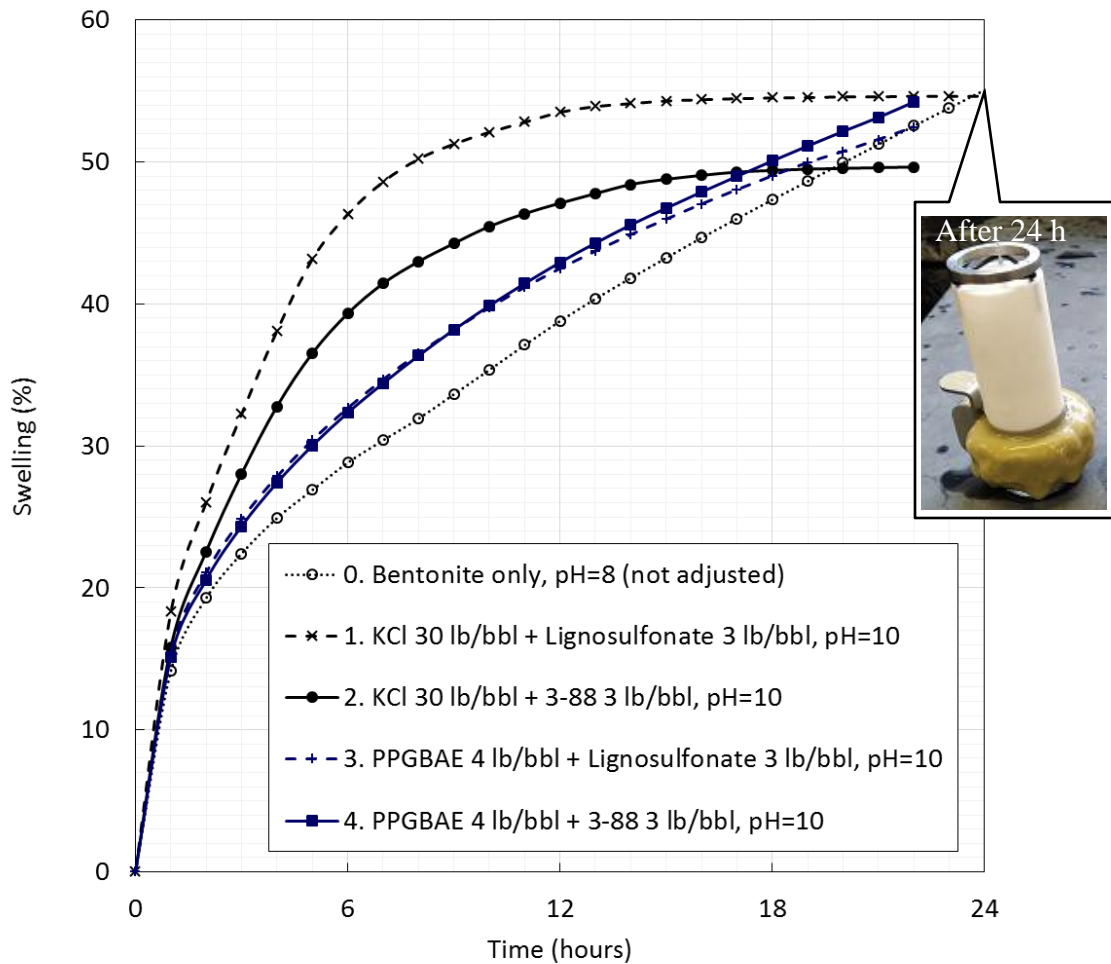
Figure 42 Linear swelling rate for Wyoming bentonite pellet in KCl muds and PPGBAE muds. Dashed curves represent lignosulfonate as a deflocculant and solid curves represent PVOH as a deflocculant. Dotted curve represents control experiment. The photo is the appearance of the pellet tested in sample 0 for 24 hours
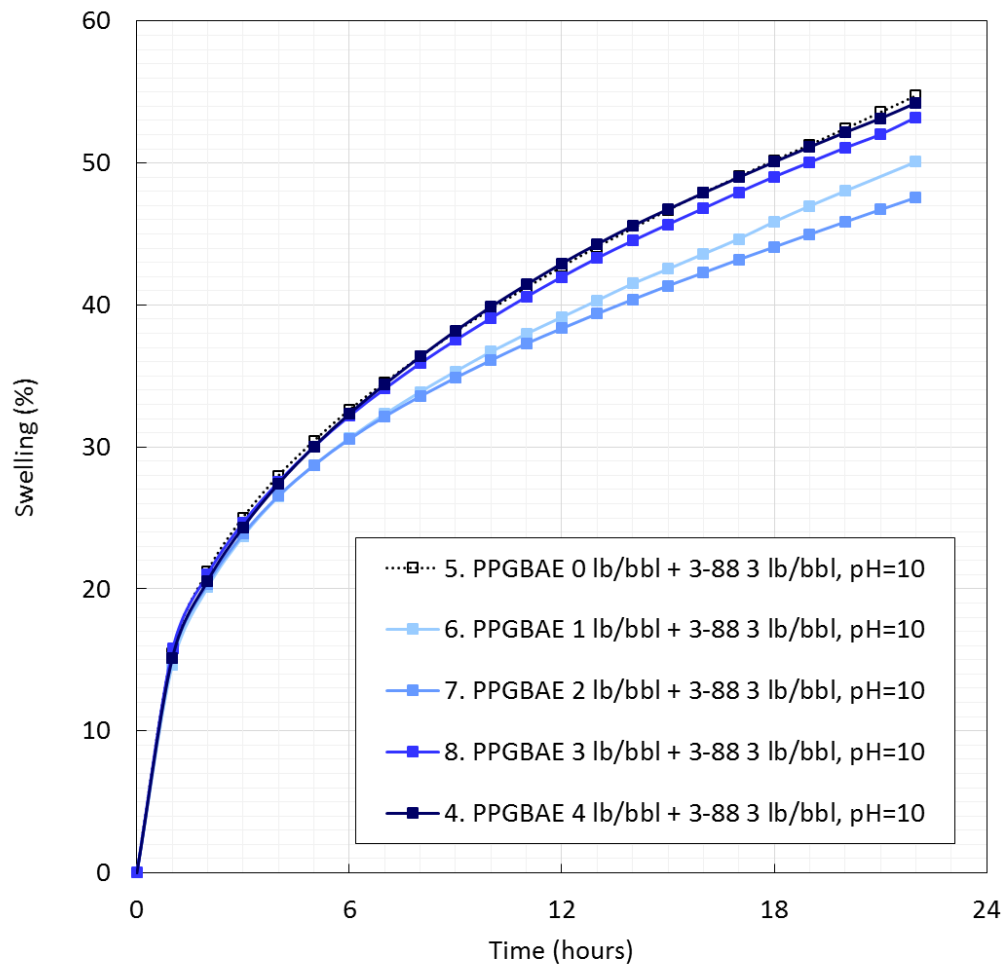
Figure 43 Linear swelling rate for Wyoming bentonite pellet in PPGBAE muds with different PPGBAE content
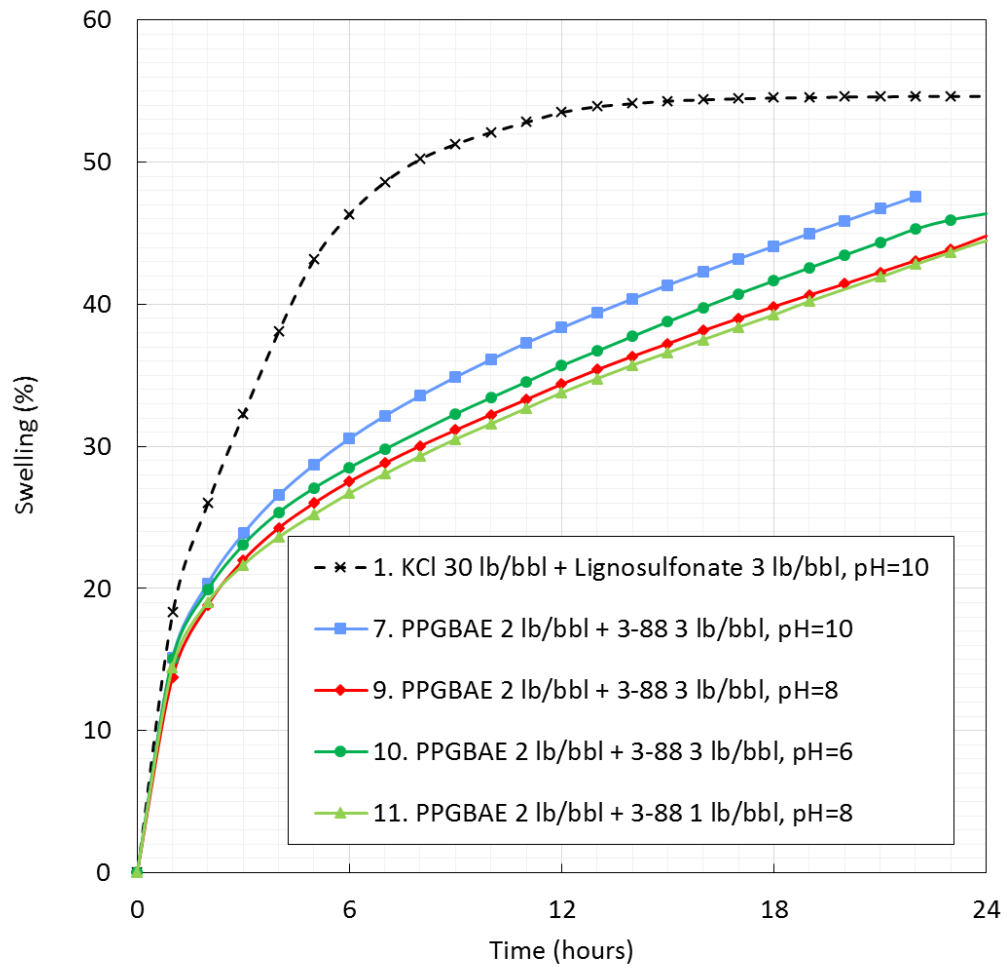
Figure 44 Linear swelling rate for Wyoming bentonite pellet in KCl and PPGBAE muds with different pH and PVOH content

As shown in Figure 42, KCl muds (sample 1 and 2) caused more rapid swelling than corresponding PPGBAE muds (sample 3 and 4) and for KCl muds swelling was inhibited more effectively by using PVOH instead of lignosulfonate. However, the equilibrated swelling values caused by KCl muds were lower than that caused by PPGBAE muds probably because the mud compositions of sample 3 and 4 were not suitable for PPGBAE. Note that swelling caused by sample 0 (control experiment) could not be properly measured because the swelling was so large that the pellet was squeezed out from the confining screen (photo in the figure) although the swelling seemed smaller than PPGBAE muds.

In order to achieve low swelling with PPGBAE as a shale inhibitor, first, we checked the effect of PPGBAE content (Figure 43). Surprisingly, large amount of PPGBAE did not necessarily result in lower swelling and swelling reached minimum when PPGBAE content was 2 lb/bbl (sample 7).

Next, we checked the effect of pH (sample 7, 9, and 10). As shown in Figure 44, swelling reached minimum when pH was 8 (sample 9). Lastly, we checked the effect of PVOH content (sample 9 and 11). As seen in the figure, PVOH content made little difference to swelling.

As a result, we discovered that PPGBAE considerably slowed down the swelling rate if the mud composition was properly optimized, even though the equilibrated swelling might be close to the swelling caused by typical KCl mud (sample 1).

1.3.9.2. Marcellus Shale Pellet

Based on the results discussed in the previous section, we chose sample 0, 1, 9, and 10 and applied them to Marcellus shale pellet samples. The results are shown in Figure 45.
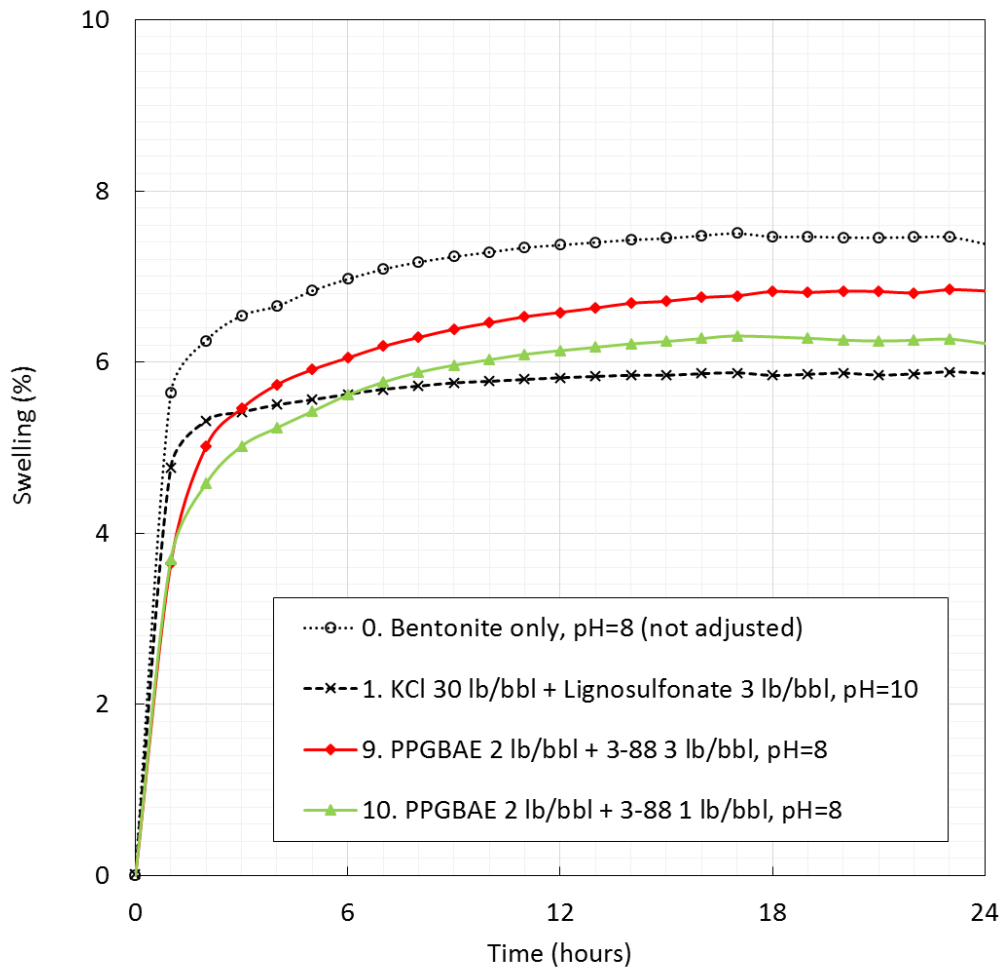
Figure 45 Linear swelling rate for Marcellus pellet in bentonite mud (dotted curve, control experiment), typical KCl mud (dashed black curve) and PPGBAE muds (red and green solid curves). Dashed curve represents lignosulfonate as a deflocculant and solid curves represent PVOH as a deflocculant

As shown in Figure 45, similarly to the results for the bentonite pellet discussed in the previous section, KCl mud (sample) caused more rapid swelling than PPGBAE muds (sample 9 and 10). In this case, PVOH content affected the swelling. Lower PVOH content led to lower swelling (sample 10) and the swelling was close to the one caused by typical KCl mud (sample 1). Note that no flocculation was observed even with 1 lb/bbl PVOH content. Swelling would be reduced even more if further optimization were performed.

1.4. Concluding Remarks

- PVOH works as a deflocculant better than lignosulfonate

- DP should be low so it does not significantly affect the mud rheology

- DH = 88 % works the best as a deflocculant

- PVOH 3-88 (DP = 300, DH = 88 %) would be the best choice

- PVOH content should be determined according to bentonite content, not PPGBAE content. Practically, we would recommend to use the same amount of PVOH as bentonite

- PVOH works better with PPGBAE than with KCl due to its incompatibility with high concentration KCl

- pH of the mud does not affect the fluid loss properties as long as there is enough PVOH in the system

- PVOH is compatible with most additives commonly used

72

- Hot-rolling lowers the performance of PVOH but it is still better than that of lignosulfonate before hot-rolling

- PPGBAE and PVOH content significantly affects the swelling and needs to be optimized to achieve low shale swelling

2. ESTIMATION OF DOWNHOLE SWELLING

2.1. Introduction

2.1.1. Literature Review

A reliable assessment of shale swelling potential is a key parameter in the selection and design of drilling and completion fluids. One of the best methods for assessing swelling potential is to expose a sample of the shale in question to the fluids being considered, and to directly measure the swelling. Since preserved shale core is rarely available, swelling tests usually must be performed by creating shale "pellets" from cuttings. Ground-up cuttings are compressed into a sample, and this sample acts as a substitute for the unavailable shale core. The created shale pellet contains the same clay mineralogy as the target shale, and in theory its swelling should be similar to that of the intact preserved shale. However, there are many factors that can cause the swelling of the pellet to be unrepresentative, and different than that of the actual shale. Swelling tests can be greatly affected by capillary pressure effects, which arise when the sample is not fully saturated. The release of capillary suction pressure upon exposure to the test fluid can result in swelling that is completely unrelated to chemical or osmotic clay swelling, and such swelling would not occur under downhole conditions. These artifacts can plague tests on both intact samples and created pellets, but it is more difficult to ensure saturation of a created pellet. A pellet is also very different physically from the true intact shale. Because it has been created by grinding up the shale and recompacting it, the internal fabric and the pore structure are likely to be very different. Ewy and

Morton proposed a new methodology for pellet creation which ensured full saturation to avoid the capillary pressure effect. Even with full saturation and high humidity equilibration, however, the pellets would swell more than the native intact shales (Ewy and Morton 2009). Even though the swelling results are still valuable for fluid design, they do not represent the actual downhole swelling and thereby we are not able to predict if wellbore instabilities will occur.

Shale swelling has been commonly measured using linear swell meter (LSM). Besides using pellets as shale samples, it is also an issue that the LSM measurements are performed under atmospheric pressure and temperature, whereas actual downhole swelling obviously occurs under in situ conditions. Some studies have been done on the measurement of swelling under high pressure, however, they all require specially designed equipment (Ewy and Stankovich 2010, Chenevert and Osisanya 1992, Zhou et al. 1992, Ewy and Morton 2008).

2.1.2. Objective

In this study, we propose a method to estimate downhole swelling using pellet samples and the conventional LSM. We review the literature (Ewy and Morton 2009) and measure the swelling of pellets and their intact counterparts to check the capillary pressure effect caused by the pellet creation method. We also measure swelling of both pellet and intact core samples under various axial loads of the LSM in order to be able to estimate the downhole swelling by extrapolating the axial loads to the downhole stress conditions. Then, we analytically check the consistency of the swelling measured under

atmospheric pressure and the one estimated by extrapolation with the actual field observations. Finally, we propose an improved procedure that analytically predicts the wellbore stability from the estimated downhole swelling even when the preserved intact core is not available.

2.2. Experimental Methods

2.2.1. Rock Samples

2.2.1.1. Downhole Core Samples

The downhole cores listed in Table 18 were obtained from Nankai trough during Integrated Ocean Drilling Program expeditions of D/V Chikyu and provided by Dr. Hiroko Kitajima of Department of Geology and Geophysics at Texas A&M University. Table 18 also shows the basic properties of the samples and more detailed information is available at http://sio7.jamstec.go.jp/.

Table 18 List of downhole core samples

Sample	Depth (ft) Below seafloor	Rock type	Porosity (%)	Bulk density (g/cc)
319-C0009A 9R-1-WR	5198	Silty claystone	36.4	2.1376
338-C0022B 00014X-03-WR	365	Silty claystone	49.6	1.8689

2.2.1.2. Outcrop Shale Samples

The Marcellus shale outcrop sample was provided by Dr. A Daniel Hill of

Harold Vance Department of Petroleum Engineering. The Mancos outcrop shale sample

was purchased from Kocurek Industries Inc.. Table 19 is the list of outcrop shale

samples.

Table 19 List of outcrop shale samples

Sample	Collection location	Bulk density (g/cc)
Marcellus	Pennsylvania	2.3800
Mancos	Salt Lake City, Utah	2.5492

2.2.2. Sample Preparation

2.2.2.1. Pellet Creation

Ewy and Morton (2009) pointed out swelling could be affected by capillary

pressure effects and proposed a new pellet creation method to avoid these effects. Table

20 compares the conventional method to Ewy and Morton's method.

Table 20 Comparison of two pellet creation methods

	Conventional method	Ewy and Morton (2009)
Rock sample	Ground to pass through 200-mesh sieve	Ground to pass through 200-mesh sieve
Amount of water	5 wt% of room-dry ground shale	Determined by empirical correlation
Consolidation	Compacted at 10,000 psi for 1.5 hours	Pressure is determined by empirical correlation, compacted for 1.5 hours
Conditioning	Stored in 30 %RH chamber for 24 hours	Stored in 98 %RH chamber for 2 weeks

In the conventional method, amount of water in the sample is 5 wt % and consolidation or compaction pressure is 10,000 psi regardless of rock types. In the Ewy and Morton's method, on the other hand, these are determined by an empirical correlation they found to ensure full saturation. And in the conventional method, pellets are stored in 30 % relative humidity chamber at least for 24 hours, whereas in Ewy and Morton's method, pellets are stored in 98 % chamber for 2 weeks before the swelling test.

Ewy and Morton's method utilizes two parameters. One is the mass of 20 g room-dry ground rock after drying at 165 °F (M_d, g) and the other is the rock in-situ bulk density (ρ_b, g/cc). The amount of water to be added to the ground rock (W_a) and consolidation pressure (P) are obtained by

$$W_a = WC_p \times M_d - (20 - M_d)$$

$$P = 7000 + \frac{3000(\rho_b - 2.19)}{2.52 - 2.19},$$

where

$$WC_p = WC_e + WC_n$$

$$WC_e = 0.1229e^{-13.274WC_n}$$

$$WC_n = 0.75284 - 0.0094\rho_b(10 + M_d).$$

We created the pellet samples from each rock sample listed in Table 18 and

Table 2 using the values of W_a and P summarized in Table 21.

Table 21 Ewy and Morton's parameters for pellet creation

Sample	M_d (g)	ρ_b (g/cc)	W_a (g)	P (psi)
Nankai 319	19.08	2.1376	2.4045	6524
Nankai 338	19.54	1.8689	4.2216	4081
Marcellus	19.79	2.3800	2.2685	8727
Mancos	19.82	2.5492	2.0431	10265

2.2.2.2. Intact Core Samples

All downhole core samples from Nankai trough were hand-carved into discs of 1

1/8 inch in nominal diameter and 1/2 inch in nominal thickness with a razor blade. All

outcrop samples were cut into discs of 1 1/8 inch in nominal diameter and 1/2 inch in

nominal thickness at Kocurek Industries Inc.. All intact core samples were stored in 98 %RH chamber for 2 weeks before the swelling test.

2.2.3. Swelling

As described in 1.2.6, a Fann Linear Swell Meter (LSM) Model 2000 was used to measure the swelling of the created pellets and the intact cores. In this study, we propose a method to estimate downhole swelling. The basic idea is to simulate the downhole situation by adding a weight on the swelling indicator of the LSM and extrapolating the stress condition to the downhole stress condition. In order to do that, first we need to know the stress condition of the sample in the LSM.

Figure 46 LSM measurement with additional weight

Figure 46 shows the LSM measurement with an additional weight on the swelling indicators. We fabricated two weights that weigh 1,452 g and 4,573 g, respectively.
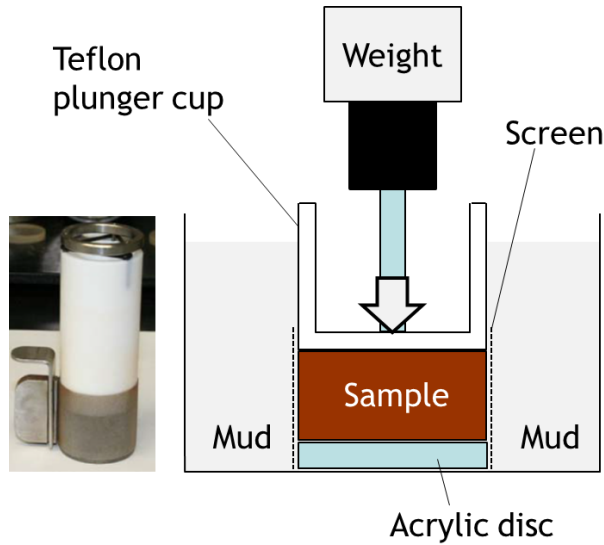
Figure 47 LSM sample setup with additional weight

Figure 47 shows the sample setup of the LSM with an additional weight. As described in 1.2.6, the sample is placed between a clear acrylic disc and a Teflon plunger cap. The sample and end pieces are then wrapped with a screen that fits tightly around the sample. This screen contains the sample and prevents slaking or dispersion when it is exposed to the test fluid. It also largely prevents lateral swelling, such that nearly all the

Figure 48 LSM sample setup w/o screen

swelling occurs vertically, or parallel to the sample axis. However, it is somewhat tricky to discuss the stress condition of the test sample because the confining force from the screen is unknown. Wrapping the sample with the screen is essential to measure the swelling of pellets otherwise the samples would swell laterally and the area to which the axial load from the swelling indicator is applied would become significantly smaller than the top surface area of the sample. To measure the swelling of intact samples, on the other hand, it is not necessary to wrap the sample with the screen because swellings of intact samples are usually so small that the change in the top surface area of the sample will be negligible. The sample setup without the screen is shown in Figure 48. Without the screen, we can determine the stress condition of the sample as shown in Table 22. Hereafter, swelling measurement of intact core samples was performed without the screen unless otherwise noted.

Table 22 Stress condition of samples in LSM

| Weight (g) | Axial stress* (psi) | Radial stress | | Average stress w/o screen** (psi) |
		w/ screen (psi)	w/o screen (psi)	
None	-1.2	Unknown	0	-0.4
1,452	-4.4	Unknown	0	-1.7
4,573	-11.3	Unknown	0	-3.8

*Weight of the swelling indicator (550 g) was added to each weight to calculate the axial stresses. Note that the top surface area of the sample is 1 in^2 and compression was taken to be negative.
**Average stress is calculated by 1/3(Axial stress + 2Radial stress)

2.2.4. Triaxial Test

Triaxial compression tests were performed to determine the Young's modulus of the Nankai trough 319-C0009A 9R-1-WR sample. Confining pressure was chosen to be 2610 psi based on the consolidation pressure, 6524 psi, calculated by Ewy and Morton's empirical correlation assuming Poisson's ratio to be 0.4 to avoid overcosolidation or undesired failure of the sample. The sample assembly is shown in Figure 49. We fabricated 2 steel frustum-of-a-cone spacers shown in green to accommodate the difference between the diameter of upper/lower pistons of the apparatus and the sample. Then, the sample was set between the spacers, wrapped with heat-shrinkable tube, and loaded and tested with four loading-unloading cycles. This experiment was performed on the Large Sample Rig in John W. Handin Laboratory for Experimental Rock Deformation of the Department of Geology & Geophysics.

Figure 49 Sample assembly

2.3. Results and Discussion

2.3.1. Effect of Pellet Creation Method

In order to confirm the effect of pellet creation method, we measured the swelling of two pellets made from Nankai trough 319-C0009A 9R-1-WR. One was created by the conventional method and the other one was created by Ewy and Morton's

method. We also measured the swelling of the intact core sample for comparison. For simplicity, we used a simple 3 wt% bentonite mud without any additives. Note that the intact core was also wrapped with the screen in this case. The results are shown in Figure 50.
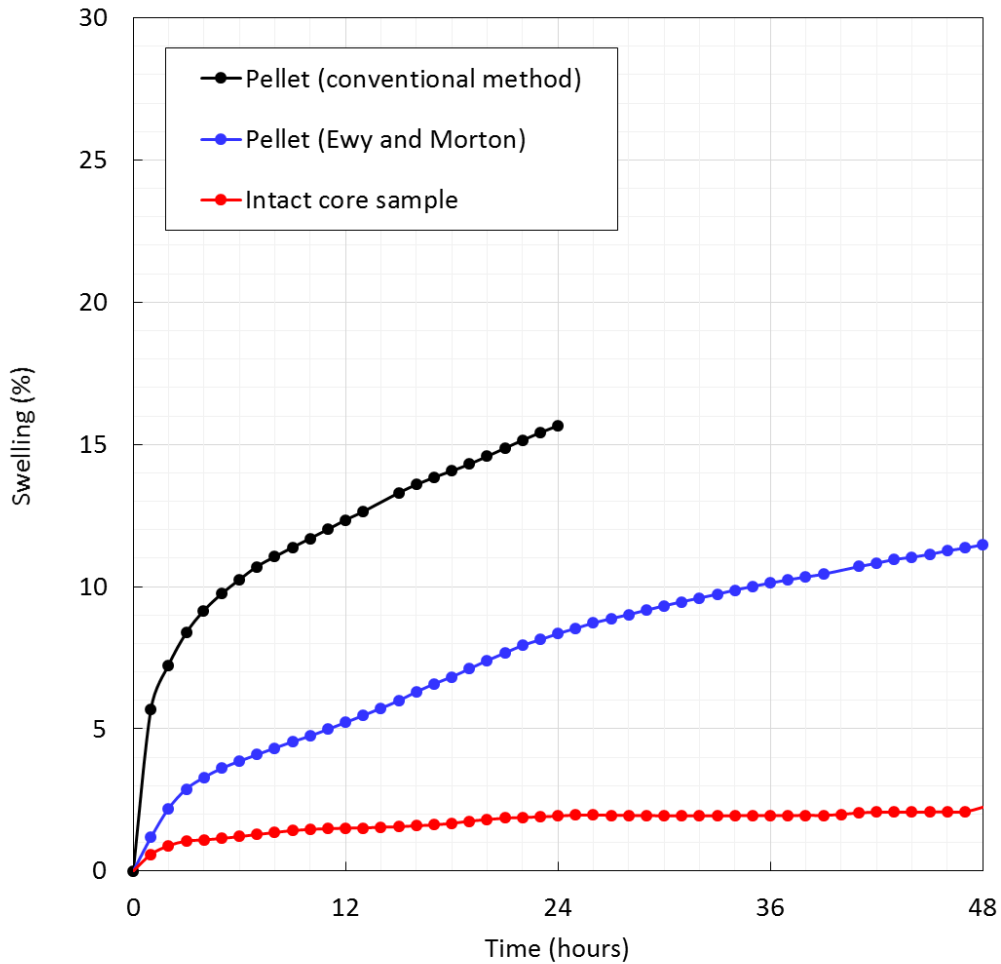
Figure 50 Linear swelling rate for Nankai trough 319-C0009A 9R-1-WR samples in 3 wt% bentonite mud. Black circles: pellet made by conventional method, Blue circles: pellet made by Ewy and Morton's method, Red circles: intact core sample

As shown in Figure 50, the swelling was significantly reduced by means of Ewy and Morton's method. However, there was still a big discrepancy between the pellet created by Ewy and Morton's method and the intact core maybe because the fabric of a pellet was quite different from that of an intact core.

2.3.2. Difference between Pellet and Intact

Based on the fact that we still found a big discrepancy between the pellet swelling and the intact core swelling even though the pellet was made by means of Ewy and Morton's method, in this section, we focus on the difference between pellet and intact core.

Figure 51 is the swelling data from Ewy and Morton 2009. They measured swelling of the pellets and the intact core samples made from "high Kaolinite shale C" in 4 types of brine.
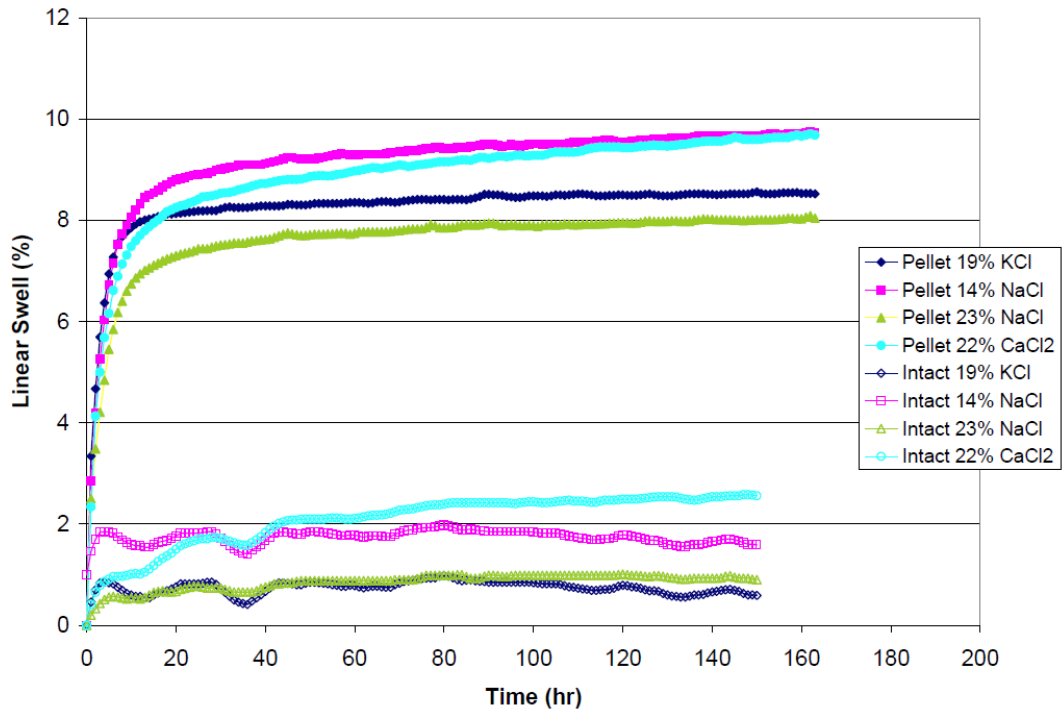
Figure 51 Linear swelling rate for Shale C pellets and intact samples, in four different brines (Reprinted from Ewy and Morton 2009)

As we discussed in the previous section, they also found a big discrepancy between the pellets and the intact core samples even though they made the pellets by means of their new method.

We also measured the swelling of a pellet made by means of Ewy and Morton's method and an intact core sample for Nankai trough 319-C0009A 9R-1-WR in the PPGBAE mud shown in Table 16. The results are shown in Figure 52. Note that the intact core sample was also wrapped with the screen in this case.
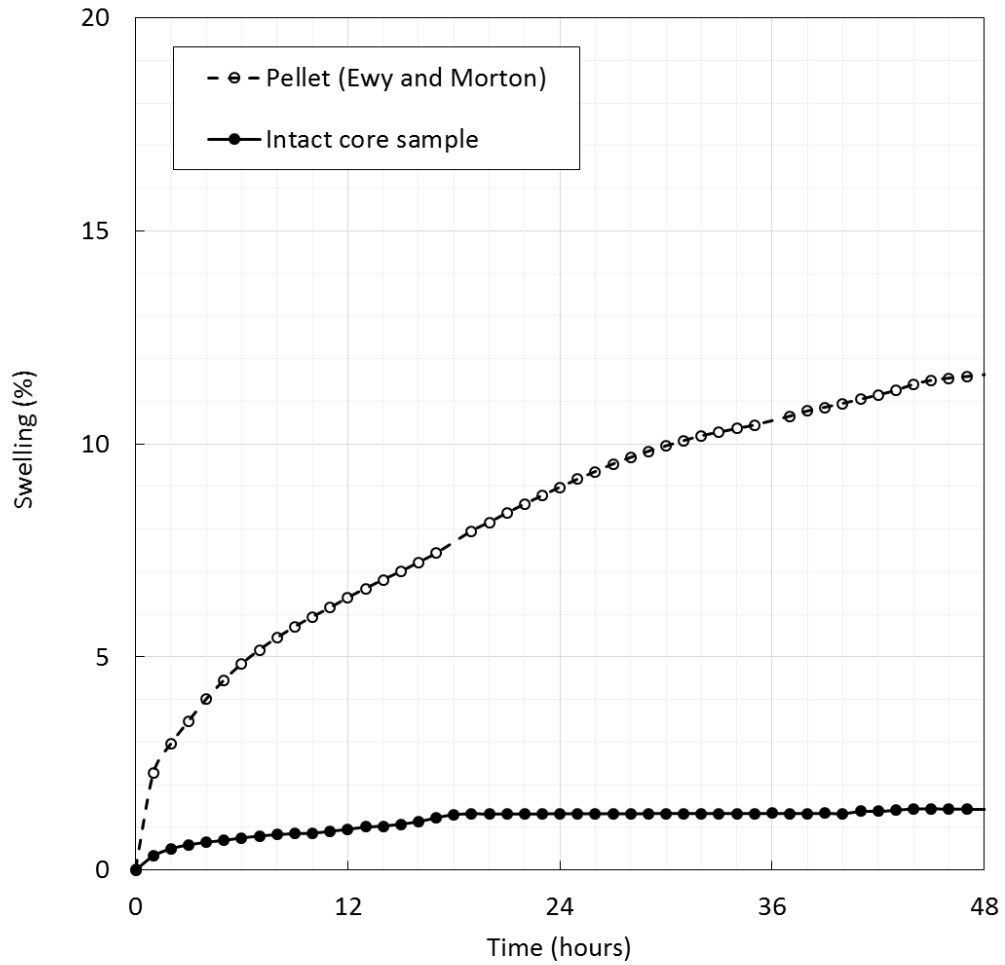
Figure 52 Linear swelling rate for Nankai trough 319-C0009A 9R-1-WR samples in PPGBAE mud to compare the swelling between pellet made by Ewy and Morton's method (open circles) and intact core (filled circles)

As is the case with Figure 50 and Figure 51 measured in different fluids, as shown in Figure 52, a big discrepancy between the results of the swelling of the pellet and the intact core sample was observed. As can be seen in Figure 50, Figure 51, and Figure 52, swelling approximately reached equilibrium within 48 hours. Thus, we regard the swelling of the intact core sample in PPGBAE mud shown in Figure 52 after 48 hours as 1.42 %. Next, we check if the measured swelling is consistent with the actual wellbore stability observations in the following section.

2.3.3. Consistency of Measured Swelling with Wellbore Stability Observations

In this section, we check if the results of the swelling of the intact core sample (Nankai trough 319-C0009A 9R-1-WR) is consistent with in situ wellbore stability observations. First, we need to figure out the downhole stress condition. Table 23 shows the key parameters at the depths of breakout occurrence in Hole C0002A (Huffman et al. 2016). Note that the stresses are referenced to zero at seafloor and these data were not obtained from this particular well, C0009A, but its neighboring well, C0002A, which was 20 miles away from C0009A. We use this because it is more complete data set than that for the C0009A.

Table 23 Key parameters at the depths of breakout occurrence in Hole C0002A (Adapted from Huffman et al. 2016)

Depth	σ_{H1}	σ_{H2}	σ_v	P_p	UCS	Breakout angle
(ft)	(psi/ft)	(psi/ft)	(psi/ft)	(psi/ft)	(psi)	(degrees)
2953	0.835	0.638	0.805	0.447	1856	32
3117	0.800	0.642	0.805	0.447	1769	6
3281	0.822	0.654	0.804	0.446	1348.5	7
3773	0.772	0.676	0.803	0.442	928	110
4265	0.809	0.694	0.813	0.445	1479	78
4547	0.756	0.702	0.810	0.443	812	100

And the pressure gradients were plotted in Figure 53 as a function of depth below sea floor, where

σ_{H1} : horizontal stress (psi/ft)

σ_{H2} : horizontal stress (psi/ft)

σ_v : vertical stress (psi/ft)

P_p : pore pressure
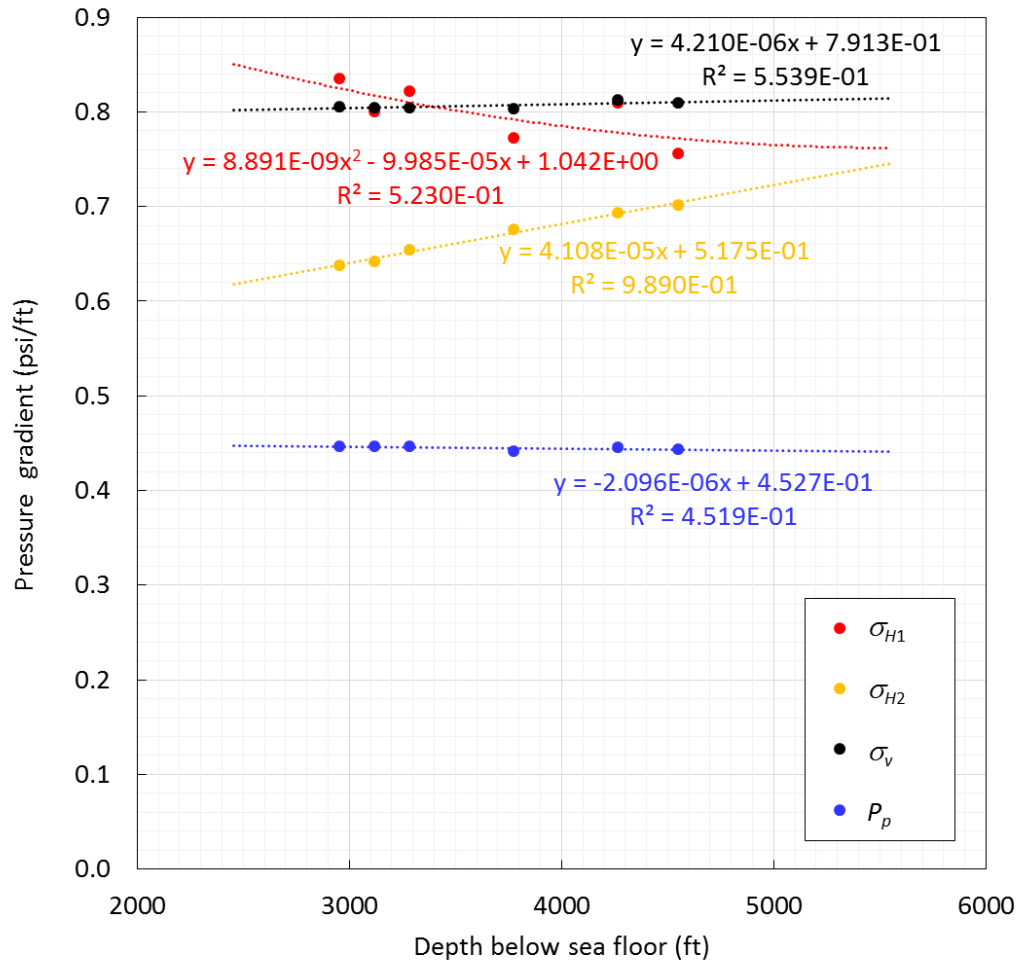
Figure 53 Pressure gradients in the hole 314-C0002A. Also shown in Table 23

By extrapolating the four pressure gradients by using the interpolation formulae shown in Figure 53, the stress gradients at 5198 ft, from which the core sample was obtained, are obtained as below.

$$\sigma_{H1} = 0.763 \text{ psi/ft}$$

$$\sigma_{H2} = 0.731 \text{ psi/ft}$$

$$\sigma_v = 0.813 \text{ psi/ft}$$

$$P_p = 0.442 \text{ psi/ft}$$

And we assumed the overbalance to be 500 psi. Then, in situ stresses will be given by

$$\sigma_H = -3800 \text{ psi}$$

$$\sigma_h = -3967 \text{ psi}$$

$$\sigma_v = -4227 \text{ psi}$$

$$P_p = 2297 \text{ psi,}$$

where σ_H and σ_h are maximum and minimum horizontal stress, respectively. Note that compression was taken to be negative. By adding the pore pressure to each stress, the net stresses are obtained as below.

$$\sigma_H^{\text{net}} = -1504 \text{ psi}$$

$$\sigma_h^{\text{net}} = -1671 \text{ psi}$$

$$\sigma_v^{\text{net}} = -1931 \text{ psi}$$

$$P_w = 500 \text{ psi}$$

where P_w is the wellbore pressure. Hereafter, σ_H, σ_h, σ_v mean the net stresses unless otherwise stated.

91

To predict the wellbore stability, we need to know in situ effective stresses. Assuming that the well is vertical, the in situ effective stresses at a distance of r from the wellbore surface in cylindrical coordinate, σ_r^{eff}, $\sigma_\theta^{\text{eff}}$, σ_z^{eff}, $\tau_{r\theta}$, $\tau_{\theta z}$, τ_{rz}, can be written by

$$\sigma_r^{\text{eff}} = \frac{1}{2}(\sigma_H + \sigma_h) - \left(\frac{1}{2}\sigma_H + \frac{1}{2}\sigma_h + P_w\right)\left(\frac{r_w}{r}\right)^2$$

$$-\frac{1-2v}{1-v}\frac{1}{r^2}\int_{r_w}^{r} r\left\{\alpha\Delta p + \frac{E}{1-2v}(\eta\Delta T + \Delta S)\right\} dr \qquad (2)$$

$$+\frac{1}{2}\left\{1 + 3\left(\frac{r_w}{r}\right)^4 - 4\left(\frac{r_w}{r}\right)^2\right\}(\sigma_H - \sigma_h)\cos 2\theta + \Delta p$$

$$\sigma_\theta^{\text{eff}} = \frac{1}{2}(\sigma_H + \sigma_h) + \left(\frac{1}{2}\sigma_H + \frac{1}{2}\sigma_h + P_w\right)\left(\frac{r_w}{r}\right)^2$$

$$+\frac{1-2v}{1-v}\int_{r_w}^{r} r\left\{\alpha\Delta p + \frac{E}{1-2v}(\eta\Delta T + \Delta S)\right\} dr$$

$$-\frac{1-2v}{1-v}\left\{\alpha\Delta p + \frac{E}{1-2v}(\eta\Delta T + \Delta S)\right\} \qquad (3)$$

$$-\frac{1}{2}\left\{1 + 3\left(\frac{r_w}{r}\right)^4\right\}(\sigma_H - \sigma_h)\cos 2\theta + \Delta p$$

$$\sigma_z^{\text{eff}} = \sigma_v - \frac{1-2v}{1-v}\left\{\alpha\Delta p + \frac{E}{1-2v}(\eta\Delta T + \Delta S)\right\}$$

$$-2v\left(\frac{r_w}{r}\right)^2(\sigma_H - \sigma_h)\cos 2\theta + \Delta p \qquad (4)$$

$$\tau_{r\theta} = \tau_{\theta z} = \tau_{rz} = 0, \qquad (5)$$

where

$$\Delta p = \begin{cases} \Delta p_w \left\{ 1 - \dfrac{\ln(r/r_w)}{\ln(r_p/r_w)} \right\}, & r_w \leq r < r_p \\ 0, & r_p \leq r \end{cases} \qquad (6)$$

$$\Delta T = \begin{cases} \Delta T_w \left\{ 1 - \dfrac{\ln(r/r_w)}{\ln(r_T/r_w)} \right\}, & r_w \leq r < r_T \\ 0, & r_T \leq r \end{cases} \qquad (7)$$

$$\Delta S = \begin{cases} \Delta S_w \left\{ 1 - \dfrac{\ln(r/r_w)}{\ln(r_S/r_w)} \right\}, & r_w \leq r < r_S \\ 0, & r_S \leq r \end{cases} \qquad (8)$$

and Δp_w, ΔT_w, and ΔS_w are drawdown, temperature change, and swelling at the wellbore surface, respectively.

Assuming that drawdown, Δp, and temperature change, ΔT, are zero, the in situ effective stresses at the wellbore surface will be written by

$$\sigma_r^{\mathrm{eff}} = -P_w = -500 \text{ psi} \qquad (9)$$

$$\sigma_\theta^{\mathrm{eff}} = \sigma_H + \sigma_h - 2(\sigma_H - \sigma_h) \cos 2\theta + P_w - \frac{E}{1-\nu} \Delta S_w$$

$$= -3175 - 334 \cos 2\theta + 500 - \frac{E}{1-\nu} \Delta S_w \qquad (10)$$

$$\sigma_z^{\mathrm{eff}} = \sigma_v - 2\nu(\sigma_H - \sigma_h) \cos 2\theta - \frac{E}{1-\nu} \Delta S_w$$

$$= -1931 - 334\nu \cos 2\theta - \frac{E}{1-\nu} \Delta S_w \qquad (11)$$

$$\tau_{r\theta} = \tau_{\theta z} = \tau_{rz} = 0 \qquad\qquad (12)$$

Hence, the radial effective stress, σ_r^{eff}, and the tangential effective stress, $\sigma_\theta^{\text{eff}}$,

are maximum and minimum principal stress, respectively. Note that θ is the angle from

the minimum horizontal stress.

To predict the wellbore instability, we use Mohr-Coulomb theory. Wellbore

instability or breakout initiates at the wellbore surface when Mohr-Coulomb failure

criteria is satisfied. The critical tangential stress, $\sigma_\theta^{\text{eff,critical}}$ can be obtained as described

in Figure 54.
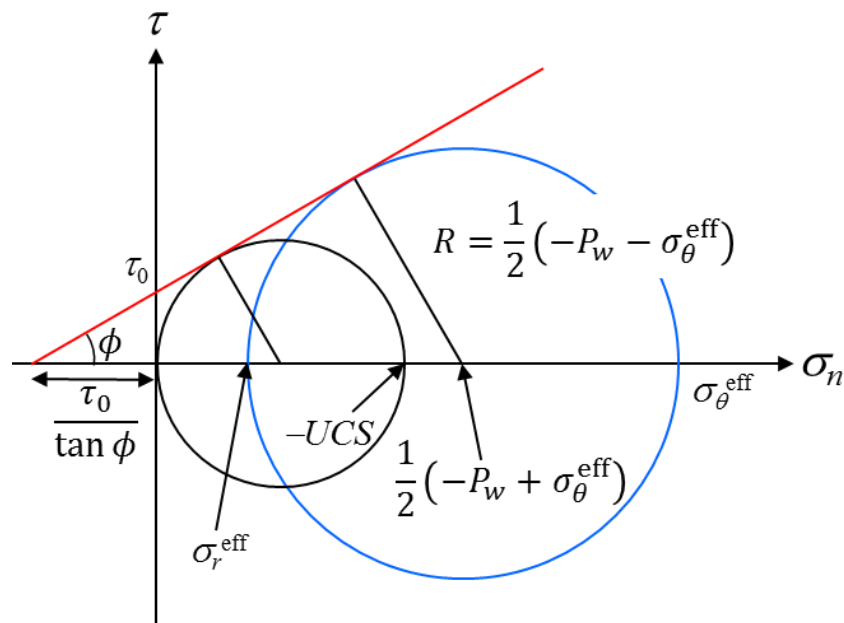
Figure 54 Mohr-Coulomb failure envelope to obtain critical tangential stress

First, we draw a circle using the two principal stresses (blue circle). Next, we draw another circle using *UCS* or uniaxial compressive strength (black circle). Then we can draw the failure envelope (red line). The failure envelope is expressed by

$$\tau = \tau_0 - \mu\tau_n \tag{13}$$

where

τ_0 : cohesion

μ : internal friction coefficient; $\mu = \tan\phi$

ϕ : internal friction angle.

Then, two equations will be geometrically obtained as below.

$$\left\{\frac{\tau_0}{\tan\phi} - \frac{1}{2}\left(-P_w + \sigma_\theta^{\text{eff}}\right)\right\}\sin\phi = \frac{1}{2}\left(-P_w - \sigma_\theta^{\text{eff}}\right) \tag{14}$$

$$\left(\frac{\tau_0}{\tan\phi} + \frac{1}{2}UCS\right)\sin\phi = \frac{1}{2}UCS \tag{15}$$

By solving Eq. (14) and (15) simultaneously, we end up with the expression for the critical tangential stress shown below.

$$\sigma_\theta^{\text{eff,critical}} = -UCS - \frac{1 + \sin\phi}{1 - \sin\phi}P_w \tag{16}$$

Eq. (16) means that high *UCS* and/or high wellbore pressure lead to high critical effective stress, in other words, more stable wellbore.

Finally, the breakout angle, 2θ (shown in Figure 55), will be obtained by solving Eq. (10)
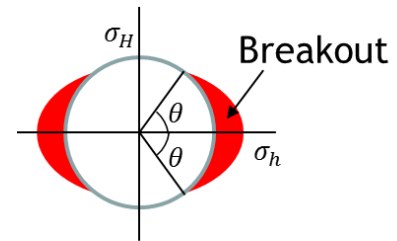
Figure 55 Breakout angle

95

and (16) simultaneously as below because breakout initiates when they are equal.

$$2\theta = \cos^{-1}\left\{ \frac{1}{2(\sigma_H - \sigma_h)}\left(\sigma_H + \sigma_h - \frac{E\Delta S_w}{1 - \nu} + \frac{2}{1 - \sin\phi}P_w + UCS\right)\right\} \quad (17)$$

Now, we calculate the breakout angle. At this depth (5198 ft), we have

$$\sigma_H = -1504 \text{ psi}$$

$$\sigma_h = -1671 \text{ psi}$$

$$P_w = 500 \text{ psi}$$

$$E = 1.1 \times 10^5 \text{ psi}$$

$$\nu = 0.25 \text{ (assumption)}$$

$$\phi = 26° \text{ (Huffman et al. 2016)}$$

$$UCS = 464 - 2900 \text{ psi (Huffman et al. 2016)}$$

$$\Delta S_w = 0.0142.$$

Young's modulus was determined based on the triaxial test (see APPENDIX A).

We assume Poisson's ratio, ν, to be 0.25. Internal friction angle, ϕ, and UCS are

literature values (Huffman et al. 2016). ΔS_w is the swelling of the intact core (Nankai

trough 319-C0009A 9R-1-WR) measured in 2.3.2.
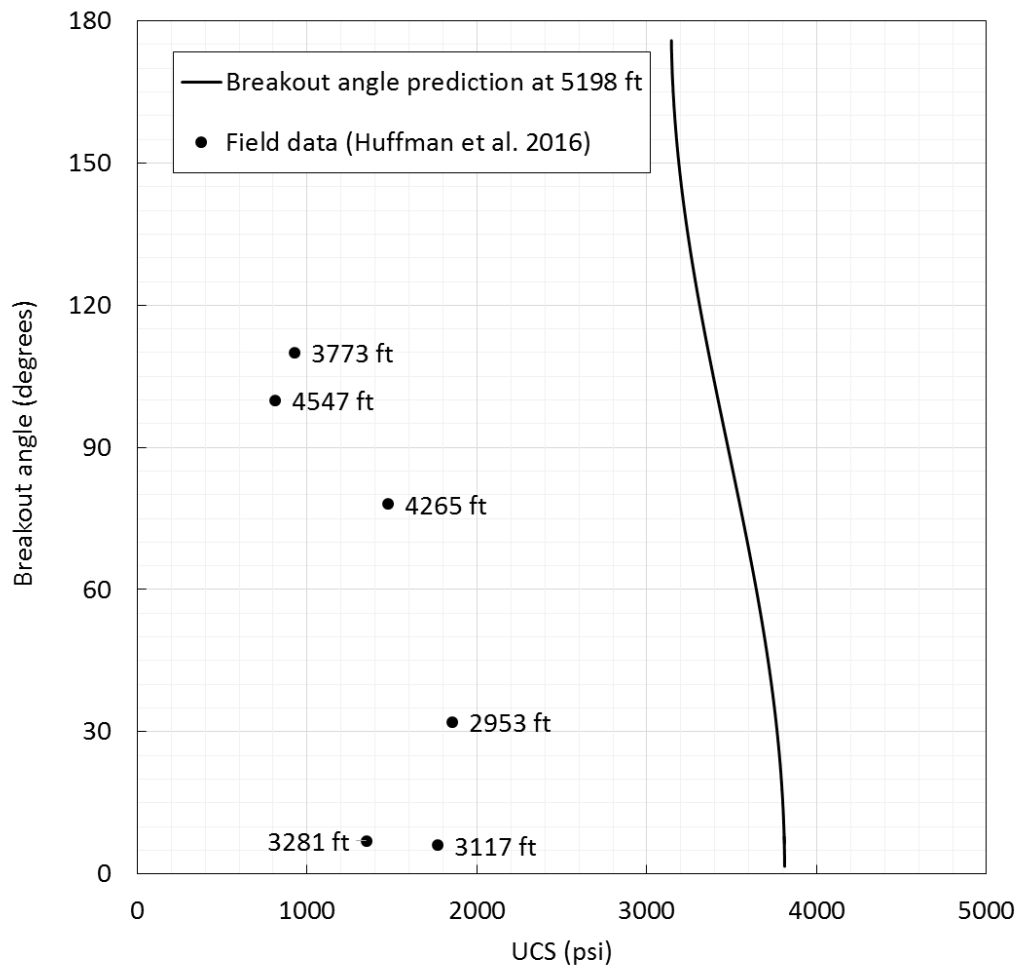
Figure 56 Breakout angle prediction (Solid curve, Eq. (17)) and the field data measured from wellbore image log (filled circles, also shown in Table 23) as a function of *UCS*. Data labels show the depths from which breakout angles were obtained

Figure 56 shows the breakout angle obtained by Eq. (17) as a function of UCS (solid curve). Breakout will be induced ($2\theta > 0°$) when UCS is 3811 psi. And if UCS is less than 3144 psi, breakout will be induced all around the wellbore ($2\theta > 180°$). In comparison, the actual breakout angles determined from wellbore image log by Huffman et al. 2016 were also shown in Figure 56 in black filled circles. As shown in Figure 56, even though the field data was obtained from somewhat different depths, we unreasonably overestimated the breakout angle. There are possibly three reasons as follows.

1) Measured swelling under atmospheric pressure is too high.

2) Non-linearity of the rock.

3) Mohr-Coulomb failure theory predicts too big breakout angle.

Concerning the consistency of swelling measurement, we iteratively calculated UCS required not to induce breakout by Eq. (17) and plotted as a function of linear swelling (Figure 57).
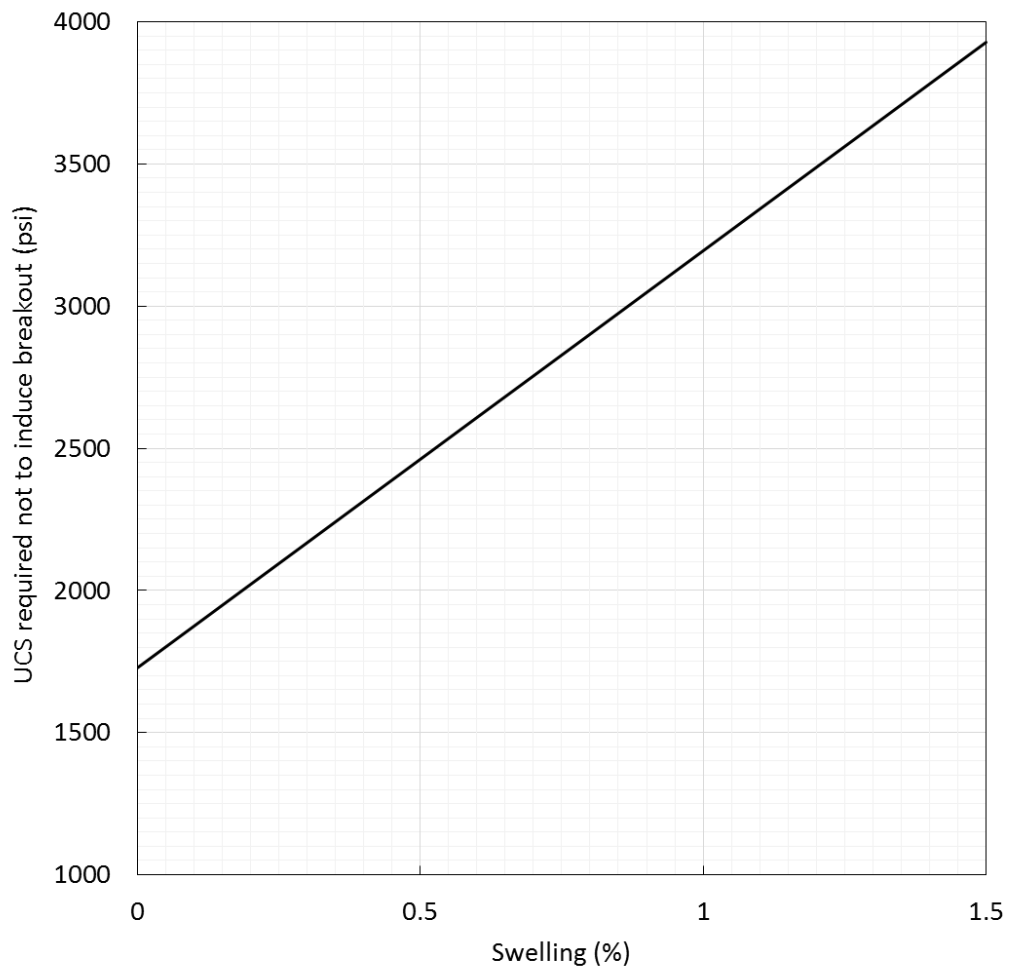
Figure 57 *UCS* **required not to induce breakout as a function of linear swelling calculated by Eq. (17)**

As shown in Figure 57, the *UCS* required for the wellbore stability is very sensitive to swelling. Because of this sensitivity, we investigate the effect of stress on the swelling measurement in the following section.

2.3.4. Effect of Stress

In this section, we focus on the effect of stress on the swelling measurement. We measured the swelling of the pellets and the intact samples for Nankai trough 319-C0009A 9R-1-WR, 338-C0022B 00014X-03-WR, Marcellus shale, and Mancos shale. As described in 2.2.3, the pellet samples were measured with a confining screen and the intact samples were measured without it. The PPGBAE mud shown in Table 16 was used for Nankai trough 319 and 338, and a simple 3 wt% bentonite mud was used for Marcellus shale and Mancos shale. The results are shown in Figure 58, Figure 59, Figure 60, and Figure 61, respectively. Note that results for the intact samples of Nankai 319 are missing because the core sample was not big enough to obtain three intact samples out of it.
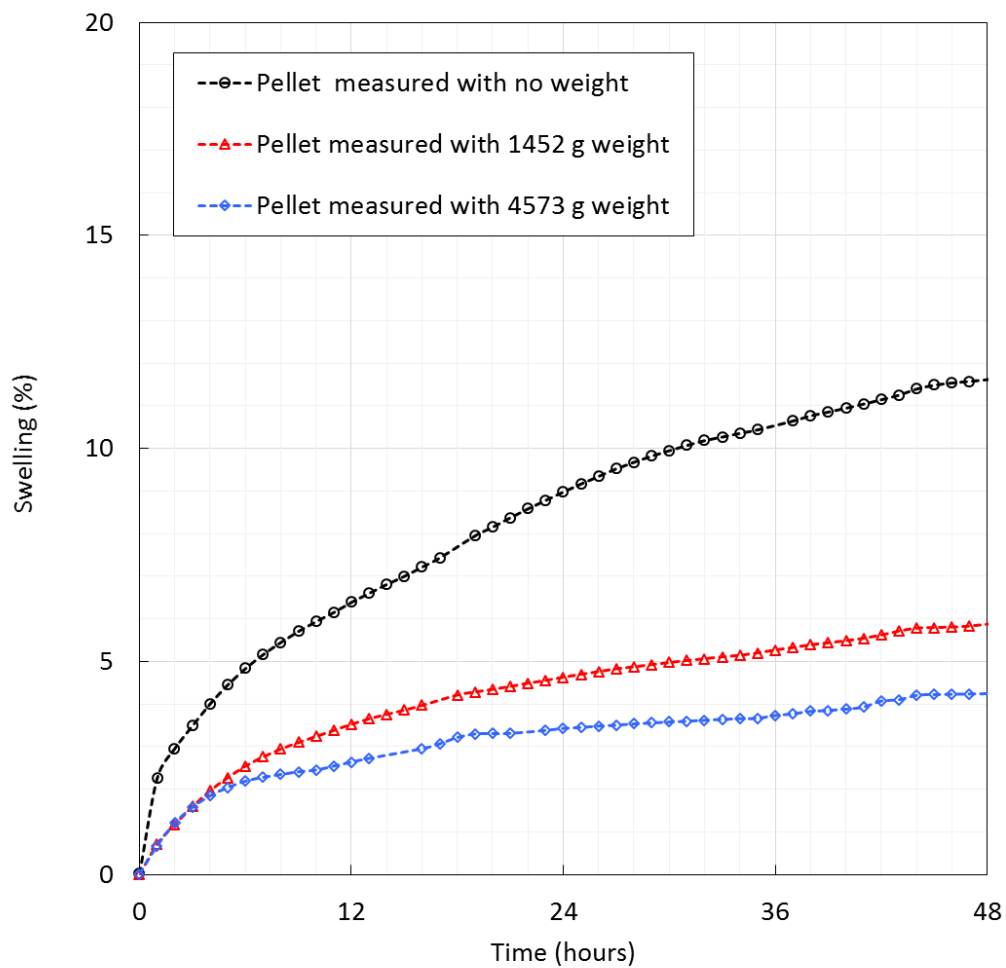
Figure 58 Linear swelling rate for Nankai trough 319-C0009A 9R-1-WR pellet samples in PPGBAE mud with different axial loads
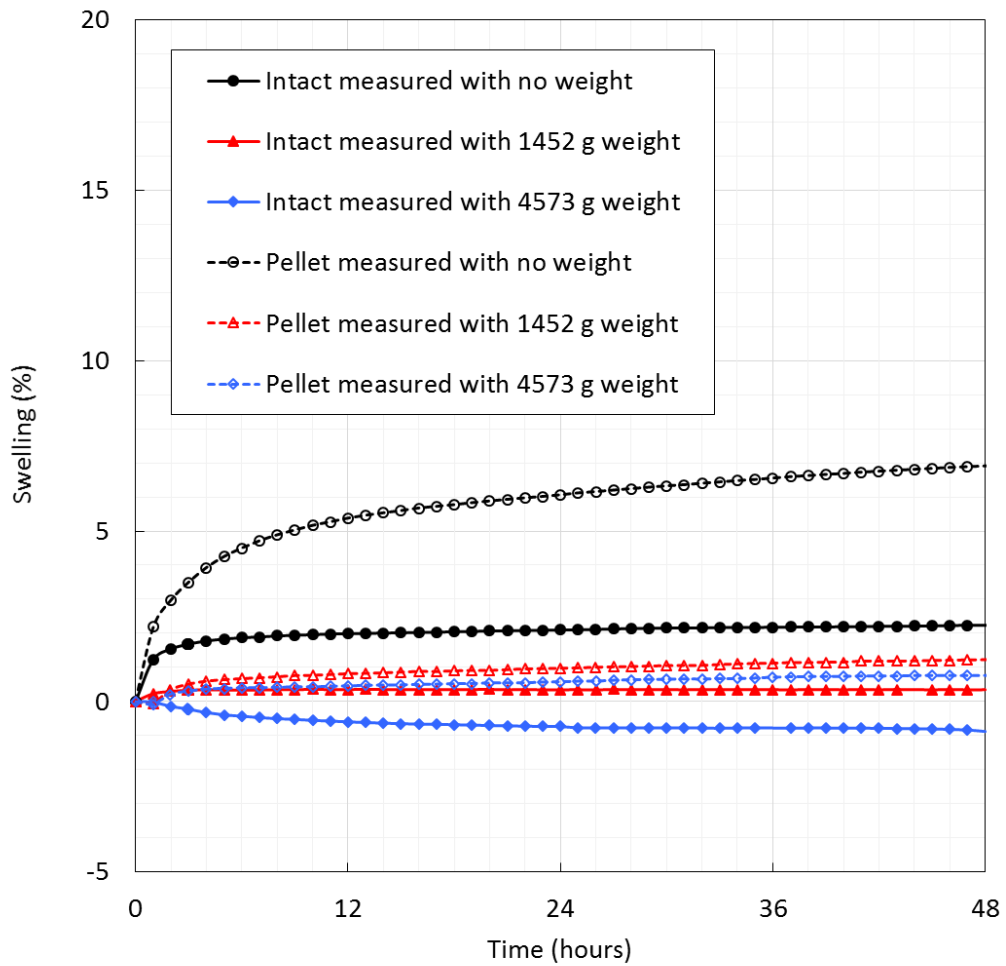
Figure 59 Linear swelling rate for Nankai trough 338-C0022B 00014X-03-WR intact core samples (filled symbols) and pellet samples (open symbols) in PPGBAE mud with different axial loads
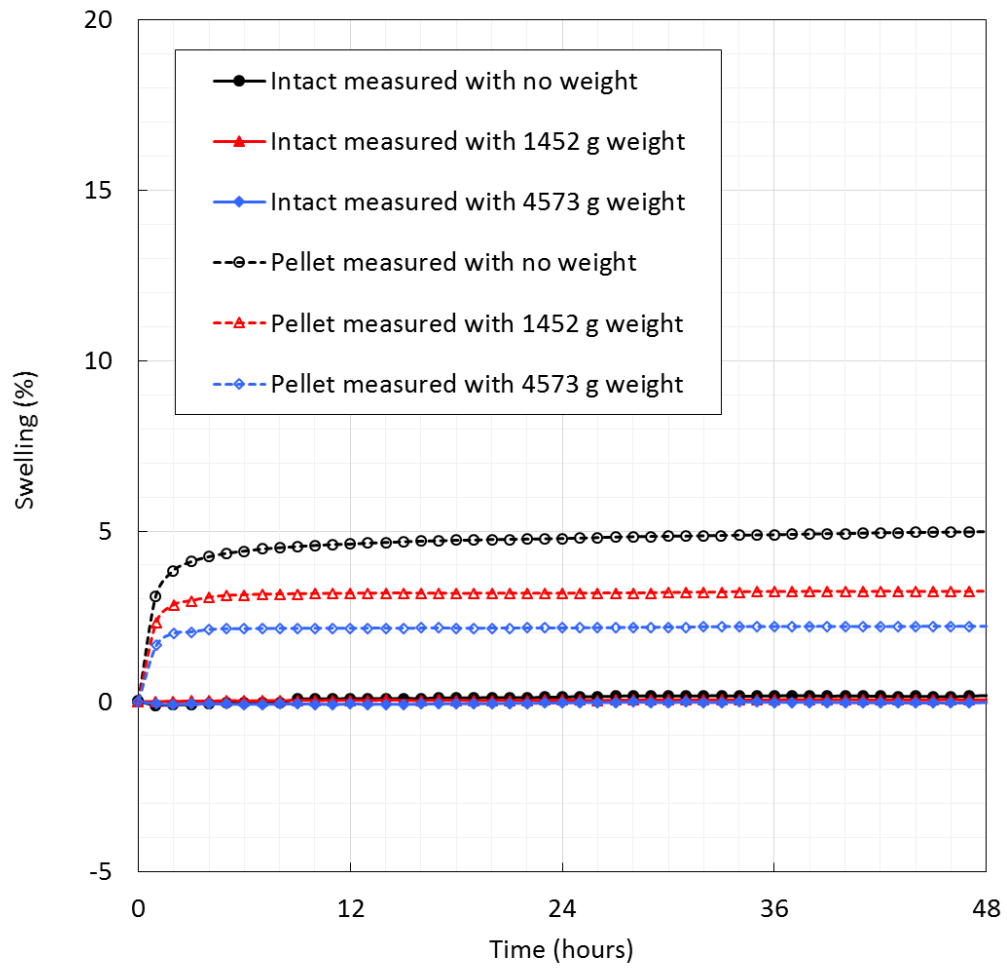
Figure 60 Linear swelling rate for Marcellus intact core samples (filled symbols) and pellet samples (open symbols) in 3 wt% bentonite mud with different axial loads
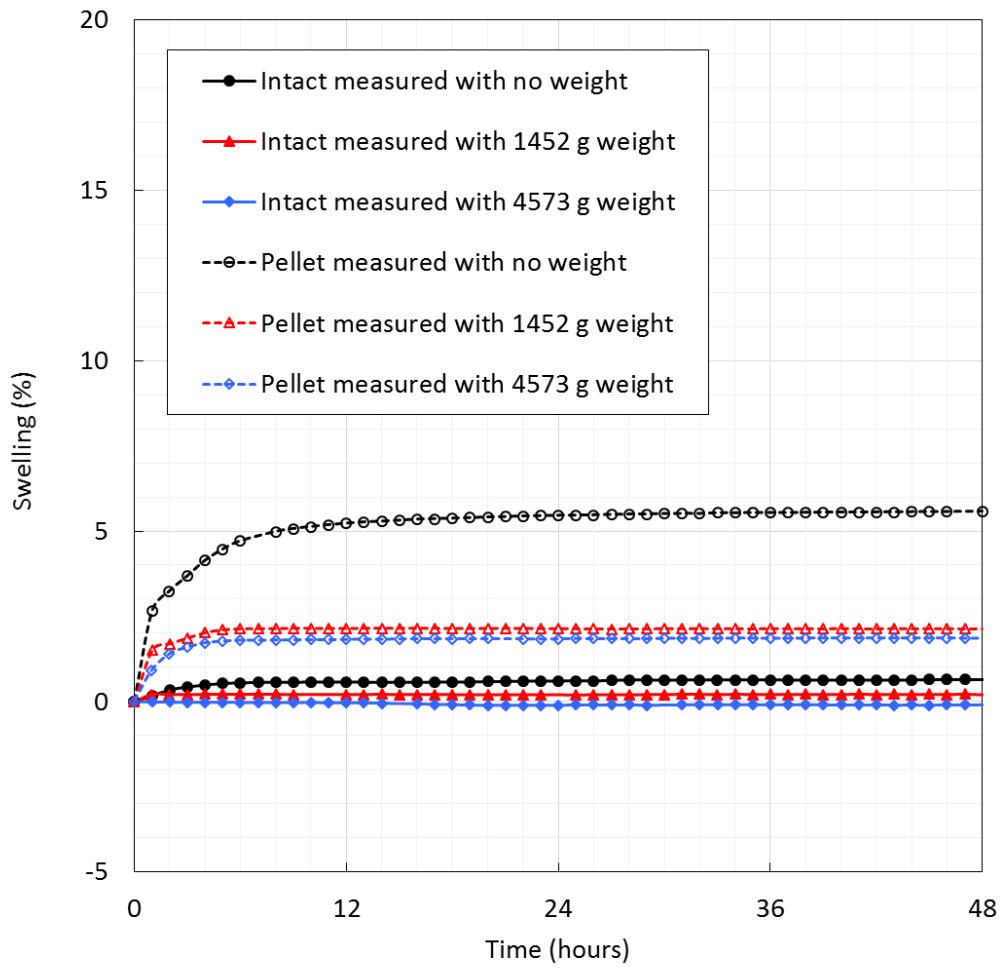
Figure 61 Linear swelling rate for Mancos intact core samples (filled symbols) and pellet samples (open symbols) in 3 wt% bentonite mud with different axial loads

As shown in the figures, negative swelling were observed on the intact samples measured with 4573 g weight. The intact samples slightly swelled laterally because they were not wrapped with a screen. And with the 4573 g weight, they could not overcome the axial load, hence the negative axial displacements were observed. In order to compare the swelling of the intact samples with that of the pellets, we measured the diameter and the length of the intact samples before and after the swelling measurement and calculated volumetric swelling. We regarded 1/3 of the volumetric swelling as the linear swelling to compare with the swelling of the pellet samples. Then, we calculated the ratio of the swelling of the intact sample to that of the pellet under each average stress condition (Table 24 and Figure 62).

Table 24 Summary of swelling after 48 hours under different stress conditions

Sample	Pellet swelling (%)			Intact swelling (%)[*]			Intact/Pellet		
	Low load	Med. load	High load	0.4 psi	1.7 psi	3.8 psi	Low load	Med. load	High load
Nankai 319	11.6	5.87	4.25						
Nankai 338	6.91	1.23	0.77	3.11	1.39	0.61	0.45	1.14	0.79
Marcellus	4.98	3.23	2.21	0.06	0.14	0.17	0.01	0.04	0.08
Mancos	5.57	2.13	1.86	0.63	0.60	0.56	0.11	0.28	0.30

*Calculated by $1/3 \times$ volumetric swelling, measured without screen
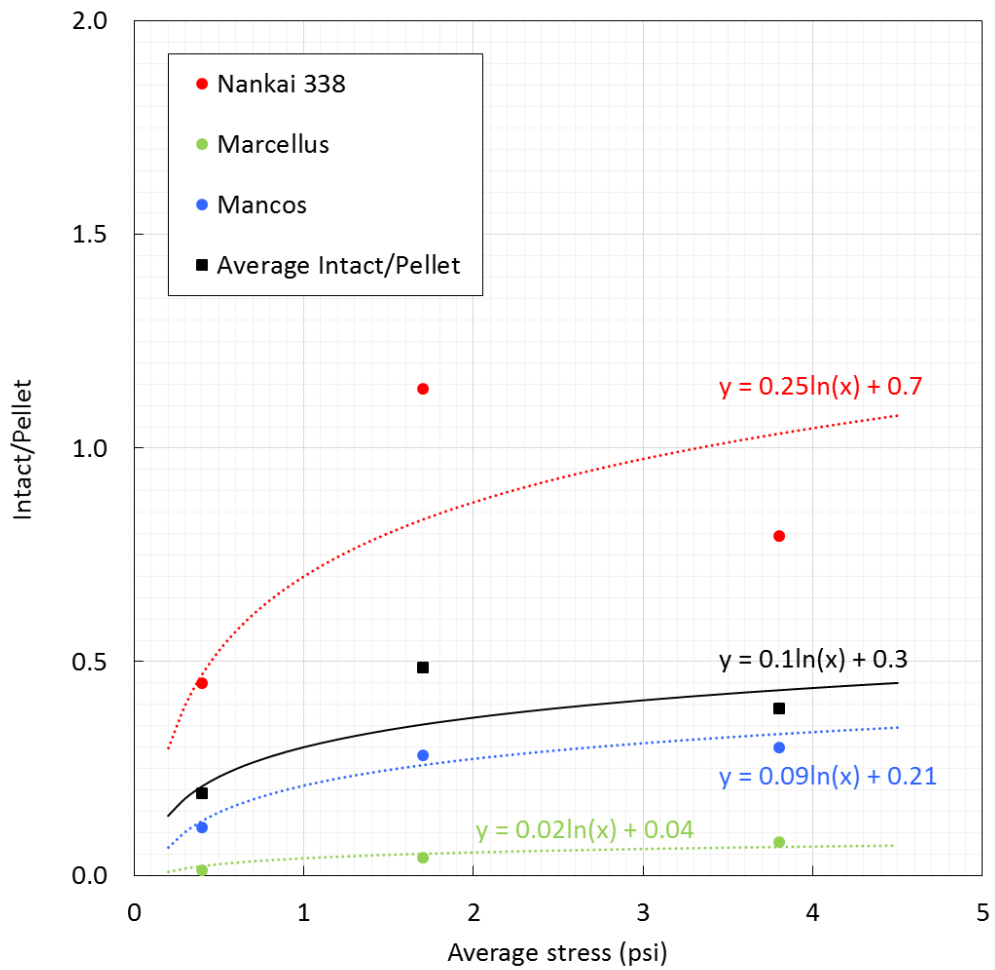
Figure 62 Intact swelling/pellet swelling as a function of average stress. Average values of Intact/Pellet ratio are also shown (black squares)

As shown in Table 24, the ratio of the swelling of the intact sample to that of the pellet sample differs significantly depending on rock type and average stress. As a general trend, however, swelling decreases as the average stress increases, and the swelling of the intact core samples are less than that of the pellet samples regardless of rock type and fluid type.

And also, as shown in Figure 62, the ratio of the swelling of intact sample to that of pellet sample tends to increase, in other words, difference between an intact sample and a pellet sample becomes smaller as the average stress increases. Then, we took the average of the ratio of intact swelling to pellet swelling for each average stress (black squares) and approximated them with a logarithmic formula shown in black in the figure. Approximate functions for each rock are also shown in the figure.

2.3.5. Improved Measurement of Downhole Swelling

As we reviewed in 2.1.1, some studies have been done on the measurement of swelling under high pressure. Zhou et al. (1992) measured volumetric swelling under confining pressure and proposed a theoretical model relating swelling with confining pressure as below.

$$\varepsilon_{\text{swell}} = \frac{1}{3}\theta_{\text{swell}} = B - A \ln \Pi \tag{18}$$

$$\Pi = P_c - P_p, \tag{19}$$

where

θ_{swell} : volumetric swelling

$\varepsilon_{\text{swell}}$: swelling strain

107

P_c : confining pressure

P_p : pore pressure.
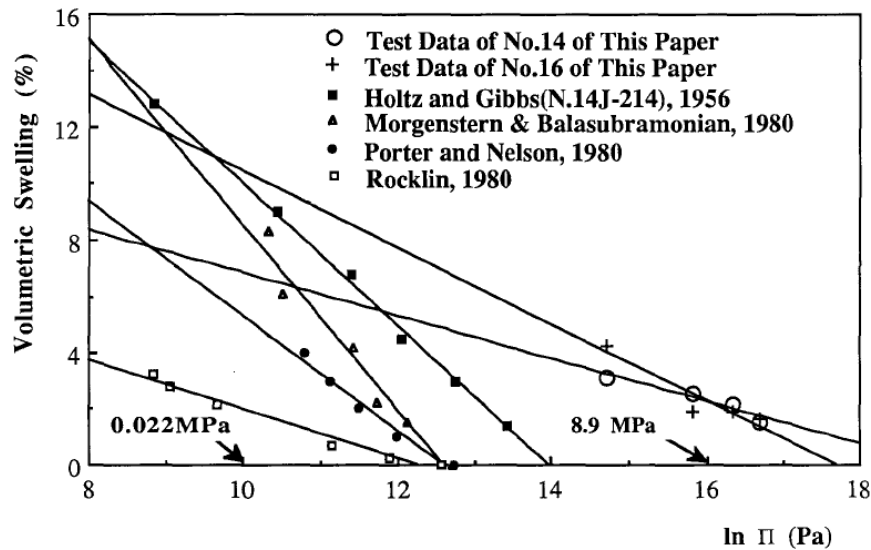
Figure 63 The relations of confining pressure vs. corresponding volumetric swelling strain (Reprinted from Zhou et al. 1992)

Figure 63 is the relations of confining pressure and volumetric swelling from Zhou et al. 1992. They applied the theory to their own data sets and also other literature data and found the theory can be applied throughout the pressure range.

Thus, we plot our results of the intact core swelling for Nankai 319 as a function of average stress on the same graph because in this case the average stress can be regarded as effective stress, Π. The ratio of intact swelling to pellet swelling and thus the volumetric swelling for the Nankai trough 319 was estimated from the approximate function shown in Figure 62 (black curve). Estimated volumetric swelling values are

108

summarized in Table 25. Upper and lower limits of the volumetric swelling are also

calculated from the approximate function for Nankai trough 338 and Marcellus shale

shown in Figure 62, respectively and summarized.

Table 25 Summary of estimated swelling for Nankai trough 319-C0009A 9R-1-WR

Average stress (psi)	Pellet swelling (%)	Intact/Pellet			Vol. swelling (%)[***]		
		Ave.	Upper limit[*]	Lower limit[**]	Ave.	Upper limit	Lower limit
0.4	11.6	0.208	0.471	0.022	7.26	16.4	0.76
1.7	5.87	0.353	0.833	0.051	6.22	14.7	0.89
3.8	4.25	0.434	1.03	0.067	5.53	13.2	0.85

*Calculated from the approximate function for Nankai trough 338
**Calculated from the approximate function for Marcellus shale
***Calculated by Pellet swelling $\times$ Intact/Pellet $\times$ 3

Figure 64 shows the relations of confining pressure or average stress with

corresponding volumetric swelling. Error bars show the upper and the lower limits that

we discussed above.
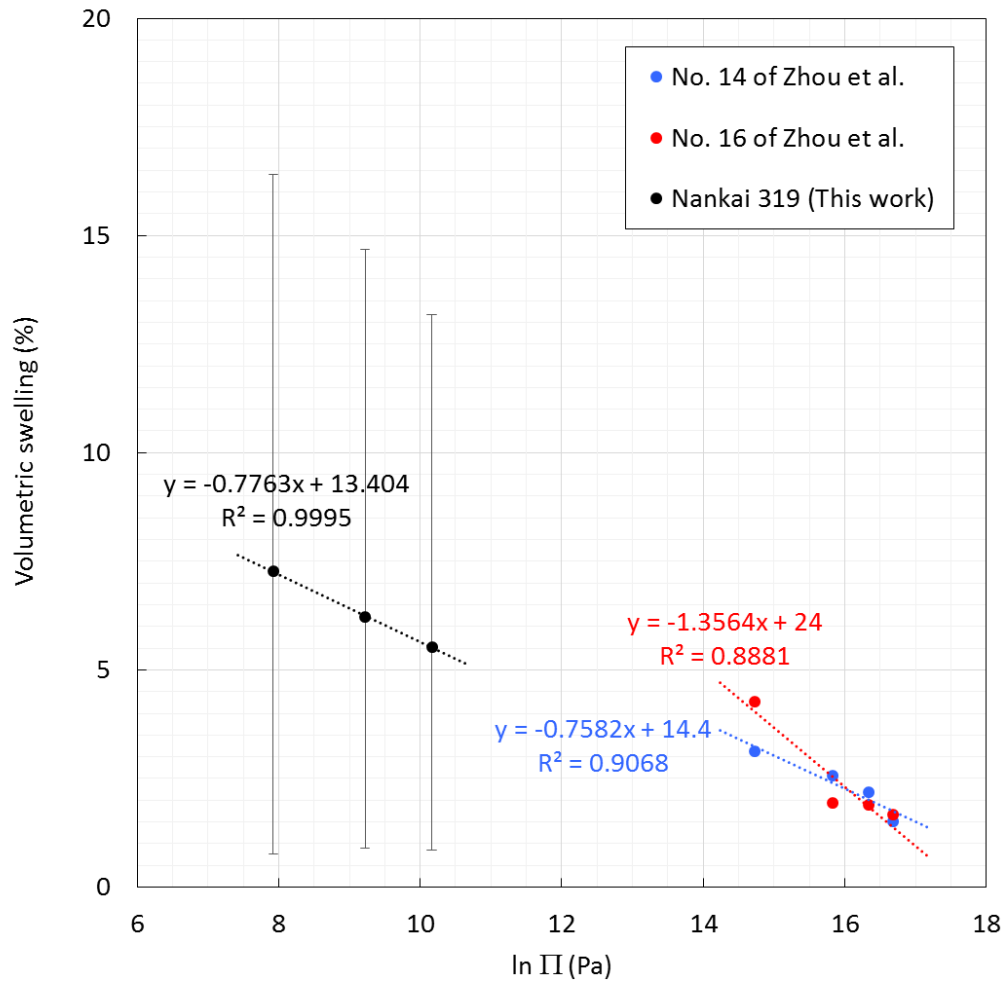
Figure 64 The relations of confining pressure or average stress vs. corresponding volumetric swelling strain Error bars show the upper and the lower limits calculated from the approximate function for Nankai trough 338 and Marcellus shale shown in Figure 59, respectively

As shown in Figure 64, in Eq. (18), for No. 14, $A = 0.25$ and $B = 4.8$. For No. 16, $A = 0.45$ and $B = 8.0$, that were determined by Zhou et al.. Note that y-axis of the graph is volumetric swelling (θ_{swell}), not swelling strain (ε_{swell}). And For Nankai 319, A and B were determined to be $A = 0.26$ and $B = 4.5$ although this is a quite rough estimation.

Now, we need to extrapolate the swelling value to the downhole condition at 5198 ft. To express the downhole stresses at 5198 ft, as described in 2.3.3, we have

$$\sigma_r^{eff} = -P_w = -500 \text{ psi} \tag{20}$$

$$\sigma_\theta^{eff} = \sigma_H + \sigma_h - 2(\sigma_H - \sigma_h)\cos 2\theta + P_w - \frac{E}{1-\nu}\Delta S_w$$

$$= -3175 - 334\cos 2\theta + 500 - \frac{E}{1-\nu}\Delta S_w$$

$$= -3009 - 1.47 \times 10^5 \Delta S_w \tag{21}$$

$$\sigma_z^{eff} = \sigma_\nu - 2\nu(\sigma_H - \sigma_h)\cos 2\theta - \frac{E}{1-\nu}\Delta S_w$$

$$= -1931 - 334\nu\cos 2\theta - \frac{E}{1-\nu}\Delta S_w$$

$$= -2015 - 1.47 \times 10^5 \Delta S_w \tag{22}$$

where

$$E = 1.1 \times 10^5 \text{ psi}$$

$$\nu = 0.25 \text{ (assumption)}$$

$$\theta = 0° \text{ (direction of } \sigma_h).$$

Note that θ was set to be 0 because breakout initiates in the direction of σ_h. Because Zhou's effective stress (Π) and our average stress are equivalent, ΔS_w will be written by

$$\Delta S_w = \left\{ 4.5 - 0.26 \ln \frac{-\left(\sigma_r^{eff} + \sigma_\theta^{eff} + \sigma_z^{eff}\right)/145 \times 10^6}{3} \right\} \times \frac{1}{100} \quad (23)$$

From Eq. (20) - (23), we can iteratively obtain

$$\sigma_r^{eff} = -500 \; psi$$

$$\sigma_\theta^{eff} = -3314 \; psi$$

$$\sigma_z^{eff} = -2320 \; psi$$

$$\Delta S_w = 0.00208.$$

2.3.6. Improved Prediction of Breakout Angle

By substituting the values obtained in the previous section in Eq. (17), we can obtain improved breakout angle prediction shown in Figure 65.

As shown in Figure 65, the improved breakout prediction matches Huffman's data much better than the original one. Thus, we can significantly improve the breakout angle prediction by taking the effect of stress into account when estimating the downhole swelling. Note that this is a quite rough estimation because we used the average of intact swelling/pellet swelling values to estimate the unavailable intact core swelling for the Nankai trough 319. Breakout angle could be predicted much more accurately if intact core samples for the Nankai trough 319 were available and their swelling were measured under different stress conditions.
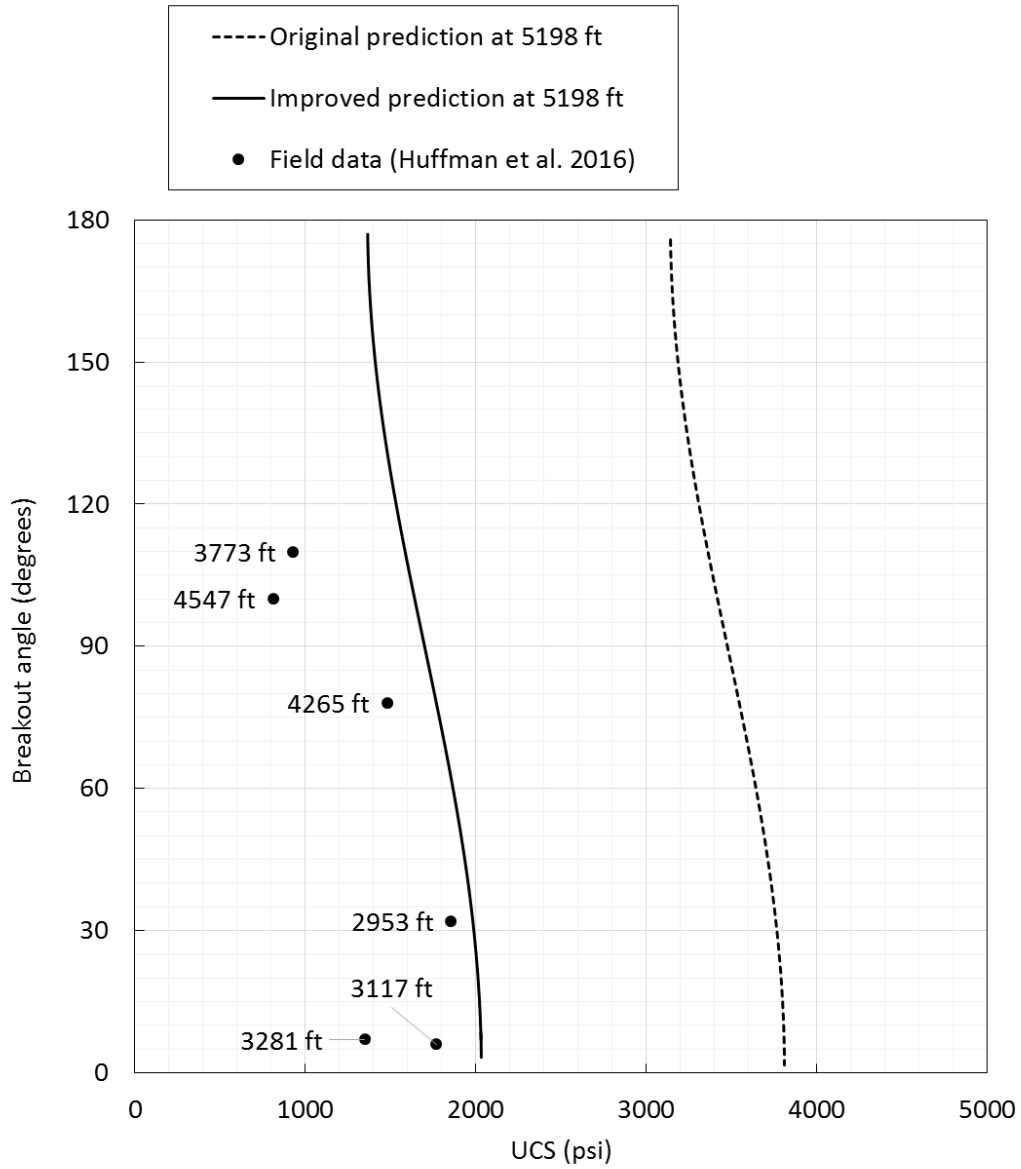
Figure 65 Original breakout angle prediction (dashed curve, also shown in Figure 56), improved prediction (solid curve), and field data measured from wellbore image log (filled circles, also shown in Table 23) as a function of *UCS*. Data labels show the depths from which breakout angles were obtained

2.3.7. Stress around the wellbore

Lastly, assuming that drawdown, Δp, and temperature change, ΔT, are zero, the effective stresses around the wellbore at $\theta = 0°$ (direction of σ_h) and $\theta = 90°$ (direction of σ_H) from Eq. (2) - (4) can be written as below (see APPENDIX B for integration).

For $r_w \leq r < r_S$,

$$\sigma_r^{\text{eff}} = \frac{1}{2}(\sigma_H + \sigma_h) - \left(\frac{1}{2}\sigma_H + \frac{1}{2}\sigma_h + P_w\right)\left(\frac{r_w}{r}\right)^2$$

$$-\frac{1}{2}\frac{1}{r^2}\frac{E\Delta S_w}{1-\nu}\left[r^2 - r_w^2 - \frac{1}{\ln(r_S/r_w)}\left\{r^2\ln\frac{r}{r_w} - \frac{1}{2}(r^2 - r_w^2)\right\}\right] \quad (24)$$

$$+\frac{1}{2}\left\{1 + 3\left(\frac{r_w}{r}\right)^4 - 4\left(\frac{r_w}{r}\right)^2\right\}(\sigma_H - \sigma_h)\cos 2\theta$$

$$\sigma_\theta^{\text{eff}} = \frac{1}{2}(\sigma_H + \sigma_h) + \left(\frac{1}{2}\sigma_H + \frac{1}{2}\sigma_h + P_w\right)\left(\frac{r_w}{r}\right)^2$$

$$+\frac{1}{2}\frac{E\Delta S_w}{1-\nu}\left[r^2 - r_w^2 - \frac{1}{\ln(r_S/r_w)}\left\{r^2\ln\frac{r}{r_w} - \frac{1}{2}(r^2 - r_w^2)\right\}\right] \quad (25)$$

$$-\frac{E\Delta S_w}{1-\nu}\left\{1 - \frac{\ln(r/r_w)}{\ln(r_S/r_w)}\right\} - \frac{1}{2}\left\{1 + 3\left(\frac{r_w}{r}\right)^4\right\}(\sigma_H - \sigma_h)\cos 2\theta$$

$$\sigma_z^{\text{eff}} = \sigma_v - \frac{E\Delta S_w}{1-\nu}\left\{1 - \frac{\ln(r/r_w)}{\ln(r_S/r_w)}\right\} - 2\nu\left(\frac{r_w}{r}\right)^2(\sigma_H - \sigma_h)\cos 2\theta. \quad (26)$$

For $r_S \leq r$,

$$\sigma_r^{\text{eff}} = \frac{1}{2}(\sigma_H + \sigma_h) - \left(\frac{1}{2}\sigma_H + \frac{1}{2}\sigma_h + P_w\right)\left(\frac{r_w}{r}\right)^2$$

$$- \frac{1}{2}\frac{1}{r^2}\frac{E\Delta S_w}{1-\nu}\left[r_S^2 - r_w^2 - \frac{1}{\ln(r_S/r_w)}\left\{r_S^2\ln\frac{r_S}{r_w} - \frac{1}{2}(r_S^2 - r_w^2)\right\}\right] \quad (27)$$

$$+ \frac{1}{2}\left\{1 + 3\left(\frac{r_w}{r}\right)^4 - 4\left(\frac{r_w}{r}\right)^2\right\}(\sigma_H - \sigma_h)\cos 2\theta + \Delta p$$

$$\sigma_\theta^{\text{eff}} = \frac{1}{2}(\sigma_H + \sigma_h) + \left(\frac{1}{2}\sigma_H + \frac{1}{2}\sigma_h + P_w\right)\left(\frac{r_w}{r}\right)^2$$

$$+ \frac{1}{2}\frac{E\Delta S_w}{1-\nu}\left[r_S^2 - r_w^2 - \frac{1}{\ln(r_S/r_w)}\left\{r_S^2\ln\frac{r_S}{r_w} - \frac{1}{2}(r_S^2 - r_w^2)\right\}\right] \quad (28)$$

$$- \frac{1}{2}\left\{1 + 3\left(\frac{r_w}{r}\right)^4\right\}(\sigma_H - \sigma_h)\cos 2\theta$$

$$\sigma_z^{\text{eff}} = \sigma_v - 2\nu\left(\frac{r_w}{r}\right)^2(\sigma_H - \sigma_h)\cos 2\theta. \quad (29)$$

Substituting

$$\sigma_H = -1504 \text{ psi}$$

$$\sigma_h = -1671 \text{ psi}$$

$$P_w = 500 \text{ psi}$$

$$E = 1.1 \times 10^5 \text{ psi}$$

$$\nu = 0.25$$

$$\Delta S_w = 0.00208$$

and also

$$r_w = 12.25 \text{ in (drilling report available at http://sio7.jamstec.go.jp/)}$$

$$r_S = 18 \text{ in (assumption)}$$

$\alpha = 1$ (assumption),

we plot the effective stresses as a function of r/r_w as shown in Figure 66 (at $\theta = 0°$, direction of σ_h) and Figure 67 (at $\theta = 90°$, direction of σ_H).

The plots for $\Delta S_w = 0.0142$, which we measured in 2.3.2 for the intact core sample of Nankai trough 319-C0009A 9R-1-WR with no weight, are also shown for comparison (Figure 68 and Figure 69). Furthermore, $\sigma_\theta^{\text{eff}}$ for various ΔS_w values as a function of r/r_w and $\sigma_\theta^{\text{eff}}$ at the wellbore surface as a function of ΔS_w are shown in Figure 70 (at $\theta = 0°$, direction of σ_h), Figure 71(at $\theta = 90°$, direction of σ_H), and Figure 72, respectively.
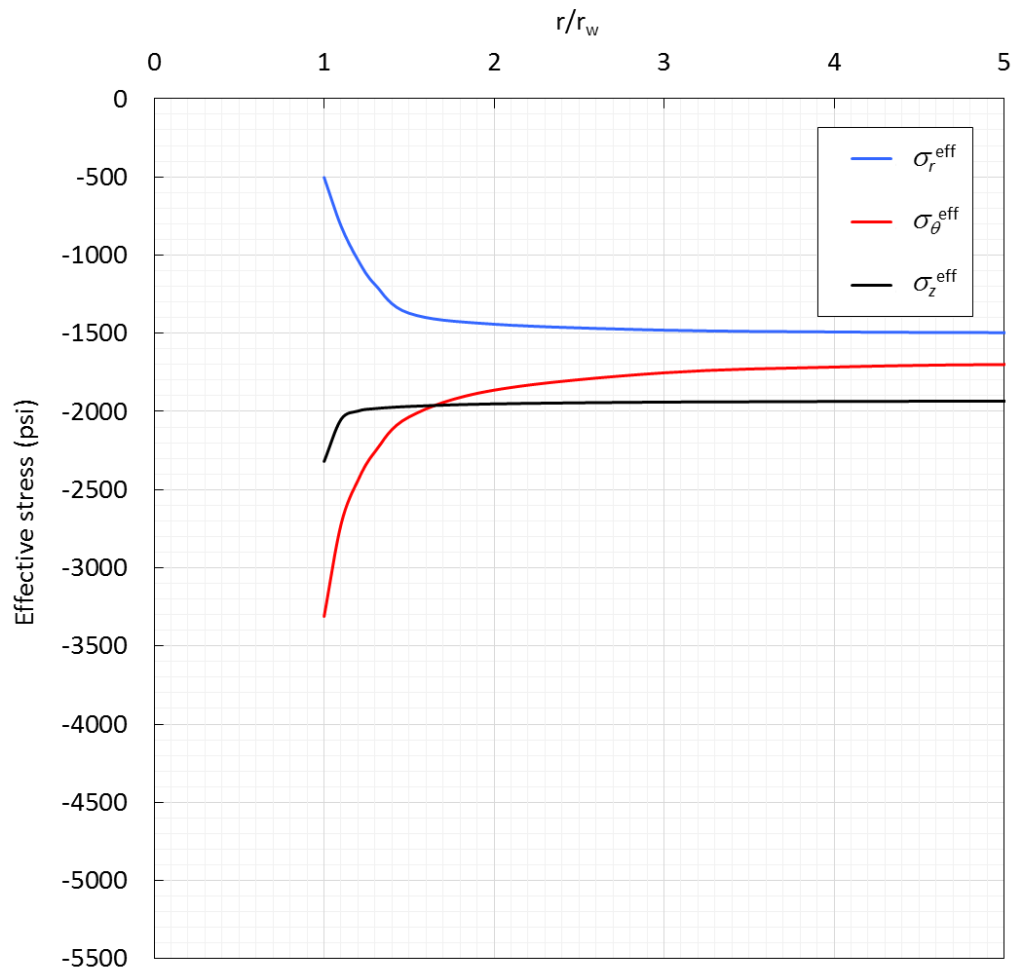
Figure 66 Variation of effective stresses at $\theta = 0^\circ$ (direction of σ_h) with distance from the wellbore when $\Delta S_w = 0.00208$
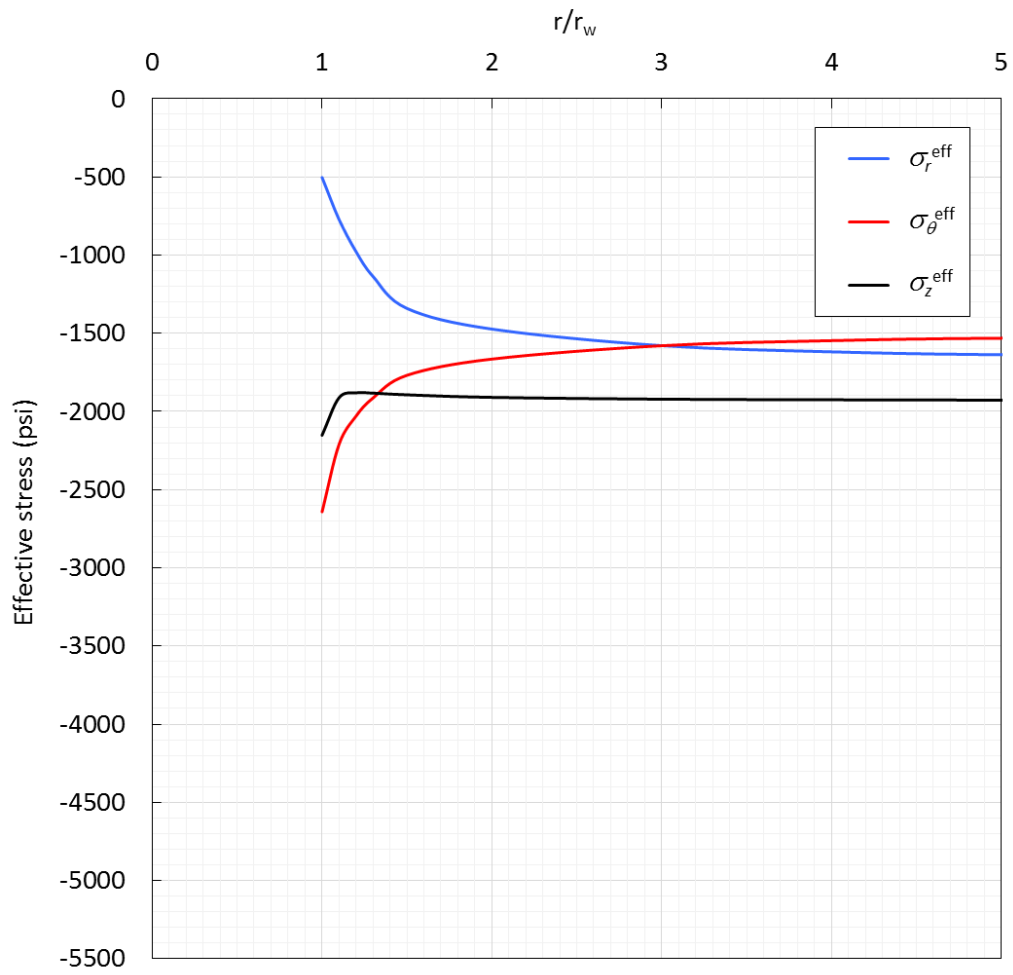
Figure 67 Variation of effective stresses at $\theta = 90^\circ$ (direction of σ_H) with distance from the wellbore when $\Delta S_w = 0.00208$
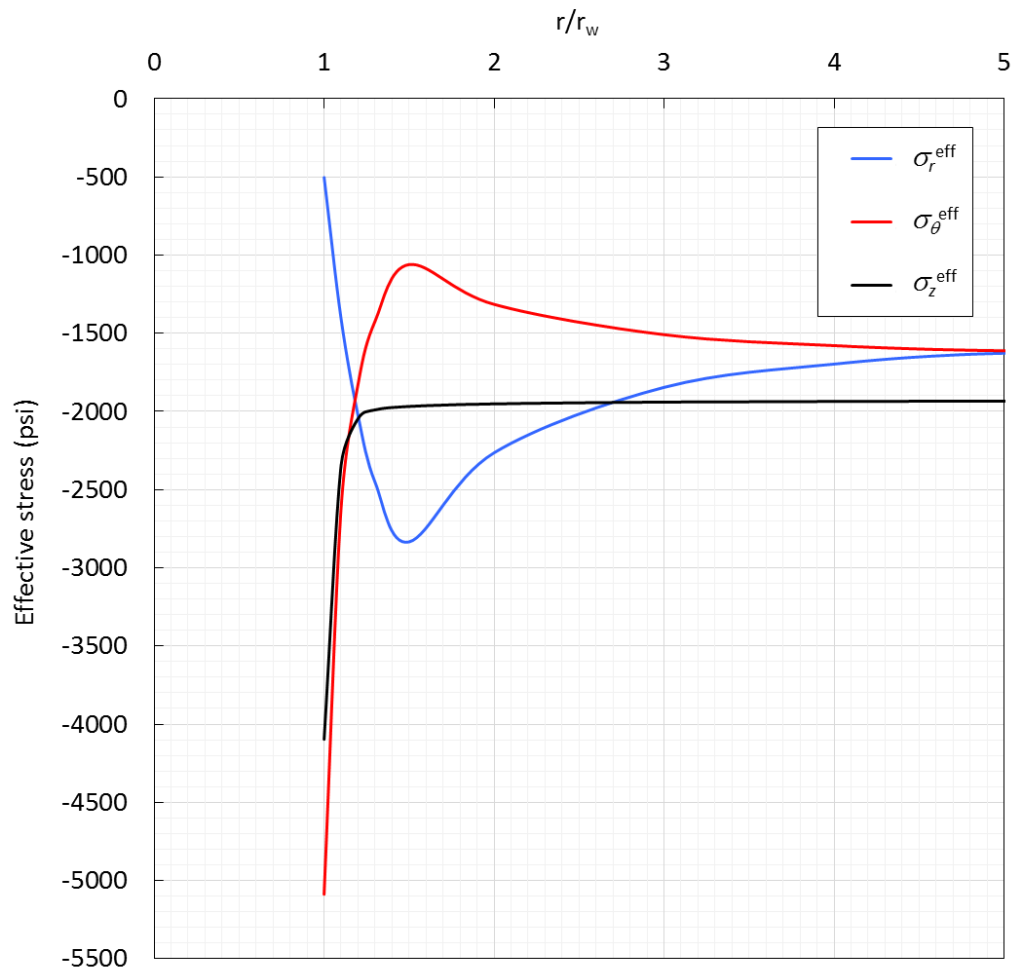
Figure 68 Variation of effective stresses at $\theta = 0^\circ$ (direction of σ_h) with distance from the wellbore when $\varDelta S_w = 0.0142$
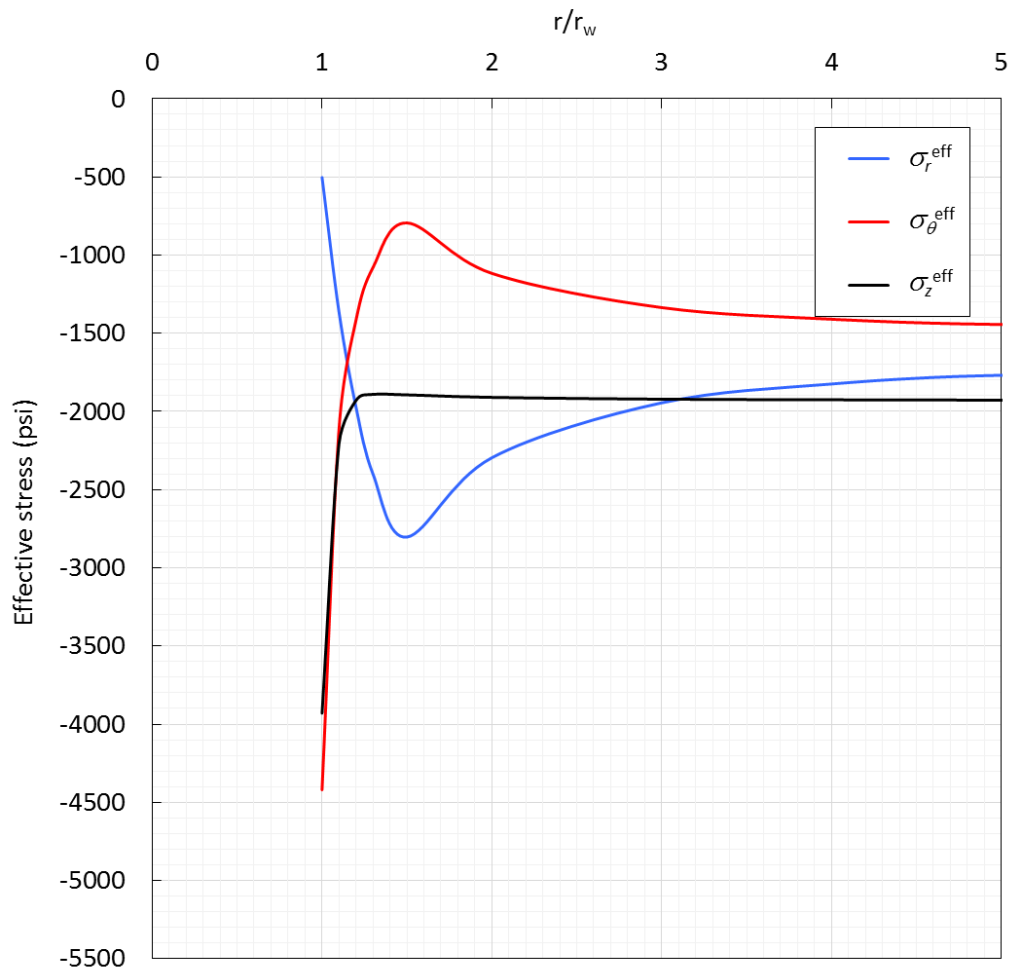
Figure 69 Variation of effective stresses at $\theta = 90^\circ$ **(direction of** σ_H**) with distance from the wellbore when** $\Delta S_w = 0.0142$
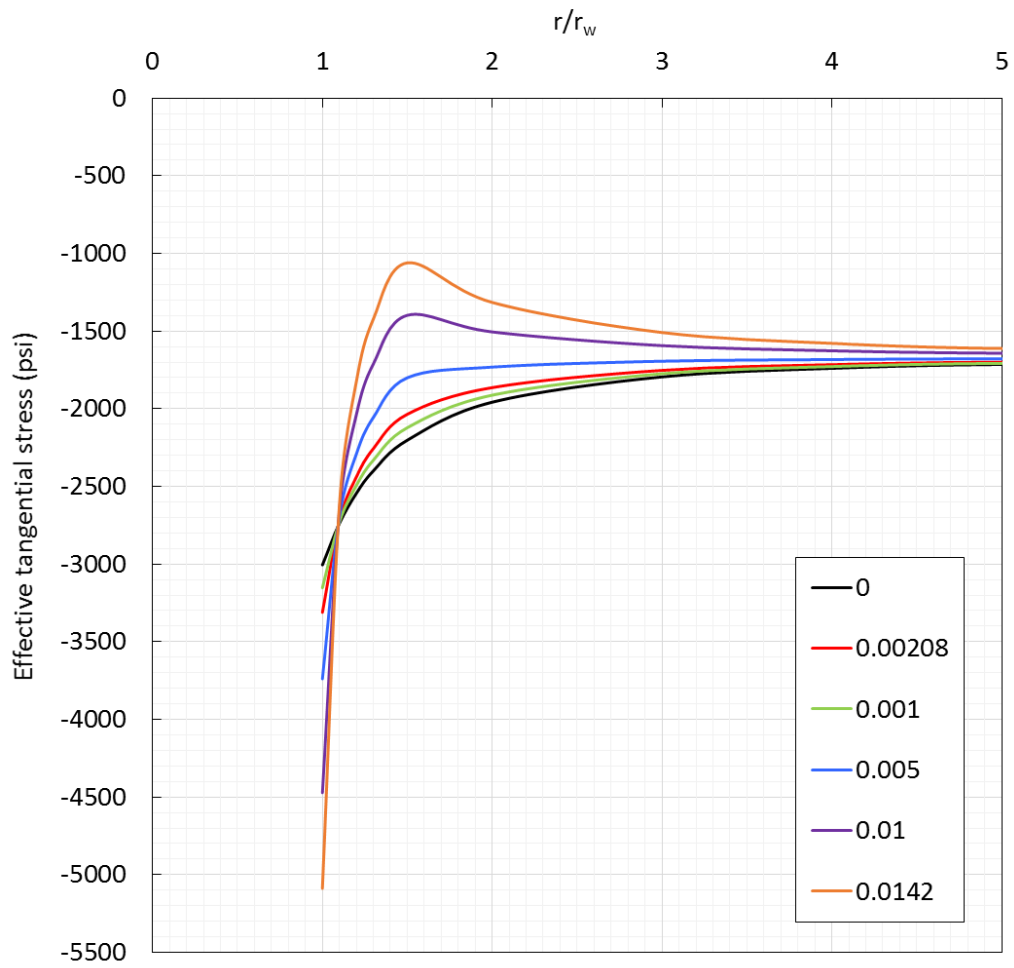
Figure 70 Variation of effective tangential stress at $\theta = 0°$ (direction of σ_h) with distance from the wellbore for various ΔS_w
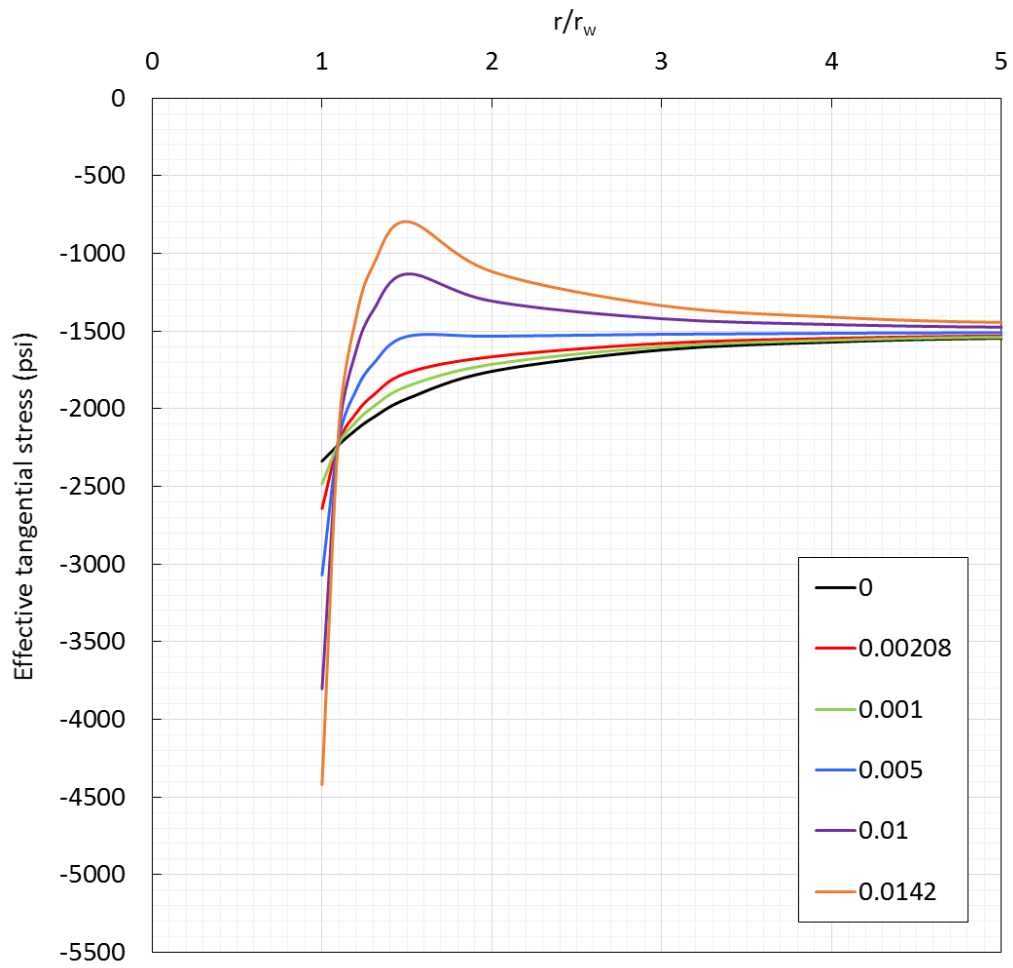
Figure 71 Variation of effective tangential stress at $\theta = 90^\circ$ (direction of σ_H) with distance from the wellbore for various $\varDelta S_w$
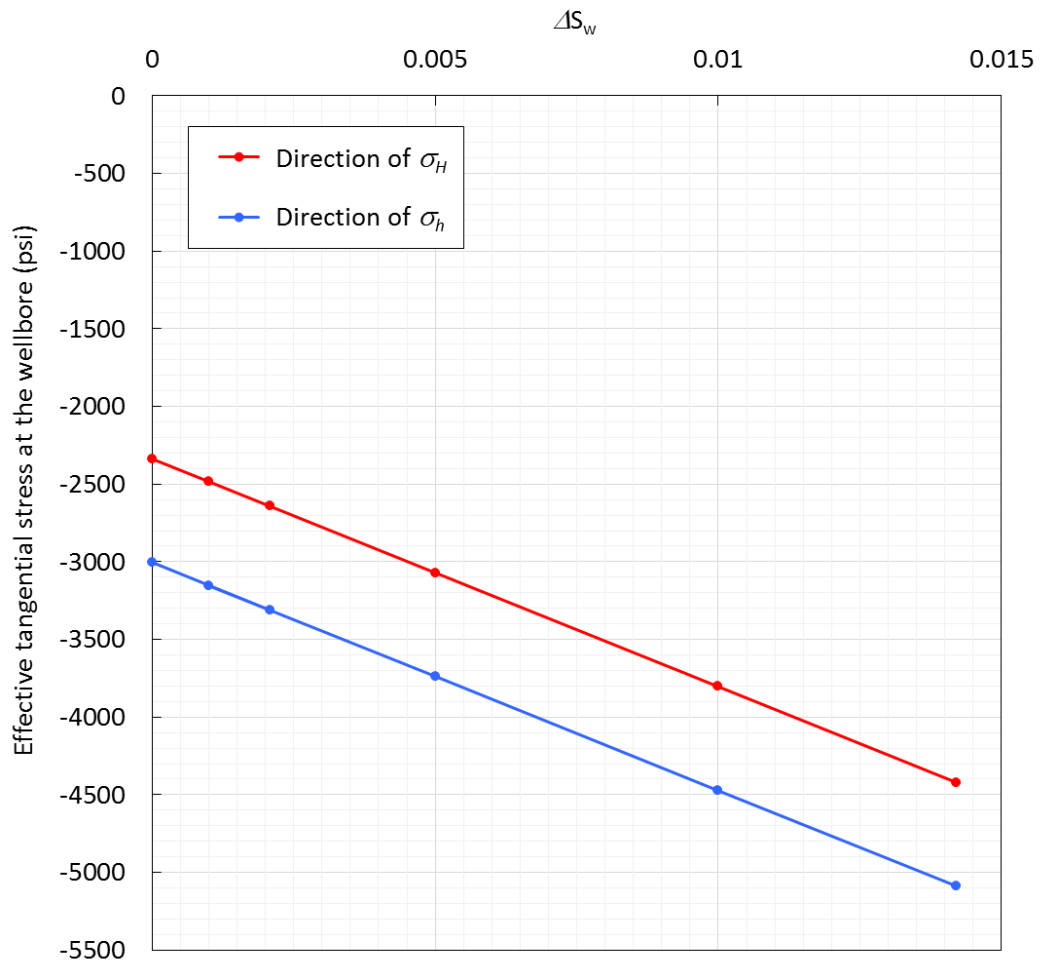
Figure 72 Dependence of $\sigma_{\theta}^{\mathrm{eff}}$ on $\varDelta S_w$ at the wellbore surface

As shown in Figure 66 - Figure 69, stress condition around the wellbore depends heavily on ΔS_w. Also, $\sigma_\theta^{\text{eff}}$ in the direction of σ_h is always greater than that in the direction of σ_H. That is why breakout initiates in the direction of σ_h.

As shown in Figure 70 - Figure 72, $\sigma_\theta^{\text{eff}}$ depends heavily on ΔS_w.as was the case with the *UCS* required for the wellbore stability discussed in 2.3.3. Even with the swelling of 0.5 %, for example, $\sigma_\theta^{\text{eff}}$ in the direction of σ_h increases by approximately 23 % (700 psi). Therefore, swelling inhibition is extremely important to maintain the wellbore stability.

2.4. Concluding Remarks

2.4.1. Summary

- Swelling was significantly reduced by means of Ewy and Morton's method. However, there was still a big discrepancy between pellet swelling and intact core swelling

- Wellbore instability, or breakout angle can be analytically predicted

- Breakout angle will be seriously overestimated if the effect of stress is not taken into account when measuring the swelling

- Downhole swelling can be estimated by extrapolating the swelling values measured under different axial loads

- The breakout angle prediction can significantly be improved by taking the effect of stress on swelling into account

- The breakout angle prediction could be improved further if intact core samples were available

- Swelling inhibition is extremely important to maintain the wellbore stability

2.4.2. Recommended Procedure to Predict Downhole Swelling and Breakout Angle

1) If intact core samples are available, measure the swelling for the intact samples under different average stress conditions by adding a weight on the swelling indicator of the LSM (in this study, 0.4 psi, 1.7 psi, and 3.8 psi). To determine the average stress conditions, the sample should not be wrapped with a screen.

2) If intact core samples are not available, create pellets from the cuttings obtained from the formation in question by means of Ewy and Morton's method and measure the swelling under different average stress conditions. The pellet should be wrapped with a screen in this case to avoid lateral swelling.

   Multiply the swelling under each average stress condition by the ratio of intact swelling to pellet swelling for each average stress condition (in this study, 0.21, 0.35, and 0.43, respectively) to estimate the swelling of unavailable intact core samples.

3) Fit the measured or estimated intact core swelling to Zhou et al. 1992 theory to determine the constants A and B.

4) From the equations for the in situ effective stresses (Eq. (20) - (22)) and Zhou's equation obtained above, iteratively calculate the downhole swelling as well as in situ effective stresses at the wellbore surface.

5) Breakout angle can be analytically predicted by Eq. (17) if UCS of the formation in question is known.

3. CONCLUSIONS

This work represented a comprehensive, systematic, and comparative study on high performance water base mud that contains a shale inhibitor. In order to improve the rheology and the fluid loss property of the mud without adversely affecting its shale inhibiting performance, PVOH was introduced as a new polymeric deflocculant.

This work also represented the improved methodology of estimation of downhole swelling. In order to predict the wellbore instability more precisely even when an intact core sample is not available, swelling of a pellet sample was measured under different stress conditions and extrapolated to the downhole condition to analytically predict the wellbore instability.

Under the stated aims, and within the limitation of this work, the following conclusions can be made.

- PVOH works as a deflocculant better than lignosulfonate

- DP should be low so it does not significantly affect the mud rheology

- DH = 88 % works the best as a deflocculant

- PVOH 3-88 (DP = 300, DH = 88 %) would be the best choice

- PVOH content should be determined according to bentonite content, not PPGBAE content. Practically, we would recommend to use the same amount of PVOH as bentonite

- PVOH works better with PPGBAE than with KCl due to its incompatibility with high concentration KCl

- pH of the mud does not affect the fluid loss properties as long as there is enough PVOH in the system

- PVOH is compatible with most additives commonly used

- Hot-rolling lowers the performance of PVOH but it is still better than that of lignosulfonate before hot-rolling

- PPGBAE and PVOH content significantly affects the swelling and needs to be optimized to achieve low shale swelling

- Swelling was significantly reduced by means of Ewy and Morton's method. However, there was still a big discrepancy between pellet swelling and intact core swelling

- Wellbore instability, or breakout angle can be analytically predicted

- Breakout angle will be seriously overestimated if the effect of stress is not taken into account when measuring the swelling

- Downhole swelling can be estimated by extrapolating the swelling values measured under different axial loads

- The breakout angle prediction can significantly be improved by taking the effect of stress on swelling into account

- The breakout angle prediction could be improved further if intact core samples were available

- Swelling inhibition is extremely important to maintain the wellbore stability

REFERENCES

Bourgoyne, A. T. Jr., Millheim, K. K. Jr., Chenevert, M. E., and Young, F. S. Jr. 1991 Applied Drilling Engineering

Chang, S. H., Gupta, R. K., and Ryan, M. E. 1992 Effect of the Adsorption of Polyvinyl Alcohol on the Rheology And Stability of Clay Suspensions. Journal of Rheology 36(2) 273-287

Chenevert, M. E. and Osisanya, S. O. 1992 Shale Swelling at Elevated Temperature and Pressure. ARMA-92-0869. Presented at the 33th U.S. Symposium on Rock Mechanics (USRMS), Santa Fe, California, 3-5 June

Chesser, B. G. 1987 Design Consideration for an Inhibitive, Stable Water-Based Mud System. SPE-14757-PA

Dairanieh, I. S. and Lahalih, S. M. 1988 Novel Polymeric Drilling Mud Viscosifiers. European Polymer Journal 24(9) 831-835

Darley, H. C. H. 1988 Composition and Properties of Drilling and Completion Fluids, 5th ed. Elsevier Inc.

Dye, W., d'Augereau, K., Hansen, N., Otto, M., Shoults, L., Leaper, R., Clapper, D.,and Xiang, T. 2006 New Water-Based Mud Balances High-Performance Drilling and Environmental Compliance. SPE-92367-PA. Presented at the 2005 SPE/IADC Drilling Conference, Amsterdam, Netherlands, 23-25 February

Ewy, R. T. and Morton, E. K. 2008 Wellbore Stability Performance of Water Base Mud Additives. SPE-116139-PA. Presented at the 2008 SPE Annual Technical Conference and Exhibition, Denver, Colorado, 21-24 September

Ewy, R. T. and Morton, E. K. 2009 Shale Swelling Tests Using Optimized Water Content and Compaction Load. SPE-121334-MS. Presented at the 2009 SPE Western Regional Meeting, San Jose, California, 24-26 March

Ewy, R. T. and Stankovich, R. J. 2010 Shale Swelling, Osmosis, and Acoustic Changes Measured Under Simulated Downhole Conditions. SPE-78160-PA. Presented at the 2002 SPE/ISRM Rock Mechanics Conference, Irving, Texas, 20-23 October

Heath, D. and Tadros TH. F. 1983 Influence of pH, Electrolyte, and Poly(Vinyl Alcohol) Addition on the Rheological Characteristics of Aqueous Dispersions of Sodium Montmorillonite. Journal of Colloid and Interface Science, 93(2) 307-319

Huadi, F., Aldea, C., Mackereth, B., and Mukhlis, T. 2010 Successful KCl-free, Highly Inhibitive and Cost-Effective Water-Based Application, Offshore Ease Kalimantan, Indonesia. SPE-132690-MS. Presented at the 2010 IADC/SPE Asia Pacific Drilling Technology Conference and Exhibition, Ho Chi Minh City, Vietnam, 1-3 November

Huffman, K. A., Saffer, D. M., and Dugan, B. 2016 In Situ Stress Magnitude and Rock Strength in the Nankai Accretionary Complex: A Novel Approach Using Paired Constraints from Downhole Data in Two Wells. Earth, Planet, and Space 68(123)

İşçi, S., Ünlü, C. H., Atici, O, and Güngör, N. 2006 Rheology and Structure of Aqueous Bentonite-Polyvinyl alcohol Dispersions. Bulletin of Materials Science 29(5) 449-456

Mehtar, M., Brangetto, M., Soliman, A. A., Mielke, S., Alfonzo, and N., Young, S. 2010 Effective Implementation of High Performance Water Based Fluid Provides Superior Shale Stability Offshore Abu Dhabi. SPE-138564-MS. Presented at the 2010 Abu Dhabi International Petroleum Exhibition & Conference, Abu Dhabi, UAE, 1-4 November

Mostafa, B. A. and Assaad, F. F. 2007 Rheological and Electrical Properties of Bentonite in Anionic Polystyrene Sulfonate and Nonionic Poly(vinyl alcohol). Journal of Applied Polymer Science 104 3886-3894

Netwas Group Oil Principal Additives of KCl polymer muds https://www.netwasgroup.us/fluids-2/principal-additives-of-kcl-polymer-muds.html

Patel, A., Stamatakis, E., Friedheim, and J., E., Davis, E. 2001 Highly Inhibitive Water-Based Fluid System Provides Superior Chemical Stabilization of Reactive Shale Formations. AADE 01-NC-HO-55. Presented at the AADE 2001 National Drilling Conference, "Drilling Technology- The Next 100 Years", Houston, Texas, 27-29 March

Patel, A., Young and S., Friedheim, J. 2007 Advances in Inhibitive Water-Based Drilling Fluids- Can They Replace Oil-Based Muds? SPE-106476-MS. Presented at the 2007 SPE International Symposium on Oilfield Chemistry, Houston, Texas, 28 February-2 March

Patel, D. A. 2009 Design and Development of Quaternary Amine Compounds: Shale Inhibition with Improved Environmental Profile. SPE-121737-MS. Presented at the 2009 SPE International Symposium on Oilfield Chemistry, The Woodlands, Texas, 20–22 April

Tare, U. A., Mody and F. K. 2002 Managing Borehole Stability Problems: On the Learning, Unlearning and Relearning Curve. AADE-02-DFWM-HO-31. Presented at the AADE 2002 Technology Conference "Drilling & Completion Fluids and Waste Management", Houston, Texas, 2-3 April

Young, S. and Ramses, G., 2006 Drilling Performance and Environmental Compliance-Resolution of Both with a Unique Water-Based Fluid. SPE/-103967-MS. Presented at the 2006 SPE/IADC Indian Drilling Technology Conference and Exhibition, Mumbai, India, 16-18 October

Zhong, H. Qiu, Z., Chen, G., Huang, W., Dong, B., Zhang, D., Fu, J., and Tong, S. 2015 Improving the Wellbore Stability While Drilling Long Open Hole Shale Intervals in Tahe Oil Field. SPE-176165-MS. Presented at the 2015 SPE/IATMI Asia Pacific Oil & Gas Conference and Exhibition, Nusa Dua, Bali, Indonesia, 20-22 October

Zhong, H., Qiu, Z., Huang, W., and Cao, J. 2011 Shale Inhibitive Properties of Polyether Diamine in Water-Based Drilling Fluid. Journal of Petroleum Science and Engineering 78 510-515

Zhong, H., Qiu, Z., Huang, W., H., Caojie, Huang, D., and Li, H. 2013 Successful Application of Unique Polyamine High Performance Water-Based Drilling Fluid in Bohai Bay Shale Formations. IPTC-16721-MS. Presented at the 2013 International Petroleum Technology Conference, Beijing, China, 26-28 March

Zhou, Z. H., Huang, R. Z., and Chen, Y. F. 1992 Constitutive Equations of Shale and Clay Swelling: Theoretical Model and Laboratory Test Under Confining Pressure. SPE-22382-MS. Presented at the 1992 SPE International Meeting on Petroleum Engineering, Beijing, China, 24-27 March

DETERMINATION OF YOUNG'S MODULUS

Results of the triaxial test for Nankai trough319-C0009A 9R-1-WR intact core sample is shown in Figure 73. An enlarged figure for the 1st loading was shown in Figure 74.
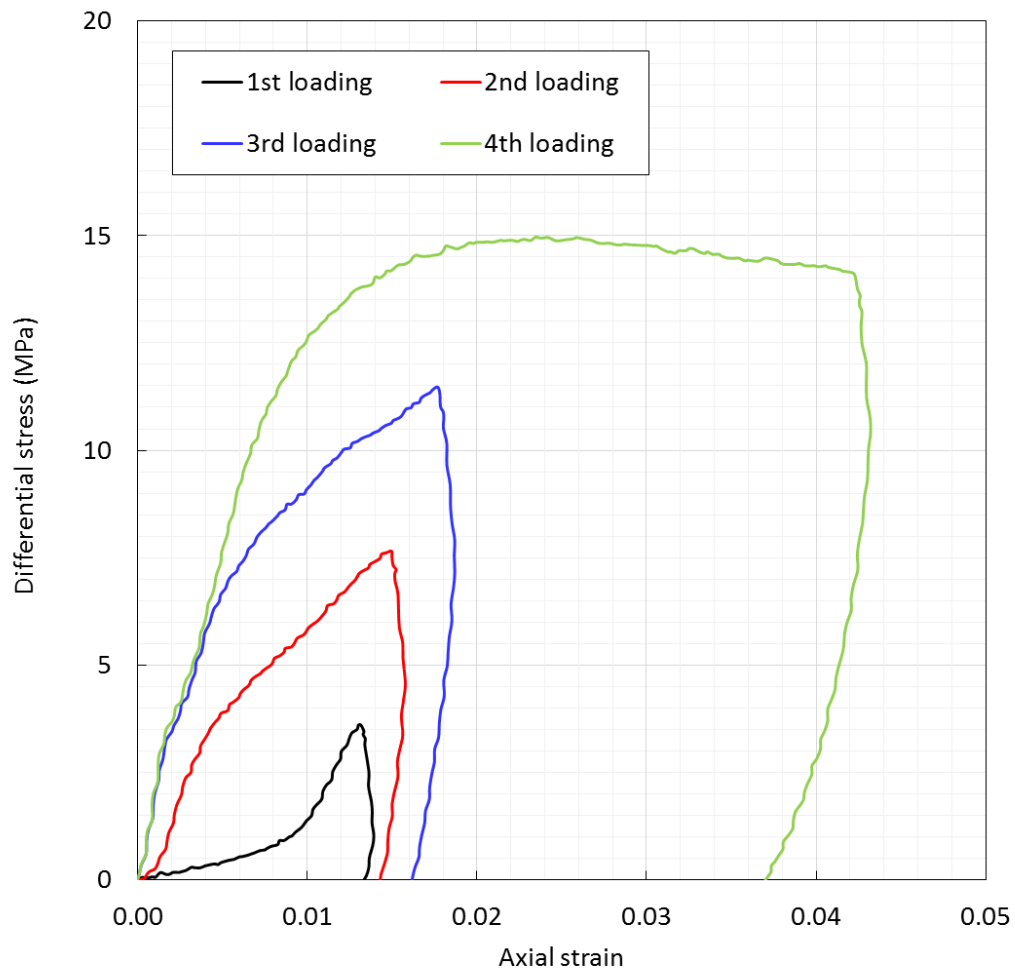

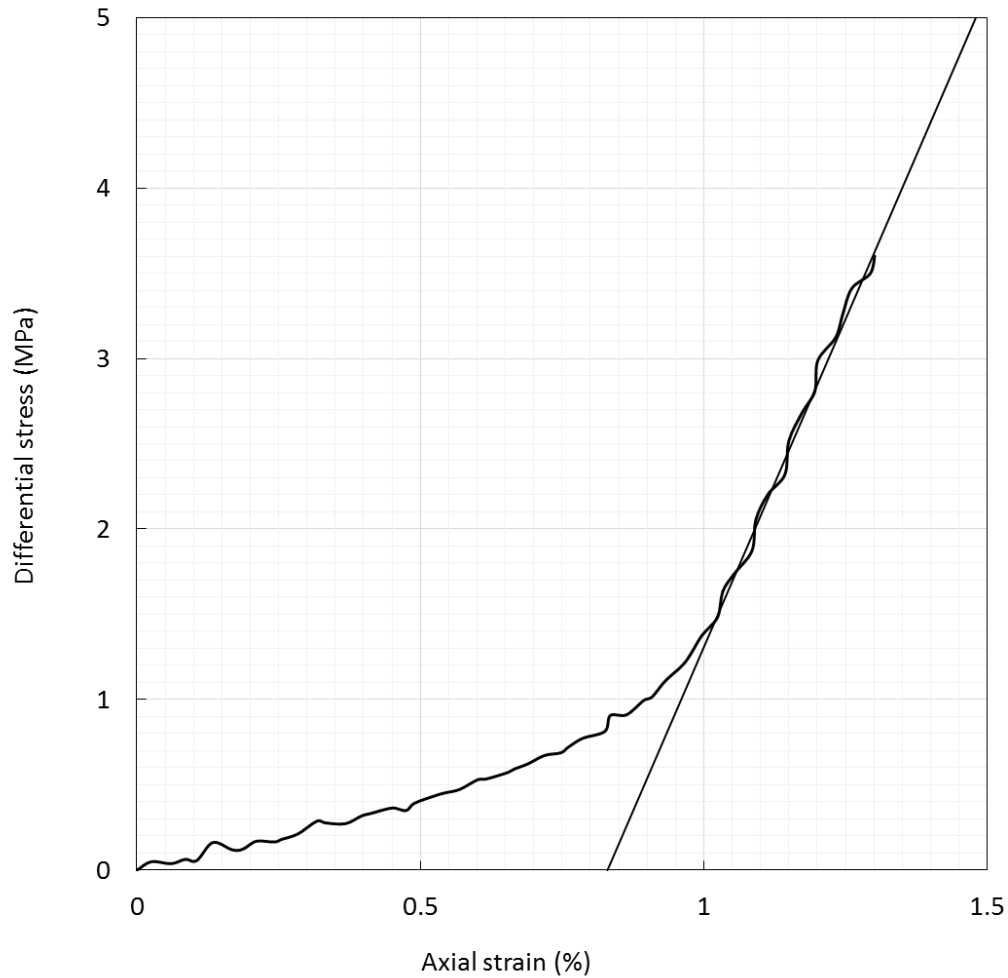**Figure 73 Stress strain curve for Nankai trough 319-C0009A 9R-1-WR intact core sample**

Figure 74 Enlarged figure for the 1st loading. Straight line is the tangent to the linear portion of the stress strain curve

As shown in Figure 74, we drew a tangent to the linear portion of the stress strain curve for the 1st loading. From the slope of the tangent, the Young's modulus was determined to be 769 MPa (1.1×10^5 psi).

DERIVATION OF NEAR WELLBORE STRESSES

Integration in Eq. (2) and (3) can be calculated as follows.

For $r_w \leq r < r_S$,

$$\int_{r_w}^{r} r \left\{ \alpha \Delta p + \frac{E}{1-2\nu} (\eta \Delta T + \Delta S) \right\} dr$$

$$= \alpha \Delta p_w \int_{r_w}^{r} r \left\{ 1 - \frac{\ln(r/r_w)}{\ln(r_p/r_w)} \right\} dr + \frac{E\eta \Delta T_w}{1-2\nu} \int_{r_w}^{r} r \left\{ 1 - \frac{\ln(r/r_w)}{\ln(r_T/r_w)} \right\} dr$$

$$+ \frac{E \Delta S_w}{1-2\nu} \int_{r_w}^{r} r \left\{ 1 - \frac{\ln(r/r_w)}{\ln(r_S/r_w)} \right\} dr$$

$$= \alpha \Delta p_w \int_{r_w}^{r} \left\{ r - \frac{r \ln r}{\ln(r_p/r_w)} - \frac{\ln r_w}{\ln(r_p/r_w)} r \right\} dr$$

$$+ \frac{E\eta \Delta T_w}{1-2\nu} \int_{r_w}^{r} \left\{ r - \frac{r \ln r}{\ln(r_T/r_w)} - \frac{\ln r_w}{\ln(r_T/r_w)} r \right\} dr$$

$$+ \frac{E \Delta S_w}{1-2\nu} \int_{r_w}^{r} \left\{ r - \frac{r \ln r}{\ln(r_S/r_w)} - \frac{\ln r_w}{\ln(r_S/r_w)} r \right\} dr$$

$$= \alpha \Delta p_w \left[\frac{1}{2} r^2 - \frac{1}{\ln(r_p/r_w)} \left\{ \frac{1}{2} r^2 \ln r - \frac{1}{4} r^2 \right\} - \frac{\ln r_w}{\ln(r_p/r_w)} \frac{1}{2} r^2 \right]_{r_w}^{r}$$

$$+ \frac{E\eta \Delta T_w}{1-2\nu} \left[\frac{1}{2} r^2 - \frac{1}{\ln(r_T/r_w)} \left\{ \frac{1}{2} r^2 \ln r - \frac{1}{4} r^2 \right\} - \frac{\ln r_w}{\ln(r_T/r_w)} \frac{1}{2} r^2 \right]_{r_w}^{r}$$

$$+ \frac{E \Delta S_w}{1-2\nu} \left[\frac{1}{2} r^2 - \frac{1}{\ln(r_S/r_w)} \left\{ \frac{1}{2} r^2 \ln r - \frac{1}{4} r^2 \right\} - \frac{\ln r_w}{\ln(r_S/r_w)} \frac{1}{2} r^2 \right]_{r_w}^{r}$$

$$= \alpha \Delta p_w \left[\frac{1}{2} r^2 - \frac{1}{\ln(r_p/r_w)} \left(\frac{1}{2} r^2 \ln \frac{r}{r_w} - \frac{1}{4} r^2 \right) \right]_{r_w}^{r}$$

$$+ \frac{E \eta \Delta T_w}{1 - 2\nu} \left[\frac{1}{2} r^2 - \frac{1}{\ln(r_T/r_w)} \left(\frac{1}{2} r^2 \ln \frac{r}{r_w} - \frac{1}{4} r^2 \right) \right]_{r_w}^{r}$$

$$+ \frac{E \Delta S_w}{1 - 2\nu} \left[\frac{1}{2} r^2 - \frac{1}{\ln(r_S/r_w)} \left(\frac{1}{2} r^2 \ln \frac{r}{r_w} - \frac{1}{4} r^2 \right) \right]_{r_w}^{r}$$

$$= \alpha \Delta p_w \left[\frac{1}{2} (r^2 - r_w^2) - \frac{1}{\ln(r_p/r_w)} \left\{ \frac{1}{2} r^2 \ln \frac{r}{r_w} - \frac{1}{4} (r^2 - r_w^2) \right\} \right]$$

$$+ \frac{E \eta \Delta T_w}{1 - 2\nu} \left[\frac{1}{2} (r^2 - r_w^2) - \frac{1}{\ln(r_T/r_w)} \left\{ \frac{1}{2} r^2 \ln \frac{r}{r_w} - \frac{1}{4} (r^2 - r_w^2) \right\} \right]$$

$$+ \frac{E \Delta S_w}{1 - 2\nu} \left[\frac{1}{2} (r^2 - r_w^2) - \frac{1}{\ln(r_S/r_w)} \left\{ \frac{1}{2} r^2 \ln \frac{r}{r_w} - \frac{1}{4} (r^2 - r_w^2) \right\} \right]$$

For $r_S \leq r$,

$$\int_{r_w}^{r} r \left\{ \alpha \Delta p + \frac{E}{1 - 2\nu} (\eta \Delta T + \Delta S) \right\} dr$$

$$= \alpha \Delta p_w \left[\frac{1}{2} (r_p^2 - r_w^2) - \frac{1}{\ln(r_p/r_w)} \left\{ \frac{1}{2} r_p^2 \ln \frac{r_p}{r_w} - \frac{1}{4} (r_p^2 - r_w^2) \right\} \right]$$

$$+ \frac{E \eta \Delta T_w}{1 - 2\nu} \left[\frac{1}{2} (r_T^2 - r_w^2) - \frac{1}{\ln(r_T/r_w)} \left\{ \frac{1}{2} r_T^2 \ln \frac{r_T}{r_w} - \frac{1}{4} (r_T^2 - r_w^2) \right\} \right]$$

$$+ \frac{E \Delta S_w}{1 - 2\nu} \left[\frac{1}{2} (r_S^2 - r_w^2) - \frac{1}{\ln(r_S/r_w)} \left\{ \frac{1}{2} r_S^2 \ln \frac{r_S}{r_w} - \frac{1}{4} (r_S^2 - r_w^2) \right\} \right]$$